

**Computational and Experimental Investigation of Ras
Homodimer Formation, Ras-effector Interactions and Ras
Shuttling**

by

Serena Muratciođlu

A Dissertation Submitted to the
Graduate School of Sciences and Engineering
in Partial Fulfillment of the Requirements for
the Degree of
Doctor of Philosophy
in
Chemical and Biological Engineering



January 31, 2018

**Computational and Experimental Investigation of Ras Homodimer
Formation, Ras-effector Interactions and Ras Shuttling**

Koç University

Graduate School of Sciences and Engineering

This is to certify that I have examined this copy of a doctoral dissertation by

Serena Muratcioğlu

and have found that it is complete and satisfactory in all respects,
and that any and all revisions required by the final
examining committee have been made.

Committee Members:

Prof. Özlem Keskin (Advisor)

Prof. Attila Gürsoy (Co-Advisor)

Prof. İ. Halil Kavaklı

Assoc. Prof. Elif Özkırımlı Ölmez

Assoc. Prof. Gizem Dinler Doğanay

Assist. Prof. Cem Albayrak

Date _____



Dedelerime

ABSTRACT

Ras proteins recruit and activate effectors that transmit receptor-initiated signals. Activation of Ras elicits a wide variety of cellular responses depending on the specific effector that becomes activated. However, Ras signaling cascades are still not entirely understood. How the effectors are regulated, and how the cell decides among them under different environments and in distinct cancers is still not elucidated completely. Ras is believed to function as a monomer. Monomeric Ras can bind Raf, a Ras effector; however, activation of Raf requires its dimerization. Since Raf alone does not form a stable dimer, dimeric Ras was thought to promote dimerization and activation of Raf. But, how Ras dimerizes and this dimerization relates to activation of effectors is still unclear. The aim of this dissertation is to elucidate the structural basis of Ras dimerization and investigate the effect of dimerization on effector binding and activation. To this end, experimental and computational approaches were combined. Computationally, I predicted two major dimer interfaces by employing PRISM (PRotein Interactions by Structural Matching). The first, highly populated β -sheet dimer interface is mapped to Switch I and effector binding regions. The second helical interface may promote Raf's activation. To validate the predictions, some of the residues at the dimer interfaces were mutated to investigate the effect of these mutations on Ras-Ras interaction and signaling. Here, K101D/R102E and R41E/K42D double mutations on the helical and beta interfaces, respectively, decreased Ras concentration, thus affected MAPK signaling. R41E/K42D double mutation had an additional effect on MAPK signaling, most probably through the interfering with Ras-Raf interaction. To signal, Ras isoforms must be enriched at the plasma membrane (PM). It was suggested that phosphodiesterase- δ (PDE δ) can bind and shuttle some farnesylated Ras isoforms to the PM. To study Ras/PDE δ interactions, I performed MD simulations. Earlier data suggested that PDE δ extracts K-Ras4B and N-Ras from the PM; but surprisingly not K-Ras4A. The simulations suggest that PDE δ can bind to farnesylated K-Ras4A and N-Ras like K-Ras4B – albeit not as strongly. This weaker binding, coupled with stronger anchoring of

K-Ras4A in the membrane, can explain the observation of why PDE δ is unable to effectively extract K-Ras4A.



ÖZETÇE

Ras proteinleri, hücreye gelen sinyalin iletiminde rol oynayan efektör proteinlerini aktive eder. Rasın aktivasyonu, aktive olan efektör proteinine bağlı olarak, farklı hücresel cevaplar oluşturur. Ras sinyal yollarının işleyişi henüz tam olarak bilinmemektedir. Cevaplanması gereken en önemli sorular arasında efektörlerin nasıl kontrol edildiği, ve hücrenin farklı koşullarda ve belirgin kanser tiplerinde bu efektörlerden hangisinin aktive edileceğine nasıl karar verdiği yer almaktadır. Ras'ın monomer olarak fonksiyonel olduğuna inanılmaktadır. Ras, efektörlerinden biri olan Raf'a monomer olarak bağlanabilir. Ancak Raf'ın aktif hale gelebilmesi için dimer oluşturması gerekmektedir. Bu nedenle, Ras dimerinin Raf dimerizasyonunu ve aktivasyonunu teşvik ettiği düşünülmektedir. Ancak, dimerizasyon ile efektör aktivasyonu arasındaki ilişki henüz açık değildir. Bu tezde, Ras dimerizasyonunun yapısal temeli hakkında var olan bilgiyi genişletmek ve dimerizasyonun efektör etkileşimi ve aktivasyonu üzerindeki etkisini incelemek amacıyla hesaplamalı ve deneysel yaklaşımları birleştirdim. Güçlü bir tahmin algoritması olan PRISM'i kullanarak iki dimer arayüzeyi tahmin edildi. β -sheet olarak adlandırdığımız ilk arayüzey Switch I ve efektör bağlanma bölgesinde bulunmaktadır. Helikal arayüzey olarak adlandırdığımız ikinci arayüzey Raf'ın dimerizasyonunu teşvik edebilir. Tahmin edilen arayüzeyleri doğrulamak amacıyla bu arayüzeylerdeki bazı amino asitler mutasyona uğratıldı ve bu mutasyonların Ras-Ras etkileşimi ve sinyal iletimi üzerindeki etkilerini incelendi. Sonuçlar K101D/R102E ve R41E/K42D mutasyonlarının hücredeki Ras konsantrasyonunu düşürdüğünü, dolayısıyla MAPK sinyal iletimini etkilediğini göstermektedir. Ayrıca, sonuçlar R41E/K42D mutasyonunun Ras-Raf etkileşimi üzerinde de bir etkisi olabileceğine işaret etmektedir. Sinyalin iletilmesi için Ras proteinlerinin plazma membranında lokalize olmaları gerekir. Phosphodiesterase- δ (PDE δ) proteininin bazı farnezenmiş Ras izoformlarına bağlandığı ve onları membrane taşıdığı bilinmektedir. Ras/PDE δ etkileşimini MD simülasyonları ile incelendi. Önceki çalışmalar, PDE δ 'nın K-Ras4B ve N-Ras izoformlarını membrandan ekstrakte ettiğini ancak K-Ras4A'yi edemediğini göstermektedir. Simülasyonlar, PDE δ 'nın her üç izoforma da farklı afinitelerle bağlanabildiğini göstermektedir. PDE δ 'nın K-Ras4A izoformuna daha zayıf bir şekilde

bağlandıđı ve bu izoformun membran ile daha kuvvetli etkileştiđi göz önüne alındığında, PDEδ'nın K-Ras4A izoformunu membrandan neden ekstrakte edemediđi açıklanabilir.



ACKNOWLEDGEMENT

I would like to thank all the people who contributed in some way to the work described in this thesis. First and foremost, I would like to express my sincere gratitude to my advisors Prof. Özlem Keskin and Prof. Attila Gürsoy for their continuous support, patience, and motivation. Their guidance helped me in all the time of research and writing of this thesis. One simply could not wish for friendlier supervisors.

Besides my advisors, I would like to offer my special thanks to our dear collaborators Prof. Ruth Nussinov and Dr. Hyunbum Jang for their invaluable encouragement, advices, and contributions to my research. I am also deeply grateful to Prof. Halil Kavaklı, Assist. Prof. Cihan Aydın, and Assoc. Prof. İbrahim Barış for their support and guidance in the experimental part of the study. Without their insights and help, I would not be able to conduct the experiments. I appreciate the feedback offered by my thesis committee members, Prof. Halil Kavaklı and Assoc. Prof. Elif Özkırmınlı Ölmez. Advice and comments given by them have been a great help in the progress of my studies. I would also like to thank my other thesis jury members Assoc. Prof. Gizem Dinler Doğanay, and Assist. Prof. Cem Albayrak for their valuable time.

I would also like to express my gratitude to the Scientific and Technological Research Council of Turkey (TUBITAK) (Project No: 114M196) for their financial support.

Every result described in this thesis was accomplished with the help and support of fellow officemates and labmates. Thus, I would like to thank to former and current COSBI lab members: Emine Güven-Maiorov, Emel Şen Kılıç, Doğu Doğru, Engin Çukuroğlu, Deniz Demircioğlu, Alper Başpınar, who have been great friends to me, Ece Acuner-Özbabacan, H. Billur Engin, Güray Kuzu, Nilay Karahan, Cemal Yamak, A. Derya Cavga, Farideh Halakou, E. Sıla Özdemir, Efe Elbeyli, Bilgesu Erdoğan, Mahan Rajaei Golsefidı, A. Tuğrul Balcı, and Ayşe S. Yazgılı. I also thank my labmates in Kavaklı lab: Selma Bulut, Sibel Çal Kayıtmazbatır, Darya Yarperver, Şeref Gül, Haşımcan Öner, and Ehsan Sarayloo for their help and all the fun we have had in the last three years.

I am deeply grateful to my housemates, Güneş Raif, Aysu Altun, Işıl Koyuncu, Bilgesu Erdoğan, and Yasemin Vardar for their endless support and all the amazing time we shared.

I would particularly like to thank my dear friends Mari Luiz Saatçıyan, Emine Güven-Maiorov, Emel Şen Kılıç, Bilgesu Erdoğan, Bakış Doğru, Doğuş Doğru, Efe Elbeyli, Houman Bahmani Jalali, and Nazlı Ataç for being there whenever I need. These people made this long, hard PhD road more bearable, easier and funnier.

Last but not least, I owe my deepest gratitude to my family, especially my parents and brother. Without their love, emotional support, understanding and endless encouragement I would not be able to pursue this research work. Thank you for always being there and for making this pursuit worthwhile. This thesis is dedicated to my grandfathers. I have always felt so lucky and proud that I had such wonderful and loving grandfathers. They always made me feel competent and confident, so thank you for making me who I am today.

TABLE OF CONTENTS

LIST OF FIGURES	XIII
LIST OF TABLES	XV
NOMENCLATURE	XVI
CHAPTER 1	1
INTRODUCTION	1
CHAPTER 2	4
LITERATURE REVIEW	4
2.1. Ras History.....	4
2.2. Ras Family	4
2.3. Ras Structure and Post-translational Modifications (PTMs)	6
2.4. Plasma Membrane and Ras Signaling.....	10
2.5. Shuttling of Ras Proteins	11
2.6. Ras-effector Interactions	13
2.7. Ras Signaling Pathways	17
2.8. Ras Dimerization, Oligomerization and Clustering.....	19
2.9. Main contributions	23
CHAPTER 3	25
MATERIALS AND METHODS	25
3.1. Computational Prediction of the Structures of H-Ras and K-Ras4B Dimers	25
3.1.1. Determination of the residues to be mutated	26
3.2. Confirmation of the Predicted Interface Residues Involved In Dimerization by Bimolecular Fluorescence Complementation (BiFC).....	26
3.2.1. Cloning strategy for BIFC system	26
3.2.1.1. Cloning of interface mutants.....	32
3.2.2. Transfection of wildtype and oncogenic pTTB-HRAS and pTTB-KRAS.....	34
3.2.3. Visualizing the cells by fluorescence microscopy	35
3.2.4. Immunofluorescence, Microscopy and Quantification.....	35

3.2.5. Determination of the Ras expression and pERK, pAKT levels by western blotting	36
3.2.6. Real-time PCR	37
3.2.7. Statistical analysis	37
3.3. Computational Prediction of Ras-Effector Interactions	38
3.4. Computational prediction of the structure of K-Ras4B with CaM and PI3K	38
3.5. MD Simulations of the K-Ras4B/PDE δ and HVR/PDE δ Complexes	39
3.5.1. Generating initial configurations	39
3.5.2. Atomistic MD simulations	40
3.5.3. MM/GBSA calculations	41
CHAPTER 4	43
H-RAS AND K-RAS4B HOMODIMERS	43
4.1. Computational Prediction of the Structures of H-Ras and K-Ras4B Dimers	43
4.2. Determination of the Residues to Be Mutated	49
4.2. Experimental Investigation of H-Ras and K-Ras4B Dimers	53
4.2.1. Investigation of the interaction by bimolecular fluorescence complementation	53
4.2.2. Determination of the Ras expression and pERK, pAKT levels upon mutation	59
CHAPTER 5	71
RAS-EFFECTOR INTERACTIONS	71
5.1. Case Study (Ras/RASSF and Ras/Raf Interactions)	79
5.2. K-Ras4B/CaM/P3K interaction	79
CHAPTER 6	83
PDEA BINDING TO RAS ISOFORMS	83
6.1. The Interaction of the Catalytic Domain of K-Ras4B-GTP with PDE δ	83
6.2. The Interaction of the Prenylated K-Ras4B-GTP with PDE δ	83
6.3. Binding Energy in Dimer Formation	88
6.4. The Interactions of Farnesylated HVRs of K-Ras4A, K-Ras4B, and N-Ras with PDE δ	89
6.5. Discussion	93
CHAPTER 7	97
CONCLUSION	97
APPENDIX A	99
APPENDIX B	108

APPENDIX C	116
APPENDIX D.....	121
BIBLIOGRAPHY	123
VITA.....	135



LIST OF FIGURES

Figure 2.1. The Ras GD/GTP cycle.....	5
Figure 2.2. Multiple sequence alignment of the amino acids in the H-Ras, N-Ras, K-Ras 4A, and K-Ras4B.....	6
Figure 2.3. Cartoon representation of H-Ras crystal structures.....	8
Figure 2.4. Cartoon representation of K-Ras4B crystal structures.....	9
Figure 2.5. Differential effects of calmodulin on two key K-Ras4B effector pathways.....	17
Figure 2.6. Ras signaling.....	19
Figure 3.1. Diagnostic digest for VN173 and VC155 cloned into pJET2.1.....	27
Figure 3.2. Diagnostic digest for wild type and constitutively active mutants.....	28
Figure 3.3. Diagnostic digest results for the wild type and mutant Venus-Ras plasmids.....	29
Figure 3.4. Diagnostic digest results for pTTB-VN173-Ras plasmids.....	30
Figure 3.5. Diagnostic cut results.....	31
Figure 3.6. Diagnostic digest results of pJET2.1-Venus-RAS and pJET2.1-Venus-HRAS_G12V and pJET2.1-Venus-KRAS4B_G12D interface mutants.....	33
Figure 3.7. Diagnostic digest results of pJET2.1-Venus-HRAS and pJET2.1-Venus-HRAS_G12V interface mutants.....	34
Figure 4.1. Predicted homodimer structure of active Ras isomer.....	44
Figure 4.2. Predicted homodimer structure of inactive Ras isomers.....	45
Figure 4.3. Crystal and predicted structures of Ras dimers.....	46
Figure 4.4. Predicted structures of Ras heterodimers.....	47
Figure 4.5. Predicted tetramer structure of active K-Ras4B.....	48
Figure 4.6. Ras-effector binding and tetramerization.....	49
Figure 4.7. Relaxed K-Ras4B dimers at the membrane.....	50
Figure 4.8. Relaxed H-Ras dimers at the membrane.....	51
Figure 4.9. Predicted homodimer structures of active H- and K-Ras4B.....	53
Figure 4.10. K-Ras4B dimerization was confirmed with BIFC system in HEK 293T cells.....	55

Figure 4.11. H-Ras dimerization was confirmed with BIFC system in HEK 293T cells.....	56
Figure 4.12. Charge reversal mutations decrease Ras dimerization and interfere with Ras membrane localization.....	58
Figure 4.13. Western blot analysis for expression of K-Ras4B ^{G12D} , H-Ras ^{G12V} and their interface mutants.....	60
Figure 4.14. Comparison of the protein levels.....	60
Figure 4.15. Effect of interface mutations on ERK phosphorylation in HEK293T cells.....	62
Figure 4.16. Effect of interface mutations on ERK phosphorylation in HEK293T cells.....	63
Figure 4.17. K101D/R102E and R41E/K42D reduce ERK phosphorylation, but increase Akt phosphorylation.....	65
Figure 4.18. Predicted Ras complex structures.....	67
Figure 4.19. Ras mutations cause downregulation of <i>FOS</i> and <i>EGR1</i> in HEK293T cells.....	69
Figure 5.1. Predicted H-Ras complex structures.....	72
Figure 5.2. Predicted K-Ras4B complex structures.....	74
Figure 5.3. Predicted complex structure of H-Ras and cell division control protein 42 homolog (Cdc42).....	78
Figure 5.4. Multiple sequence alignment of Ras isoforms.....	79
Figure 5.5. A K-Ras4B-GTP/calmodulin/PI3Ka ternary complex model based on the prediction.....	81
Figure 6.1. The superimposed snapshots of the final conformation and the starting point of six K-Ras4B-GTP/PDE δ systems.....	85
Figure 6.2. The key residues involved in K-Ras4B-GTP/PDE δ complex formation... ..	86
Figure 6.3. Hydrophobic interactions involved in K-Ras4B-GTP/PDE δ complex formation.....	88
Figure 6.4. The snapshots of farnesylated HVR/PDE δ complexes.....	90
Figure 6.5. The key residues involved in HVR/PDE δ complex formation.....	91
Figure 6.6. Hydrophobic interactions involved in HVR/PDE δ complex formation.....	92

LIST OF TABLES

Table 4.1. Residues selected for site-directed mutagenesis.....	52
Table 6.1. Binding energy in dimer formation using MM/GBSA method for the prenylated K-Ras4B-GTP/PDE δ systems.....	89



NOMENCLATURE

AFAD	Adherens Junction Formation Factor
BiFC	Bi-molecular fluorescence complementation
Bry	Brachyury
cDNA	complementary DNA
Cdc42	cell division control 42
GAP	GTPase activating protein
GDP	Guanine dinucleotide
GEF	Guanine-nucleotide exchange factor
GTP	Guanine trinucleotide
h	hour
MAPK	Mitogen-activated protein kinases
mRNA	messenger RNA
PCR	Polymerase chain reaction
PDB	Protein Data Bank
PDE δ	Phosphodiesterase- δ
PI3K	Phosphoinositide 3-kinase
PLC ϵ	Phospholipase C ϵ
PM	Plasma Membrane
PPI	Protein-Protein Interaction
PRISM	PRotein Interactions by Structural Matching
RAIN	Ras interactinhg protein
RALGDS	Ral guanine nucleotide dissociation
RASSF	Ras association domain containing protein
RGS	Regulator of G protein signaling
RhoGDI	Rho GDP dissociation inhibitor
Sos	Son of sevenless

Chapter 1

INTRODUCTION

Ras-family proteins are small membrane-associated GTPases. Acting as molecular switches in response to receptor-mediated extracellular signals, they regulate an astonishing diversity of cellular functions such as proliferation, differentiation, cell morphology, motility, intracellular trafficking and gene expression. Oncogenic Ras mutations are among the most common events in human cancer. Despite tremendous effort, these proteins are still “undruggable”. Thus, researchers seek different strategies to target oncogenic Ras. Interfering with its PM localization, and targeting effector pathways downstream of Ras, are two major approaches that hold promise for blocking oncogenic Ras signaling.

Ras is believed to function as a monomer. Monomeric Ras can bind Raf; however, Raf needs to dimerize for activation. An earlier observation that C-Raf forms dimers, trimers, and tetramers in the presence of active Ras suggests that Ras plays a significant role in Raf dimerization [1]. Studies indicating that N-Ras-GDP can form dimers in a model membrane [2] and native H-Ras can dimerize on membrane surfaces [3] raise the question whether dimeric Ras can promote Raf dimerization and activation. Structure of Ras dimers, and how dimerization relates to activation of effectors, however, are still unknown. In this thesis, I showed that active H-Ras and K-Ras4B can form stable homodimers through two major dimer interfaces, β -sheet and helical. The β -sheet dimer interface overlaps with effectors' (including Raf and PI3K) binding regions. The second helical interface can promote Raf dimerization. Experiments to validate predicted structures *in vitro* revealed that K101D/R102E double mutation on the helical interface affects Ras dimerization, but does not block MAPK signaling. On the other hand, R41E/K42D double mutation on the beta interface downregulated MAPK signaling.

Active Ras proteins transmit the information through a physical interaction with its downstream effector proteins. Ras GTPases activate more than 20 signaling pathways, regulating essential cellular functions such as proliferation, survival, and migration. However, how Ras proteins control their signaling diversity is still a mystery. Predicting structures of Ras with its effector proteins can help solve this mystery and understand the pathways at the structural level. To this end, Ras-effector structures were calculated and it is shown that most of these binding partners interact with Ras through the effector binding region, thus compete for binding. Some of the partners, on the other hand, bind to C-terminal allosteric lobe on Ras, thus compete with Ras dimerization through the helical interface.

Ras proteins must be attached to the plasma membrane (PM) to relay the signal. Thus, interfering with Ras localization is one of the approaches to target oncogenic Ras [4, 5]. However, the transport of Ras proteins to the PM is not fully understood. Studies indicate that phosphodiesterase- δ (PDE δ) can bind and shuttle some farnesylated Ras isoforms to the PM – but not all. To gain structural and conformational dynamics insight into the Ras/PDE δ interaction, K-Ras4B/PDE δ and HVR/PDE δ complexes were simulated. The results indicate that PDE δ can bind to farnesylated K-Ras4A and N-Ras like K-Ras4B, but with different affinities.

Chapter 2 gives a comprehensive review on Ras proteins and signaling, Ras dimerization and its significance, and membrane shuttling of Ras.

Chapter 3 provides a detailed explanation about the materials and methods used in this study.

Chapter 4 presents computational and experimental results for Ras dimerization, and its effect on MAPK pathway, and provides a detailed discussion of the results including the functional outcome of Ras dimerization.

Chapter 5 focuses on Ras-effector interactions and includes the complex structures of these partners. It also refers to isoform-specific interactions and discusses the competitive pathways.

Chapter 6 addresses detailed explanation of the results for K-Ras4B/PDE δ interaction and discusses the implications of this interaction for other Ras isoforms.

Chapter 7 presents the conclusion and future perspectives



Chapter 2

LITERATURE REVIEW

2.1. Ras History

Ras genes were first identified and characterized as transduced oncogenes in the Harvey [6] and Kirsten [7] strains of acutely transforming retroviruses. In the late 1970s, Scolnick and colleagues identified the cellular origin of the viral *H-ras* and *K-ras* genes [8] and showed that these human Ras genes encode 21 kDa proteins [9, 10] that can bind GDP/GTP [11]. In addition, using electron microscopic immunocytochemistry they showed that majority of these proteins are localized to the cytoplasmic surface of the plasma membrane (PM) and that PM is their major action site [12]. In 1982, three groups discovered that these Ras genes are indeed the same genes that were identified as transforming genes in the NIH/3T3 DNA transfection assays [13-15]. By the end of the year, they found that a single missense mutation in codon 12 causes *HRAS* and *KRAS* gene activation in the EJ/T24 bladder carcinoma cell line, [16], and lung and colon tumor cells [17], respectively. Additionally, in neuroblastoma-derived DNA, a third transforming human *RAS* gene, *NRAS*, was discovered [18, 19]. These pioneering studies prompted further analyses of Ras genes and their products. Active *RAS* genes were detected in majority of the human tumor cell lines [20]. The screening of the tumor cell lines revealed that in addition to mutations at codon 12, transforming *RAS* genes carried mutations at codons 13 and 61.

2.2. Ras Family

Ras-family proteins are small membrane-associated GTPases that are activated in response to various extracellular stimuli, such as growth factors, receptors, and hormones. Ras proteins can activate multiple signaling pathways that regulate cell proliferation, migration, survival and differentiation [21, 22].

Ras proteins are quintessential members of small GTPases that function as molecular switches by alternating between inactive GDP-bound and active GTP-bound states [23-29]. Activation is tightly regulated by Guanine nucleotide exchange factors (GEFs), which catalyze the exchange of GDP to GTP. Active Ras-GTP can bind and activate downstream effectors, including Raf kinase, phospho-inositol 3 kinase (PI3K), and Ral guanine nucleotide dissociation stimulator (RalGDS) [30-32]. Ras inactivation is mediated by GTPase-activating proteins (GAPs) which accelerate the intrinsic GTP hydrolysis rate of Ras by several orders of magnitude [33] (Figure 2.1). Ras mutations that impair GTPase activity are insensitive to GAPs, rendering mutant Ras proteins persistent in their active GTP-bound state, thereby prolonging downstream signaling associated with oncogenic cell growth [34-37].

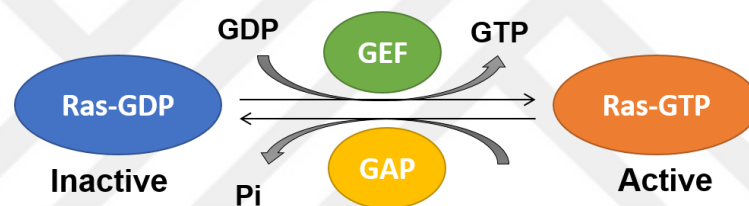


Figure 2.1. The Ras GD/GTP cycle. The cycling between the active and inactive state is controlled with GEF and GAP proteins.

The three human *RAS* genes encode four highly similar proteins: H-Ras, N-Ras, and K-Ras4A and K-Ras4B. The two K-Ras proteins arise from alternative splicing at the C terminus [38, 39]. H-Ras, K-Ras4A and N-Ras have 189 amino acids, while K-Ras4B has 188 amino acids. Multiple sequence alignment (Figure 2.2) reveals that the total sequence identity between the four isoforms is approximately 79% [40]. Remarkably, the catalytic domain (residues 1-166) of the four isoforms shares highly conserved sequence identity (~ 89%), while extremely low sequence identity (~ 8%) is observed in the hypervariable region (HVR) of the four isoforms (residues 167-189 for H-Ras, K-Ras4A, and N-Ras; 167-188 for K-Ras4B). Despite a high degree of sequence identity across Ras isoforms, the frequency and distribution of Ras mutations are not equivalent. The Catalog of Somatic Mutations in Cancer (COSMIC) [41] confirms that K-Ras is the most frequently mutated isoform in Ras-driven cancers (86%), followed by N-Ras

(11%) and H-Ras (3%) [42]. Mutated isoforms tend to associate with particular tumor types [32, 43-47]: K-Ras mutations occur at very high frequency in pancreatic ductal adenocarcinoma, lung and colon tumors; N-Ras mutations are commonly detected in hematopoietic tumors and in malignant melanomas; H-Ras mutations are the most frequent in bladder tumors and head and neck squamous cell carcinoma. Significantly, 98% of the oncogenic Ras mutations are found at amino acid residues G12, G13 and Q61, whose mutations impair intrinsic and GAP-mediated GTP hydrolysis, locking mutant Ras in the active Ras-GTP state.

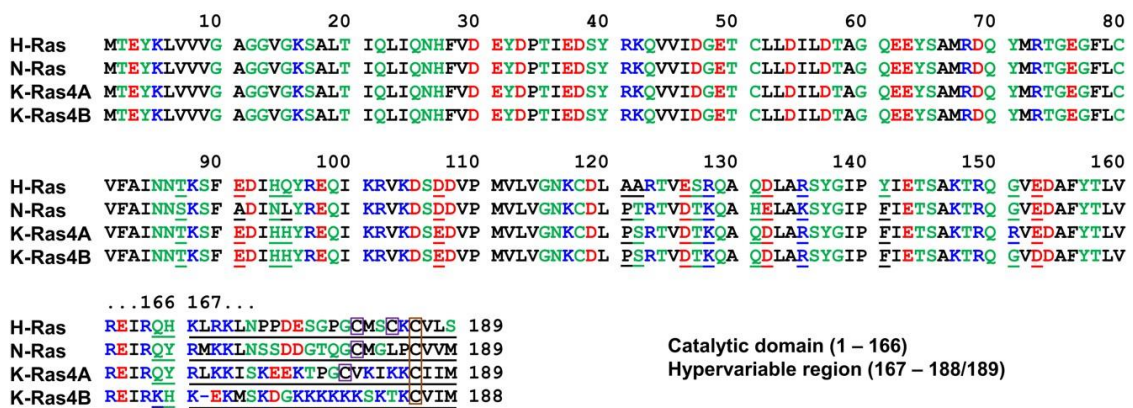


Figure 2.2. Multiple sequence alignment of the amino acids in the H-Ras, N-Ras, K-Ras4A, and K-Ras4B. In the sequence, hydrophobic, polar/glycine, positively charged, and negatively charged residues are colored black, green, blue, and red, respectively. The non-identity of residues in the alignment is indicated by under-lined texts. In the hypervariable region (HVR) sequences, the purple boxes denote the palmitoylated cysteines and orange-boxes indicate the farnesylated cysteines. A distinguishing feature of the HVR of K-Ras4B is bearing a polybasic stretch [48].

2.3. Ras Structure and Post-translational Modifications (PTMs)

H-Ras was the first Ras structure determined in 1988 [49]. X-ray crystal structures of H-Ras catalytic domain complexed with GppNHp, a GTP analogue, (PDB ID 5P21) [50] and GDP (PDB ID 4Q21) [51] revealed that the catalytic domain of Ras is composed of the quintessential G-domain structure containing the catalytic machinery with six β -strands (β 1- β 6) flanked by five α -helices (α 1- α 5) and ten connecting loops (Figure 2.3

A and 2.3 B). The functional P-loop (residues 10-17), switch I (residues 30-38), and switch II (residues 59-76) regions constitute the active site for GTP/GDP binding and interaction sites for effector proteins, including Raf, PI3K, RalGDS and GAP [52]. These structural elements are within the first ‘effector lobe’ (residues 1-86) half of the catalytic domain, which has 100% sequence identity across Ras isoforms [53, 54]. The remainder of the molecule, containing a more variable sequence among Ras isoforms, serves as the second ‘allosteric lobe’ (residues 87-166) half of the catalytic domain, which has an allosteric site [55]. Arguably the most remarkable differences in the GppNHp- (a GTP analogue) and GDP-bound H-Ras are in the switch I and switch II regions (Figure 2.3 D), revealing a crucial role of the nucleotide-mediated cooperativity between the two switch regions in the conformational transition [56]. The root-mean-square deviation (RMSD) between the whole catalytic domains of GppNHp- and GDP-bound H-Ras is 1.58 Å for the backbone heavy atoms. The overall three-dimensional (3D) structures of K-Ras4B catalytic domain complexed with GppNHp (PDB ID 3GFT) and GDP (PDB ID: 4LPK) are similar to the corresponding structures of GppNHp- and GDP-bound H-Ras (Figures 2.4 A and 2.4 B). Backbone superimposition of the crystal structure of GppNHp-bound K-Ras4B onto that of GppNHp-bound H-Ras yields a backbone RMSD of 0.96 Å and the RMSD between GDP-bound K-Ras4B and H-Ras is 0.97 Å for the backbone atoms.

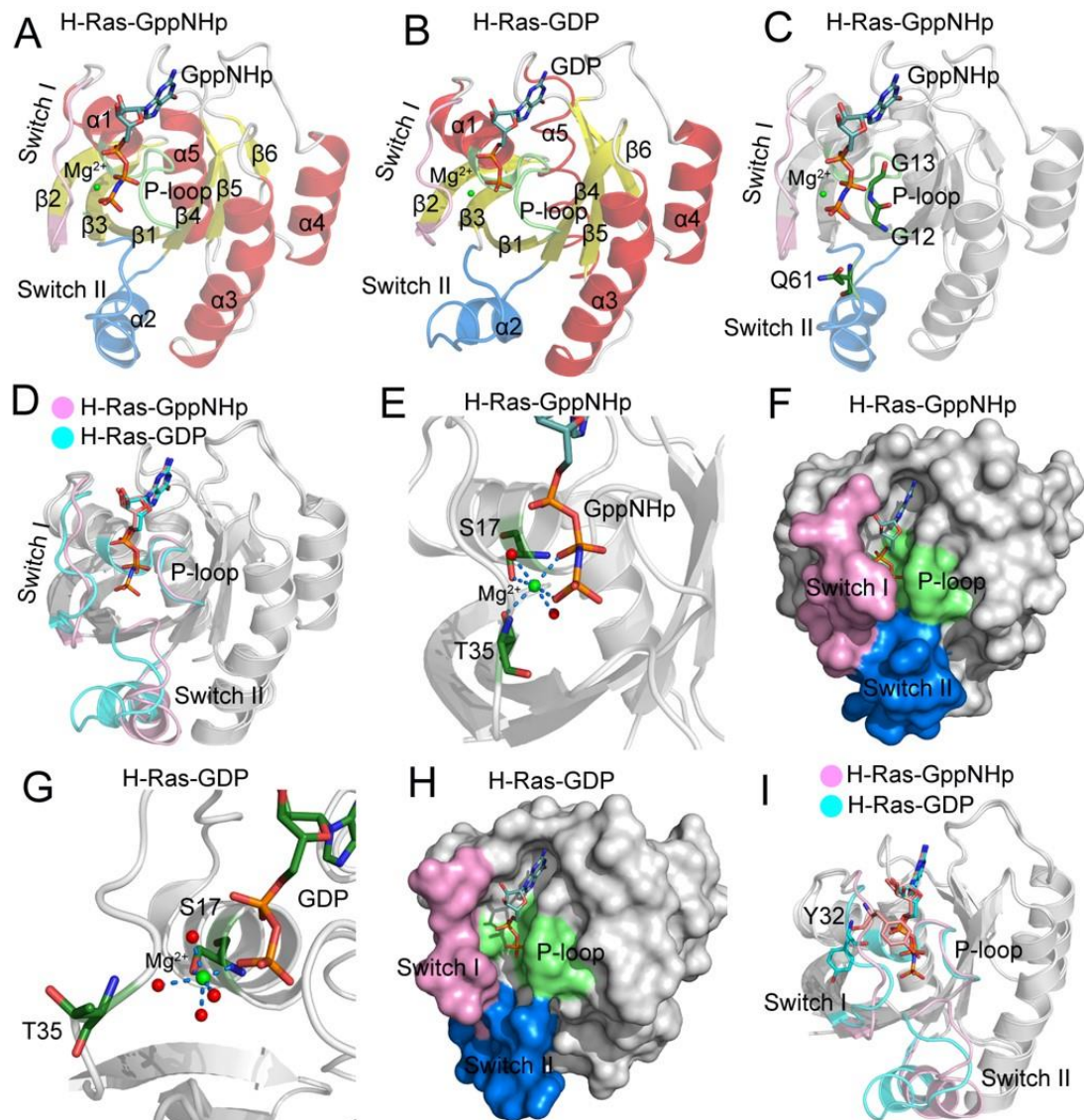


Figure 2.3. Cartoon representation of H-Ras crystal structures. **(A)** Cartoon representation of crystal structure of GppNHp-bound H-Ras (PDB ID 5P21). The helices, strands and loops are colored in red, yellow and gray, respectively. The P-loop, switch I and switch II regions are colored in lime, pink and blue, respectively. GppNHp and Mg²⁺ are depicted by stick models and a green sphere, respectively. **(B)** Cartoon representation of crystal structure of GDP-bound H-Ras (PDB ID 4Q21). **(C)** The positions of the three most frequently oncogenic mutated residues, G12, G13, and Q61, in the GppNHp-bound H-Ras. **(D)** Stereo representation of the backbone superimposition of crystal structure of GppNHp-bound H-Ras (*pink*) onto that of GDP-bound H-Ras (*cyan*). **(E)** The coordination modes of Mg²⁺ in the GppNHp-bound H-

Ras. **(F)** Surface representation of GppNHp-bound H-Ras. **(G)** The coordination modes of Mg²⁺ in the GDP-bound H-Ras. **(H)** Surface representation of GDP-bound H-Ras. **(I)** The different orientation of Y32 between GppNHp- (*pink*) and GDP-bound H-Ras (*cyan*). Y32 is depicted by stick models [48].

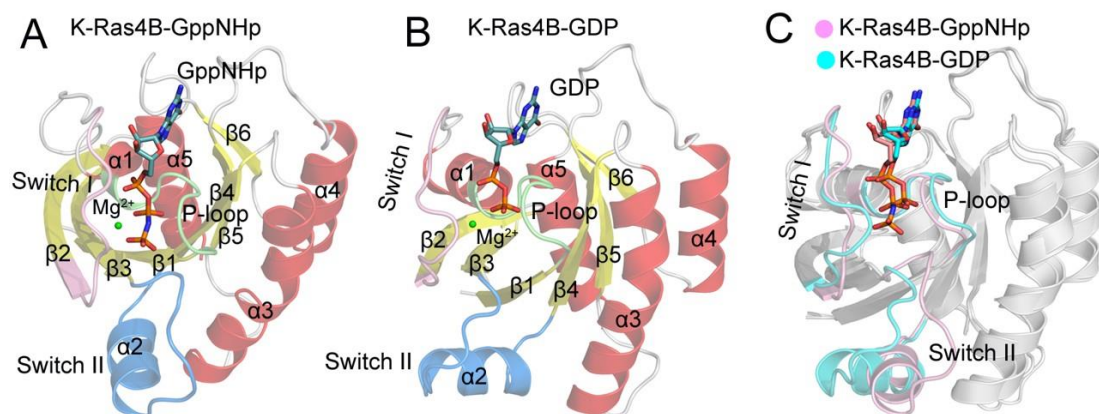


Figure 2.4. Cartoon representation of K-Ras4B crystal structures. **(A)** Cartoon representation of crystal structure of GppNHp-bound K-Ras4B (PDB ID 3GFT). **(B)** Cartoon representation of crystal structure of GDP-bound K-Ras4B (PDB ID 4LPK). **(C)** Stereo representation of the backbone superimposition of crystal structure of GppNHp-bound K-Ras4B (*pink*) onto that of GDP-bound K-Ras4B (*cyan*) [48].

Despite the homology, Ras isoforms are not functionally redundant [57]. The C-terminal 22 or 23 amino acids of the HVR are probably responsible for the biological differences across Ras isoforms because this is the only region that differs markedly in sequence among them (Figure 2.2). As such individual HVRs represent distinct preferred conformational states and interactions and may provide clues for isoform-specific differences in network signaling and oncogenic potential [58]. The C-terminal protein sequences conserved in the HVR CAAX motif (C, cysteine; A, aliphatic amino acid; X, any amino acid) [59-61], are necessary for Ras recruitment to the inner PM for normal biological function [62-64]. Mutation of the CAAX motif in the HVR has been demonstrated to demolish PM localization and Ras signaling [65]. The initial triplet of modifications of the CAAX motif is a prerequisite for all Ras proteins, encompassing

farnesylation at cysteine within the CAAX motif, AAX proteolysis, and carboxyl methylation of the resulting C-terminal prenylcysteine [66, 67]. In order to insert the HVR into the PM, Ras proteins require a second signal. The HVR of K-Ras4B contains multiple lysines (K175-K180) that serve as a polybasic stretch, which is capable of associating with the negatively charged phospholipids in the inner PM leaflet of acidic membranes through electrostatic interactions. H-/N-Ras and K-Ras4A carry additional palmitoyl moiety on cysteine residues (C181 and C184 for H-Ras; C181 for N-Ras; C180 for K-Ras4A) within the HVR, immediately proximal to the CAAX motif [68, 69]. Palmitoylation strengthens the lipophilicity of the HVR and enables association with a zwitterionic PM. Its linkage to the HVR is reversible unlike farnesylation.

2.4. Plasma Membrane and Ras Signaling

Ras proteins are preferentially located at different membrane microdomains, supporting functional specificity [70]. H-Ras is targeted towards the cholesterol-rich microdomains (lipid rafts and caveolae) [70]. N-Ras is also found at the lipid rafts in the PM, but does not associate with caveolae [71]. Ras localization, however, is dynamic and largely relies on the activation state of these proteins. Active H-Ras, for instance, redistributes from lipid rafts to bulk plasma membrane [69, 72, 73]. Active N-Ras, on the other hand, redistributes in the opposite direction [69]. K-Ras is localized outside of lipid rafts and this localization is nucleotide-independent [72]. In addition, K-Ras can aggregate at the anionic lipid phosphatidylinositol-4,5-bisphosphate (PIP₂), a substrate for the Ras effector PI3K, due to its polybasic domain [74]. Phosphorylation of the residues located within the polybasic region can also alter K-Ras localization. PKC-mediated phosphorylation of S181, for example, induces translocation of K-Ras from PM to different intracellular compartments like ER, Golgi, and mitochondria [75].

Ras proteins have different degrees of access to GEFs, GAPs, and effectors in various microdomains [76]. This differential access idea can explain isoform-specific signaling of Ras. For example, H-Ras activates PI3K to a greater extent than K-Ras4B whereas

K-Ras4B is responsible for activation of Raf-1 [57]. Although the membrane localization pattern of PI3K has not been studied, PIP2 is found in the inner leaflet of membrane microdomains [77]. These PIP2 microdomains can be cholesterol independent and distinct from rafts. It is conceivable that PI3K may co-localize with its substrate PIP2 in these microdomains. Incidentally, H-Ras nanoclusters are enriched in phosphatidylinositols [78]. K-Ras-GTP is similar to H-Ras-GTP in its ability to form nanoclusters on PIP3-rich intact plasma membrane sheets [78]. However, K-Ras-GTP nanoclusters are enriched in phosphatidic acid to a greater extent than either H-Ras-GTP or H-Ras-GDP nanoclusters [79]. Co-localization of K-Ras with phosphatidic acid is consistent with K-Ras's preferential activation of Raf, which has a phosphatidic acid binding domain [80].

The extent of co-localization of Ras isoforms with their corresponding receptor complexes on particular membrane microdomains determines the differences in activation by Ras isoforms. K-Ras on disordered microdomains becomes efficiently activated in growth factor dependent cell lines because epidermal growth factor receptors and components of the activated receptor complex, including GEFs like SOS, also partition to the disordered microdomains [81]. Conversely, H-Ras or N-Ras bound to lipid rafts are less active in these cells.

2.5. Shuttling of Ras Proteins

Attachment of Ras superfamily proteins to PM is essential for their function [82]. To gain full biological activity, following their synthesis as soluble precursors, Ras superfamily proteins undergo a series of post-translational modifications (PTMs) [83-87]. Ras prenylation involving farnesylation and geranylgeranylation is crucial for membrane signaling and trafficking [88].

Signaling by the prenylated proteins like Ras and Rho relies on their subcellular distribution and localization [89]. There is evidence that farnesylated and palmitoylated H-Ras,

N-Ras, and K-Ras4A proteins, but not K-Ras4B, are vesicle-transported from the Golgi complex to the PM [89, 90]. On the other hand, K-Ras4B is transported to the PM through a non-vesicular, diffusional mechanism. This intracellular diffusion is a slow process and inward membrane flow of endocytic vesicles counteracts this movement to randomize Ras distribution over all membranes [91]. Studies involving inhibition or knock down of the delta subunit of the cGMP phosphodiesterase from retinal rod cells (PDE δ) indicated that PDE δ is essential for the dynamic shuttling of polybasic-stretch-containing K-Ras4B [92]. PDE δ can interact with prenylated proteins, such as K-Ras, H-Ras, and Rheb, and assist in their trafficking through the cytosol between different membrane compartments [93-97]. PDE δ increases the kinetics of trapping and thereby counteracts the entropic tendency of the membranes to randomly distribute Ras over all membranes and maintain K-Ras4B localized enrichment at the PM [89, 93, 98, 99].

PDE δ shares a significant structural similarity with RhoGDI, a guanosine nucleotide dissociation inhibitor (GDI) responsible for intracellular trafficking of Rho proteins [100, 101]. It features a hydrophobic prenyl-binding pocket into which prenylated small G-proteins insert their farnesylated C-terminus. This facilitates the intracellular diffusion of these proteins by shielding the hydrophobic prenyl moiety from the cytosol. However, the prenyl binding pocket of PDE δ is much shorter than the RhoGDI binding pocket resulting in a weaker interaction between PDE δ and geranylgeranylated proteins [93, 94, 96]. PDE δ also lacks an N-terminal helix-loop-helix that can interact with the GTPase switch regions. Consequently, unlike RhoGDI binding, PDE δ binding to prenylated proteins is nucleotide-independent [94, 95]. PDE δ appears more promiscuous in terms of ligand specificity and can associate with various prenylated proteins including protein kinases, PDE subunits, and GTPases. In addition to these proteins, PDE δ associates with two non-prenylated small G proteins, Arl2 and Arl3 from the Arf family. These post-translational modifications-independent interactions involve the switch regions and are specific to the GTP-bound state, hence classifying PDE δ as an Arl2 and Arl3 effector [94, 102, 103].

Biochemical studies indicate that PDE δ binds more strongly to farnesylated proteins such as Rheb and K-Ras4B than other prenylated proteins and the binding stoichiometry is 1:1 [93, 96]. Binding of Rheb to PDE δ occurs mainly through the farnesylated C-terminus. Unlike the Rho/RhoGDI interaction, the interaction between Rheb and PDE δ does not involve the switch regions of Rheb [101, 104, 105]. Additionally, the farnesyl group together with the last three residues penetrates much more deeply into the hydrophobic pocket than RhoGDI. This presumably compensates for the weaker contacts with the rest of the protein. Binding of K-Ras4B to PDE δ also occurs mainly through the farnesylated and methylated C-terminus of the hypervariable region (HVR) and is enhanced by the negatively charged surface of PDE δ and the positively charged C-terminus of K-Ras4B HVR, with no additional contacts between PDE δ and the catalytic domain of K-Ras4B [97, 106].

2.6. Ras-effector Interactions

In the active GTP-bound state, Ras can associate with its downstream effectors [107-109], including Raf kinase, PI3K, and RalGDS, thereby activating several signal transduction pathways in the cell. All reported Ras effectors contain a conserved structural domain referred as the RBD, which binds to Ras in a nucleotide-dependent manner [110]. Ras-GTP strongly interacts with RBD with dissociation constants (K_d) in the range of 0.01-3 μ M [111]. In contrast, in the inactive GDP-bound state, Ras weakly interacts with RBD with K_d values in the upper micromolar range, which decreases by approximately 1000-fold compared with the binding affinities of Ras-GTP to Ras effectors [112]. In this context, Ras-GDP loses its ability to interact with Ras effectors. To date, several crystal structures of Ras in complex with RBD of Ras effectors in the GppNHp-bound states have been solved, providing a detailed insight into the interactions between Ras and RBD [113].

2.6.1. Interaction with Raf

Mammals express three Raf paralogs (A-Raf, B-Raf, and C-Raf), which participate in the Ras-Raf-MEK-ERK signal transduction cascade [114]. Each of the Raf isoforms contains three conserved regions (CR) [115]: CR1, CR2, CR3. CR1 consists of a RBD and a cysteine-rich domain (CRD), which can bind two Zn^{2+} ions. CR2 is a serine/threonine rich domain, which can bind to 14-3-3, a regulatory protein. CR3 is the kinase domain, which is located near the C-terminus. Previously, yeast two-hybrid and *in vitro* binding studies ascertained that the RBD (residues 55-131) of C-Raf (also known as Raf-1) (hereafter referred as RafRBD) directly interacts with the H-Ras-GTP [116-118]. Furthermore, mutational analyses showed that only mutations such as E31, T35, and E37 in the switch I region of H-Ras significantly impair the association of RafRBD to mutant H-Ras, suggesting that the switch I region of H-Ras directly interacts with RafRBD [119]. Fetics *et al.* [120] solved the first crystal structure of the complex between H-Ras^{WT}-GppNHp and RafRBD (PDB ID 4G0N), together with the complex between the oncogenic H-Ras^{Q61L} mutant bound to GppNHp and RafRBD (PDB ID 4G3X). They showed that Switch II region of oncogenic H-Ras^{Q61L} mutant becomes more rigid relative to the wild-type in the presence of Raf,

2.6.2. Interaction with PI3K

Class I PI3Ks, the best physiologically, biochemically, and structurally characterized kinase of PI3K family, consists of four isoforms, α , β , γ and δ [121]. Each isoform is a heterodimer that comprises a p110 catalytic subunit and a p85 regulatory subunit [122, 123]. The overall organization of the p110 catalytic subunit is highly conserved, including an N-terminal adaptor-binding domain (ABD) (residues 34-141), a Ras binding domain (RBD) (residues 217-309), a C2 domain (residues 357-521), a helical domain (residues 541-723), and a catalytic domain (residues 828-1073). Biochemical studies have well-documented that all class I PI3Ks bind Ras in a GTP-dependent manner [124-127]. However, the binding affinity of PI3Ks to Ras is significantly weaker than that of Raf to Ras. In 2000, Pacold *et al.* [128] solved the first co-crystal structure of the complex between the oncogenic H-Ras^{G12V} bound to GppNHp and the catalytic subunit of PI3K γ ^{V233K} (PDB ID 1HE8). In the binding interface, PI3K γ interacts mainly

with the switch I region of H-Ras^{G12V} and the strand β 2 of H-Ras^{G12V} forms an anti-parallel β -sheet with the β 2 of PI3K γ ^{V233K}. The interaction of the switch I region of H-Ras^{G12V} with the PI3K γ -RBD contributes to the ordering of a loop, residues 255 to 267, in the RBD.

2.6.3. Isoform-specific interactions

Most Ras binding partners including Raf and PI3K can interact with all Ras isoforms. However, distinct Ras isoforms have unique physiological functions with individual isoforms associated with different cancers and developmental diseases [129]. These functional differences among Ras isoforms arise from involvement of specific binding partners. Recent evidence suggests that only GTP-loaded K-Ras4B can bind to Calmodulin (CaM) in a Ca²⁺-dependent manner [130]. The main driving force is the electrostatic interaction between calmodulin and the HVR; however, docking of the farnesyl into a calmodulin pocket further stabilizes the interaction [131, 132]. Though the HVR is the primary binding site for CaM, the inability of HVR to mimic the interactions between full-length K-Ras4B and CaM completely suggests that Ras catalytic domain is also involved [131]. Ca²⁺/CaM regulate K-Ras4B signaling through the Raf/MEK/ERK and PI3K/Akt pathways (Figure 2.5). Activation of these pathways can elicit different, sometimes sequential or opposite, biological responses including cell proliferation, differentiation, and oncogenic transformation. CaM was shown to directly activate PI3K α and proposed to form a complex with K-Ras4B and PI3K α [133-135]. Normally, PI3K α is recruited to the membrane with the help of activated tyrosine kinase receptors (RTKs). However, when K-Ras4B is activated by oncogenic mutations, calmodulin can substitute for the RTK signal, to achieve full activation of the PI3K α . CaM also acts in down-regulation of the ERK1/2 pathway at low serum concentration [130, 136]. Thus, CaM defines a threshold to prevent the activation of ERK1/2 pathway under basal conditions. CaM also acts to prevent a too-sustained high activation of ERK1/2 upon growth factor stimulation, allowing a proliferative effect of the ERK1/2 pathway [130, 136]. K-Ras activation induced by CaM inhibition is protein kinase C (PKC)-dependent, with strong synergism between CaM inhibition and PKC activation. PKC phosphorylates K-Ras Ser181, and positively modulates K-Ras activity. CaM also

binds to active K-Ras and prevents its phosphorylation by PKC in serum-starved cells. Taken together, these data suggest an interplay between CaM binding to K-Ras, K-Ras phosphorylation and activity [130, 137]. This reciprocal regulation of K-Ras by CaM and PKC is essential when cells need to uncouple PKC activity and K-Ras activation to prevent an excessively sustained ERK activity. Treatment of fibroblast cells with CaM inhibitors blocks growth factor-dependent migration and Akt activation. The involvement of both CaM and K-Ras4B in the activation of Akt together with the observation that CaM specifically interacts with active K-Ras4B [131, 137, 138] suggest a key CaM role in this isoform-specific activation.

Calmodulin's binding to the HVR of GTP-bound K-Ras4B shifts the equilibrium from membrane-bound K-Ras4B to the unbound state, thus, temporally downregulates Raf's activation. Due to its activation of the PI3K α /Akt pathway in the absence of a signal from RTK, calmodulin plays a critical role in K-Ras-driven cancers [139]. The high calcium levels observed in these cancers may explain calmodulin's role in recruiting and activating PI3K α . Without RTK signals, oncogenic mutations in K-Ras can activate PI3K α , but are unable to achieve full activation; thus they may lead to oncogene-induced senescence (OIS) or to proliferation and differentiation [140]. Calmodulin can fully activate PI3K α through two mechanisms: first, binding to PI3K α 's nSH2 domain substituting for the pYXXM motif of activated RTKs. This action relieves the steric autoinhibition action of the nSH2 domain on the catalytic p110 subunit, and second, acting to allosterically activate PI3K α through binding to the cSH2 domain of its p85 subunit.

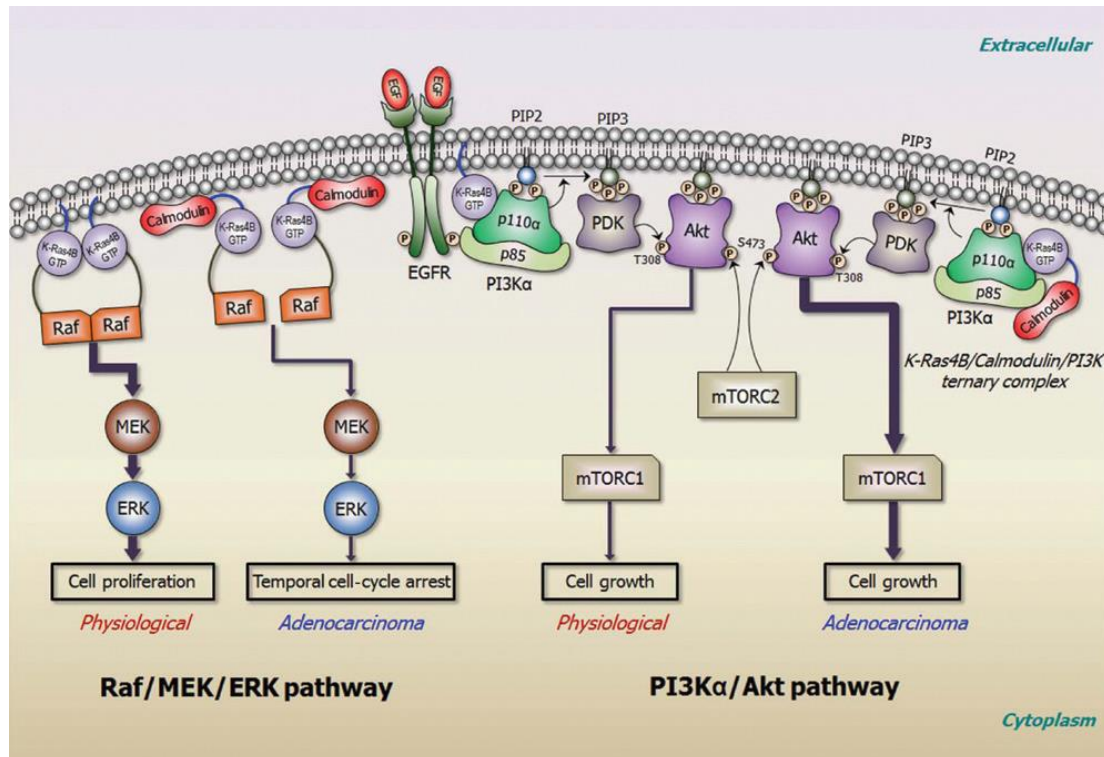


Figure 2.5. Differential effects of calmodulin on two key K-Ras4B effector pathways. Calmodulin (CaM) binding to K-Ras4B-GTP downregulates the Raf/MAPK kinase/extracellular signal-regulated kinase (Raf/MEK/ERK) pathway. Raf/MAPK signaling and calmodulin's upregulation of PI3K result in proliferative effect through inducing the expression of cyclin D1, a G1–S–specific cyclin, which is essential for cell-cycle progression. Cyclin D1/cyclin-dependent kinase 4 (CDK4) complex phosphorylates and inhibits retinoblastoma (RB) protein and regulates G1–S transition. Binding of calmodulin to K-Ras4B-GTP activates the PI3K/Akt (also known as protein kinase B, PKB) pathway and enhances cell migration. The thick and thin arrows indicate upregulated and downregulated pathways, respectively [139].

2.7. Ras Signaling Pathways

Two of the main Ras signaling pathways are mitogen-activated protein kinases (MAPK) and phosphoinositide-3 kinase (PI3K) pathways (Figure 2.6). MAPK and PI3K pathways are the cell's key mechanisms for controlling cell survival, proliferation, and motility [141-144]. Ligand binding to a receptor tyrosine kinase (RTK) is the first step

towards activating these pathways. Epidermal growth factor (EGF) binding to the extracellular domain of RTKs such as epidermal growth factor receptor (EGFR), results in dimerization and activation of EGFR. The activated EGFR recruits Ras-specific guanine nucleotide exchange factors (GEFs) [e.g., SOS (Son of sevenless)] via the adaptor proteins SHC (SHC-transforming protein) and Grb2 (growth factor receptor-bound protein 2). SOS exchanges GDP by GTP and activates Ras. In the MAPK pathway, activated Ras recruits a MAP kinase kinase kinase (Raf) to the cell membrane and activates its kinase domain by promoting Raf side-to-side dimer formation [145-147]. Active Raf then initiates a protein kinase cascade leading to an activation of a MAP kinase, ERK1 [148, 149]. PI3K, on the other hand, can be activated by three independent pathways. The first one involves direct binding of the regulatory subunit of PI3K to phospho-YXXM motifs (in which X indicates any amino acid) within receptor tyrosine kinases (RTKs) [150]. The second pathway utilizes the adaptor proteins such as GRB2 [151]. Finally, the third way to activate PI3K is through a direct interaction with Ras [152]. Active Ras binds and activates PI3K that converts phosphatidylinositol (4,5)-bisphosphate (PIP₂) into phosphatidylinositol (3,4,5)-trisphosphate (PIP₃). PIP₃ serves as a plasma membrane docking site for the pleckstrin homology (PH) domain of Akt/PKB and its upstream activator PDK1 [153]. Phosphorylation of Akt at Thr308, and Ser473 by PDK1 and mTORC2, respectively, leads to the full activation of Akt [154].

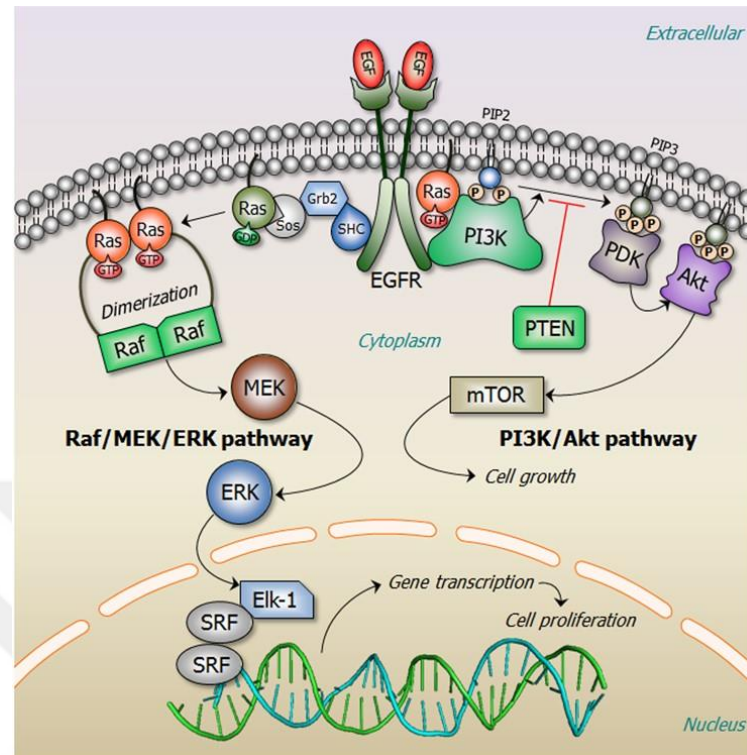


Figure 2.6. Ras signaling in the mitogen-activated protein kinase (MAPK), Raf-MEK-ERK pathway, and phosphatidylinositol 3-kinase (PI3K)/Akt pathway [48].

2.8. Ras Dimerization, Oligomerization and Clustering

The possibility of Ras existing in different oligomerization states at the plasma membrane has recently emerged as a new way of regulating Ras function. Ras dimers are observed by X-Ray crystallography. Lipidated N-Ras-GDP anchored to 1-palmitoyl-2-oleoyl-sn-glycero-3-phosphocholine (POPC) membrane was shown to dimerize utilizing dichroic ATR-FTIR spectroscopy, biomolecular simulations, and Förster resonance energy transfer experiments. Analyses of X-ray crystal structures and MD simulations indicate that the residues in helices α_4 , α_5 and the loop between β_2 and β_3 are crucial for dimerization [2]. Ras dimerization is important since it has been shown to play an essential role in Raf activation [155]. Inouye *et al.*[156] found that Ras incorporated into liposome can induce Raf-1 activation. Bifunctional cross-linker and a protein-fragmentation complementation assay confirm formation of Ras dimers in the liposome and in the intact cells, respectively. These results indicate the necessity of Ras dimerization in the lipid membrane for activation of Raf-1. Lin *et al.*[3] demonstrated

that H-Ras can form dimers, but not higher-order oligomers on supported lipid bilayers using a combination of time-resolved fluorescence spectroscopy and microscopy. Additionally, they showed that mutation of Y64 located at the switch II region to alanine interferes with dimerization suggesting that switch II region is either part of the dimer interface or has an allosteric effect on dimerization [3]. Using biophysical experimental techniques in combination with a template-based protein-protein complex structure prediction algorithm (PRISM), we showed that GTP-bound K-Ras4B forms stable homodimers [157]. We predicted two major dimer interfaces, β -sheet and helical. A study by Nan *et al.* demonstrated that active Ras forms dimers to activate Raf. Using quantitative photoactivated localization microscopy (PALM), they showed that K-Ras4B forms dimers and higher order clusters on the cell membrane; dimers, however, remain the predominant form of clusters at endogenous expression levels. Additionally, they found that the CAAX motif in the HVR is crucial for dimerization as mutation of cysteine to serine prevents the activation of MAPK even in the presence of a small molecule dimerizer. This observation suggests that the HVR in addition to its known function in membrane localization may have a role in protein dimerization in cells [158, 159]. A recent study by Prakash *et al.* [160] also identifies two partially overlapping dimerization interfaces ($\alpha 3/\alpha 4$ and $\alpha 4/\alpha 5$) for K-Ras utilizing protein-protein docking and molecular simulations. Using mutagenesis, electron microscopy, and biochemical assays they show that charge reversal mutations at positions 101 and 107 (K101E and E107K) reduce K-Ras clustering and dimer fraction. Spencer-Smith *et al.* [161] show that a synthetic binding protein, designed specifically for binding to the $\alpha 4$ - $\beta 6$ - $\alpha 5$ region of H- and K-Ras, disrupts Ras dimerization, thus blocks oncogenic H- and K-Ras-mediated signaling and transformation. These studies identified contributions from the catalytic and HVR domains in dimer formation. The contribution of HVR to K-Ras4B dimerization is consistent with the involvement of the farnesyl group of HVR peptides in cooperative dimerization and binding to phospholipid bilayers.

Ras proteins bind POPC bilayers as dimers or oligomers, in an orientation perpendicular to the membrane surface. Although simulations point to a dimer, it has been proposed

that oligomerization due to diffusion limited partner switching of dimers cannot be excluded [162]. K-Ras4B forms nanoclusters that are membrane-anchored through a farnesylated HVR. Anchoring stabilizes the Ras dimers, increasing the Ras effective local concentration and favorably orienting the catalytic domain. The formation of large, activated Ras signaling complexes has also been observed by Murakoshi *et al.* using single molecule FRET in KB cells [163]. These large, activated signaling complexes recruit GAP molecules to the membrane, which then catalyze GTP hydrolysis and cause dissociation of the complexes. These results suggest that GDP-bound Ras is less prone to oligomerization [164]. However, several publications propose the formation of Ras-GTP as well as Ras-GDP nanoclusters, which are spatially distinct for each isoform [79]. Methodological differences used by different labs may have led to alternate conclusions regarding the existence of Ras-GDP oligomers. Murakoshi *et al.* use FRET to study the formation of complexes whereas the Hancock group employs EM on immunogold labeled plasma membrane sheets and mathematical models toward the same aim. Electron microscopy and single fluorophore tracking indicate that Ras proteins are arrayed in nanoclusters on the inner plasma membrane [73, 164-166]. These nanoclusters are formed through the assembly of the lipid-anchored Ras proteins into transient dynamic structures. They contain 6–8 Ras proteins with a diameter of 12–22 nm, and are highly dynamic structures since each cluster turns over on average every 0.4 s. Each Ras isoform occupies spatially distinct nanoclusters and about 40% of any Ras isoform is arrayed in these nanoclusters [73].

Despite the advances in single molecule imaging techniques, the exact mechanism of Ras dimerization and clustering is not fully understood. Computer simulations suggest that lipid anchors in the HVR of H-Ras and N-Ras are capable of forming dimers and nanoclusters [2, 3, 167]. In-cell studies of the K-Ras lipid anchor using Homo-FRET and electron microscopy also demonstrate that the lipid anchor is sufficient for dimerization and clustering on the membrane [168]. How can the HVR, - that is not involved in nucleotide binding or hydrolysis - affect dimer and nanocluster formation in a nucleotide dependent manner? It is possible that the catalytic domain of Ras has a way

to communicate with the HVR. Intriguingly, a conserved water-mediated hydrogen-bonding network linking the nucleotide sensor residues R161 and R164 on helix 5 to the active site was discovered in Ras-GTP but not in Ras-GDP [169]. This hydrogen-bonding network might relay the conformational changes induced by nucleotide binding to helix 5 and subsequently to the directly linked HVR. In this way, the nucleotide-induced conformational changes can affect membrane binding, dimerization and clustering of Ras. Alternatively, nanoclustering of Ras can be mediated by nucleotide dependent interactions with scaffold proteins, such as galectin [170]. Finally, it is also possible that the catalytic domain of Ras is directly involved in nucleotide-dependent dimer formation and clustering.

Ras nanoclusters function to efficiently recruit effectors for signaling pathways. The propensity to form nanoclusters is a direct function of the concentration of EGF upon stimulation. As confirmed by single particle tracking, Raf is recruited from the cytosol to Ras clusters [164, 166]. The association of MEK with both Raf and ERK ensures the recruitment of the entire MAP kinase cascade to Ras nanoclusters [171-173]. Studies confirm the significance of Ras nanoclusters in MAPK activation; blocking nanocluster formation disrupts Ras-dependent MAPK signaling [174-176]. In line with this, *in silico* abrogation of Ras nanoclusters leads to failure of Raf recruitment [177]. Importantly, the signal output decreases to 3% of its maximal value when Ras proteins function as individual molecules rather than as nanoclusters [165, 177]. A decrease in Ras clustering diminishes the target area of the plasma membrane available for Raf-MEK-ERK recruitment, which in turn, decreases the probability of successful recruitment and activation. Conversely, K-Ras nanoclustering can be increased by membrane depolarization that causes reorganization of phosphatidylserine and PIP2 and amplifies MAPK signaling [178]. Collectively, these data confirm that cell signaling relies on the formation of functional Ras nanoclusters at the plasma membrane, similar to other membrane-anchored signaling platforms, and suggest that cells can adjust their response to the environmental stimuli by regulating the extent of Ras clustering [179]. Interestingly, Raf dimerization enhanced by Raf inhibitors increases Ras

clustering, suggesting a possible role of effectors in stabilizing Ras oligomers on the plasma membrane [180].

In conclusion, the diverse plasma membrane microdomains appear to play a decisive role in regulating Ras signaling. Membrane association limits the accessibility of Ras to its effectors and allosterically alters the conformation of Ras and its oligomerization state. In this way, diversity of Ras signaling responses can be achieved and optimized across Ras isoforms. It is quite possible that the number and distribution of membrane microdomains are affected through cellular mechanisms, which include endosomal trafficking and lipid sorting. Importantly, membrane organization can be controlled extracellularly, for example, by growth factor binding to its receptor or by pharmacological agents. Understanding how regulation of Ras signaling happens at the membrane will offer new opportunities for anti-cancer drug design.

2.9. Main contributions

Ras proteins bind and activate many effectors and, as a result, mediate a wide variety of cellular functions. So general interference with Ras function would have serious consequences. Screening of human tumor cell lines indicate that activating mutations in Ras genes are present in approximately 30% of metastatic human cancers [181, 182]. Despite the decades of extensive research, no effective small-molecule Ras inhibitor has been identified indicating that direct targeting of Ras is a very challenging task. Thus, Ras community seek different approaches like targeting the downstream Ras effector pathways and preventing its membrane localization.

Ras is functional as a monomer. However, studies indicating that Ras can form dimers on the plasma membrane and Ras dimerization plays a key role in Raf activation have shifted the focus towards the identification of the oligomerization state of Ras. To elucidate the structural details of Ras oligomerization, and discover the effects of Ras dimerization on effector binding and activation, H-Ras and K-Ras4B dimer/tetramer structures were predicted and the effect of Ras dimerization on MAPK pathway was investigated by combining computational and experimental methods.

Raf, PI3K and RalGDS are major Ras effectors. They bind at the same Ras site. What decides the cell selection among them? This temporal and spatial decision is critical since the signaling pathways that they elicit oppose each other. Elucidating the structural details of Ras/effector interactions can help us understand the cell decision. However, only a few of the Ras/effector complexes have crystal structures in PDB. Here, the 3D structures of Ras/effector complexes were predicted and binding sites other than the effector binding regions on Ras were identified. The effectors were also classified according to the binding regions on Ras to determine which pathways are competitive.

Ras is functional when it is membrane-attached. Thus, after its synthesis as a soluble precursor, it undergoes a series of PTMs and is shuttled to the PM. PDE δ is responsible for the shuttling of K-Ras4B. Studies indicate that PDE δ can bind to K-Ras4B, and N-Ras, but not to K-Ras4A, although K-Ras4B and K-Ras4A are quite similar both sequence- and structure-wise. K-Ras4B/PDE δ and the HVRs of N-Ras and K-Ras4A with PDE δ were simulated to unravel these puzzling observations.

The models introduced in this dissertation may assist structure-based drug design studies for oncogenic Ras, thus cancer. Disruption of some of the predicted interactions by drugs or mutations may abate Ras signaling or interfere with its membrane localization, hence, contribute to indirect targeting of Ras.

Chapter 3

MATERIALS and METHODS

3.1. Computational Prediction of the Structures of H-RAS and K-RAS4B Dimers

In this study, an accurate template-based protein-protein complex structure prediction algorithm, PRISM [183-185], was used to predict models for the dimeric and tetrameric structures of the Ras protein. PRISM is based on our observation that protein-protein interface motifs are conserved in nature, similar to single chain architectures. PRISM uses the tertiary structure of proteins of interest to build models. The solutions are optimized by a docking refinement protocol and ranked based on the binding energy scores (BES) computed by FiberDock [186], which has been implemented in PRISM. PRISM has been tested extensively for a range of proteins and pathways. Its accuracy has been demonstrated [187]. The structural data for the dimer predictions (target proteins) have been obtained from the PDB. These predictions are then used to build and assess models for Ras tetramers. G-domains (corresponding to Ras residues 4-166) of both H- and K-Ras were used as target proteins. K- and H-Ras catalytic domains have 10 and 115 structures in the PDB, respectively. They include GDP- and GTP-bound conformations. All K-Ras structures were included in the predictions. For H-Ras, only X-ray structures with resolution of 2.00 Å or lower were considered. To reduce the redundancy due to very similar interface architectures, the root mean squared deviation (RMSD) was calculated for each pair. For structures with RMSD below 0.25 Å, a representative with the highest resolution was chosen. In this way, the number of structures for H-Ras was reduced to 46. Figures B.1 and B.2 show the superimposed H- and K-Ras structures, respectively. Then, the interface regions of the putative dimers were identified using the HotRegion [188]. HotRegion is a database of predicted hot spot clusters. It identifies the regions that are important for the stability of protein complexes by using predicted hot spot residues, major contributors to the binding energy. The results were compared with crystal structures to further affirm our predictions. Evolutionary Protein-Protein Interface Classifier (EPPIC) [189] Server was

used to classify the crystal interfaces in Ras structures.

3.1.1. Determination of the residues to be mutated

The atomic interactions in the GTP-bound H-Ras and K-Ras4B homodimers were analyzed to narrow down the number of the interface residues to be mutated. Then the change in binding free energy ($\Delta\Delta G$) upon mutation was computed using FoldX [190]. FoldX uses an empirical method to estimate the stability effect of a mutation. A mutation that increases energy ($\Delta\Delta G > 0$ kcal/mol) will destabilize the structure, while a mutation that decreases energy ($\Delta\Delta G < 0$ kcal/mol) will stabilize the structure. A common threshold is to say that a mutation has a significant effect if $\Delta\Delta G$ is > 1 kcal/mol, which roughly corresponds to a single hydrogen bond.

3.2. Confirmation of the Predicted Interface Residues Involved In Dimerization by Bimolecular Fluorescence Complementation (BiFC)

3.2.1. Cloning strategy for BiFC system

Human *HRAS* and *KRAS* genes were amplified by polymerase chain reaction (PCR) from pMXs-hs-*HRAS* (Addgene ID: 52730), and pMXs-hs-*KRAS4b* – (Addgene ID: 52729), respectively. Similarly, VN173 and VC155 ORFs, the N and C terminal fragments of the Venus protein (an improved version of the yellow fluorescent protein, YFP), were amplified from pBiFC-VN173 (Addgene ID: 22010) and pBiFC-VC155 (Addgene ID: 22011) vectors, respectively. The oligonucleotide primers used for polymerase chain reactions (PCRs) are listed in Table A.1. The oligonucleotide primers of VN173 and VC155 have an additional cMyc and FLAG epitope, respectively, in order to be visualized by Western blot. The PCR conditions were applied as follows; initial denaturation at 98°C for 60 sec, annealing at 98°C, 15 sec; 54-62°C, 15 sec; 72°C 45 sec for 35 cycles, and final extension at 72°C for 5 min and the amplification was checked by agarose gel electrophoresis (Figure B.1). Then gel purification was applied to the PCR products. Purified PCR products were cloned into pJET1.2/blunt vector (Thermo Scientific) (Figures C.1 and C.2). DH5-alpha cells were transformed with these

constructs and grown on ampicillin (100 ug/mL) containing agar plates. The plasmids were isolated from the resulting colonies and cut with PstI/XbaI enzymes to verify the inserts (Figure 3.1).

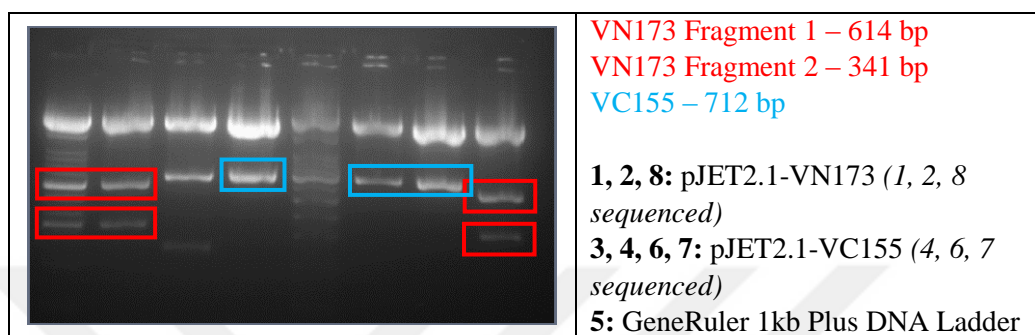


Figure 3.1. Diagnostic digest for VN173 and VC155 cloned into pJET2.1. The DNA marker is mixed with the sample in lanes 1 and 5.

To design the constitutively active forms of HRAS and KRAS proteins (HRAS^{G12V} and KRAS4B^{G12D}) site-directed mutagenesis (SDM) was performed. The oligonucleotide primers for site-directed mutagenesis are listed in Table A.2. The thermocycling conditions for the PCR were as follows: initial denaturation at 98°C for 2 min, annealing at 98°C, 30 sec; 54-62°C, 30 sec; 72°C 2.5 min for 20 cycles, and final extension at 72°C for 10 min and the amplification was checked by agarose gel electrophoresis (Figure B.4). Following the reaction, the products were digested with DpnI at 37°C for 3 hours. Then, DH5 α cells were transformed with these constructs and grown on ampicillin containing agar plates. The plasmids were isolated from the resulting colonies and cut with PstI/XbaI enzymes to verify the inserts (Figure 3.2).

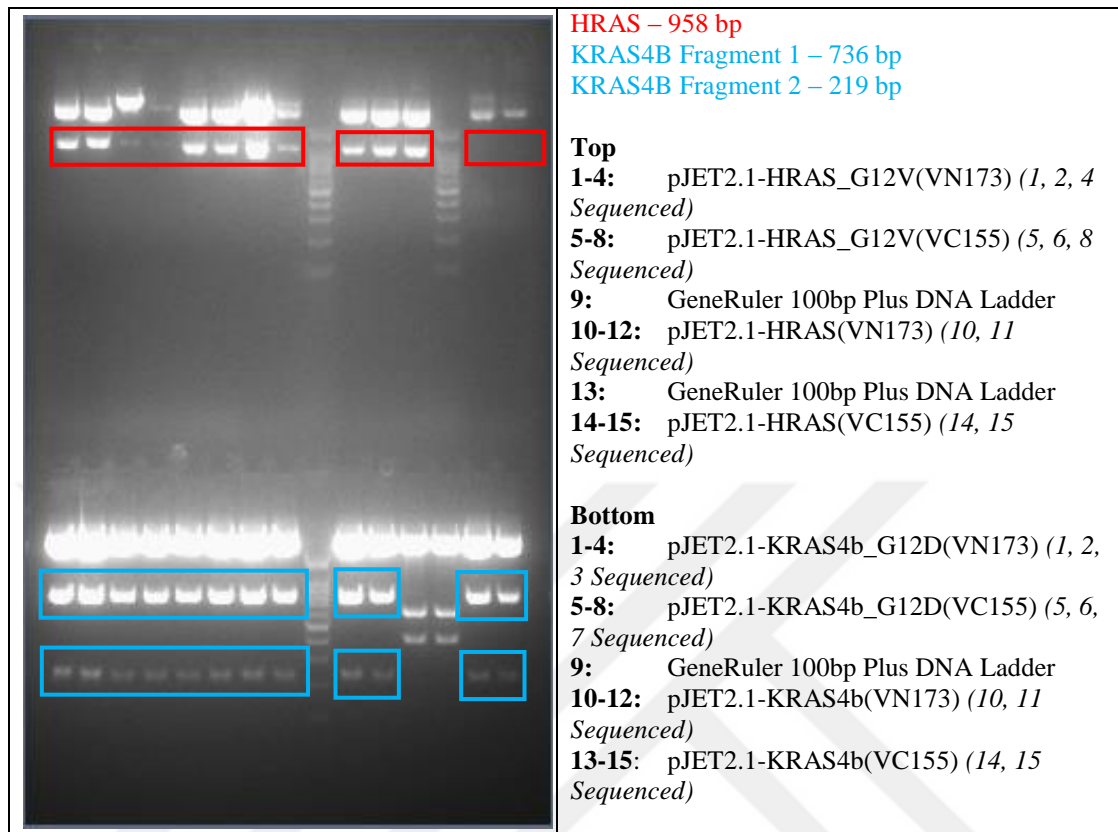


Figure 3.2. Diagnostic digest for wild type and constitutively active mutants ($HRAS^{G1V}$ and $KRAS4B^{G12D}$) of *HRAS* and *KRAS* genes cloned into pJET2.1.

Verified constructs were used to fuse RAS with Venus fragments on pJET2.1 vector. To this end, pJET2.1-*HRAS* (VN173), pJET2.1-*KRAS4b* (VN173) and pJET2.1-VN173 vectors were linearized by XhoI/KpnI digestion. Following the restriction reactions, pJET2.1-RAS (VN173), and VN173 DNA fragments were gel purified and ligated. The same approach was used for the ligation of VC155 with pJET2.1-Ras (VC155) vectors, but here, XhoI/BshTI were used for restriction. Figure C.3 shows the maps of the constructed plasmids. Constructed plasmids were verified for the inserts by diagnostic cut with PstI/HindIII enzymes (Figure 3.3).

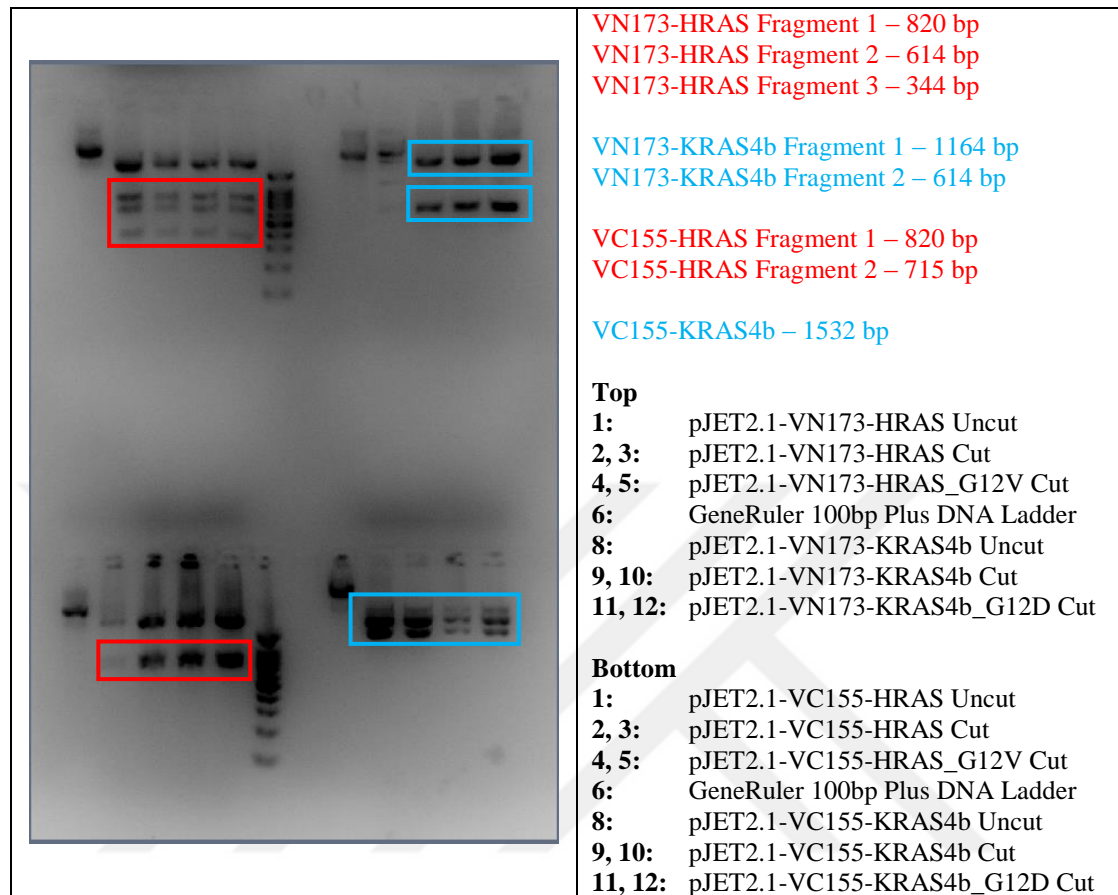


Figure 3.3. Diagnostic digest results for the wild type and mutant Venus-Ras plasmids. All results are positive except the pJET2.1-VN173-KRAS4b sample in lane 9.

The last step of the cloning involved the ligation of the RAS/Venus fragments with pTRE-Tight-BI vectors kindly provided by Assoc. Dr. Nuri Öztürk, Gebze Technical University. Unlike pJET2.1, pTRE-Tight-BI is a low copy plasmid and consists of two SV40 polyadenylation (polyA) signals that render the plasmid more susceptible to unwanted recombination event. Stbl3 *E. coli* strain was used for the amplification of pTRE-Tight-BI plasmids. To improve the DNA yield of this low copy plasmid the following method was applied: first Stbl3 *E. coli* cells were transformed with 10-20 ng pTRE-Tight-BI plasmid. The next day, selected colonies were inoculated into a 3 mL LB broth containing 100 µg/mL ampicilline and 50 µg/mL streptomycin and incubated overnight at 37°C on 225 rpm shaker. 1 mL from this overnight grown culture was

inoculated into LB broth containing 100 $\mu\text{g}/\text{mL}$ ampicilline and 50 $\mu\text{g}/\text{mL}$ streptomycin and incubated again overnight at 30°C on 225 rpm shaker. 170 $\mu\text{g}/\text{mL}$ chloroamphenicol was added to the cultures to inhibit new protein synthesis, whereas not disturbing plasmid DNA synthesis and incubated again overnight at 30°C on 225 rpm shaker. After the chloroamphenicol treatment the cells were harvested and the plasmids were isolated using Macherey Nagel NucleoPure Plasmid Isolation Kit.

First, RAS/VN173 fragments were ligated into pTRE-Tight-BI vectors. To this end, the plasmids were cut with KpnI/NheI restriction enzymes. Following the restrictions, pTRE-Tight-BI and RAS/VN173 fragments were gel purified. *Stb13* cells were transformed with these ligations. Isolated the plasmids were cut with KpnI/HindIII enzymes to verify the inserts (Figure 3.4).

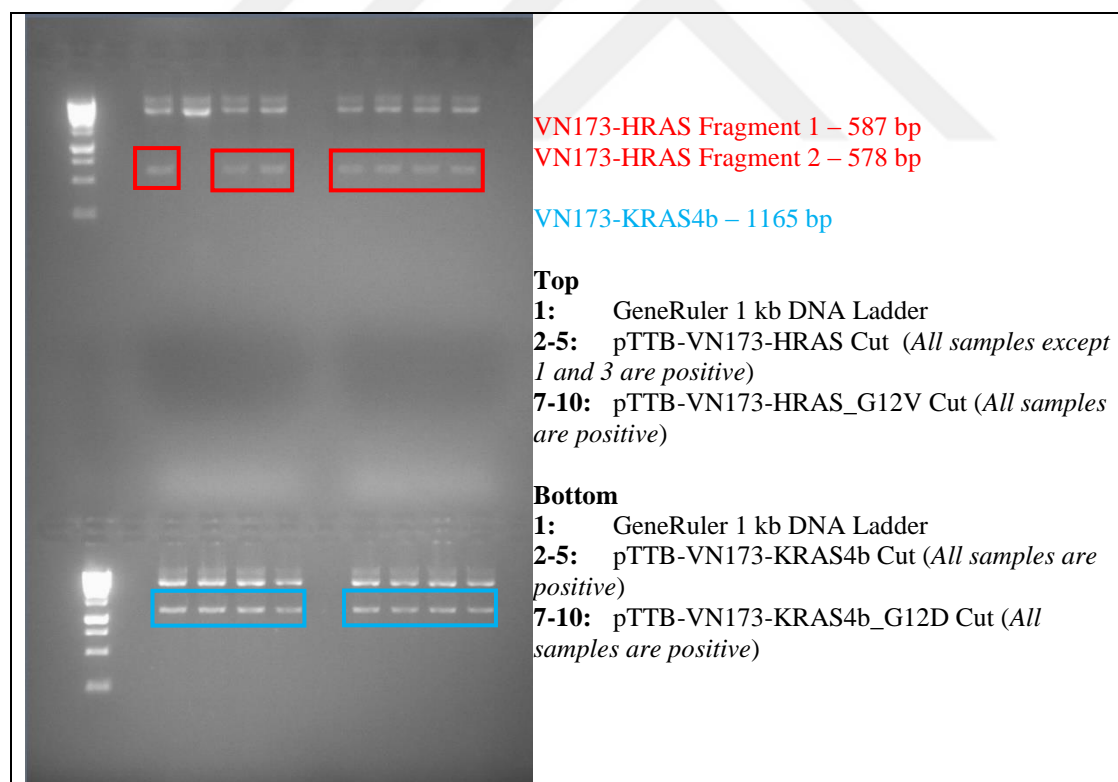


Figure 3.4. Diagnostic digest results for pTTB-VN173-Ras plasmids. There is only one band for VN173-HRAS samples since the cut fragments are similar in size.

Finally, RAS/VC155 fragments were ligated into pTTB-VN173-Ras vectors. pTTB-VN173-HRAS was ligated with VC155-HRAS fragment and pTTB-VN173-HRAS_G12V with VC155-HRAS_G12V fragment using EcoRI/NdeI restriction enzymes. To construct KRAS plasmids pTTB-VN173-KRAS, pJET2.1-VC155, and pJET2.1-KRASb were cut with EcoRI/NdeI, EcoRI/BshTI and BshTI/NdeI restriction enzymes, respectively. Lastly, two samples for each pTTB-BiFC-Ras construct were selected and verified with the diagnostic cut (XhoI/HindIII for pTTB-BiFC-HRAS and XhoI/XbaI for pTTB-BiFC-KRAS4b) (Figure 3.5). The positive samples were sent to sequencing for further verification.

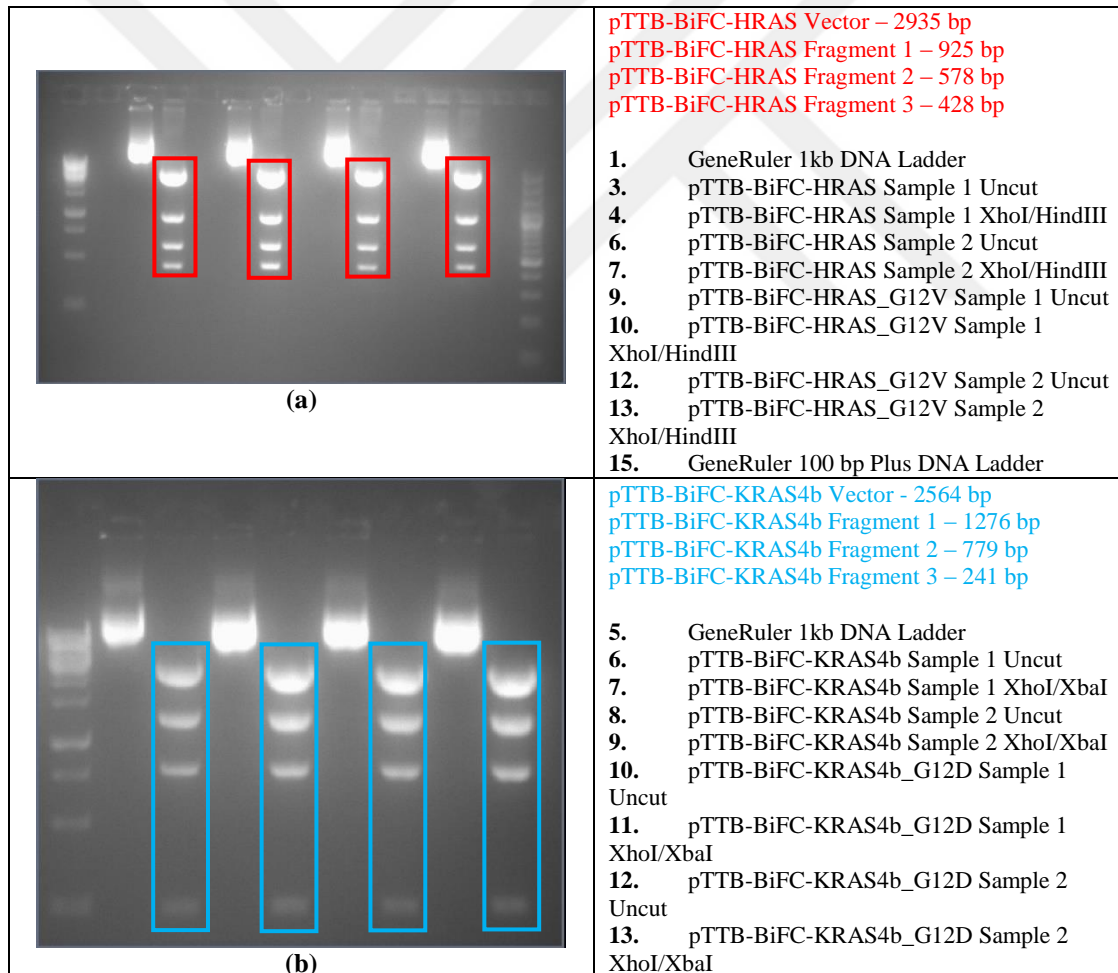


Figure 3.5. Diagnostic cut results for **(a)** pTTB-BiFC-HRAS plasmids and **(b)** pTTB-BiFC-KRAS plasmids.

The constitutively active Ras mutants (H-Ras^{G12V} and K-Ras4B^{G12D}), and the interface mutants (H-Ras^{G12V/K101D/R102E}, H-Ras^{G12V/R41E/K42D}, K-Ras4B^{G12D/K101D/R102E} and K-Ras4B^{G12D/R41E/K42D}) were generated by site-directed mutagenesis and the verified products were ligated to pTRE-Tight-BI vectors in the same way. The oligonucleotide primers for site-directed mutagenesis are listed in Supplemental Tables 3, 4 and 5.

3.2.1.1. Cloning of interface mutants

To confirm the predicted interfaces *in vitro* computationally identified residues (Table 4.1) were mutated following the site-directed mutagenesis protocol described in section 3.2.1. Verified pJET2.1-HRAS, pJET2.1-HRAS_G12V, pJET2.1-KRAS4B and pJET2.1-KRAS4B_G12D plasmids were used as templates for the mutagenesis experiments. The oligonucleotide primers used in the experiment are listed in Tables A.3 and A.4. Gradient PCR was performed and two different annealing temperatures (54°C and 58°C) were used for SDM. We could amplify the mutant genes using at least one of the annealing temperatures (Figures B.5 and B.6). Following the amplification and DpnI digestion, DH5 α cells were transformed with these mutant constructs. Three colonies from each plate were selected and inoculated into ampicillin containing LB broth. Following the overnight incubation the cells were settled and the plasmid were isolated. pJET2.1-Venus-mutant RAS constructs were cut with HindII/PstI to verify the inserts (Figures 3.6 and 3.7).

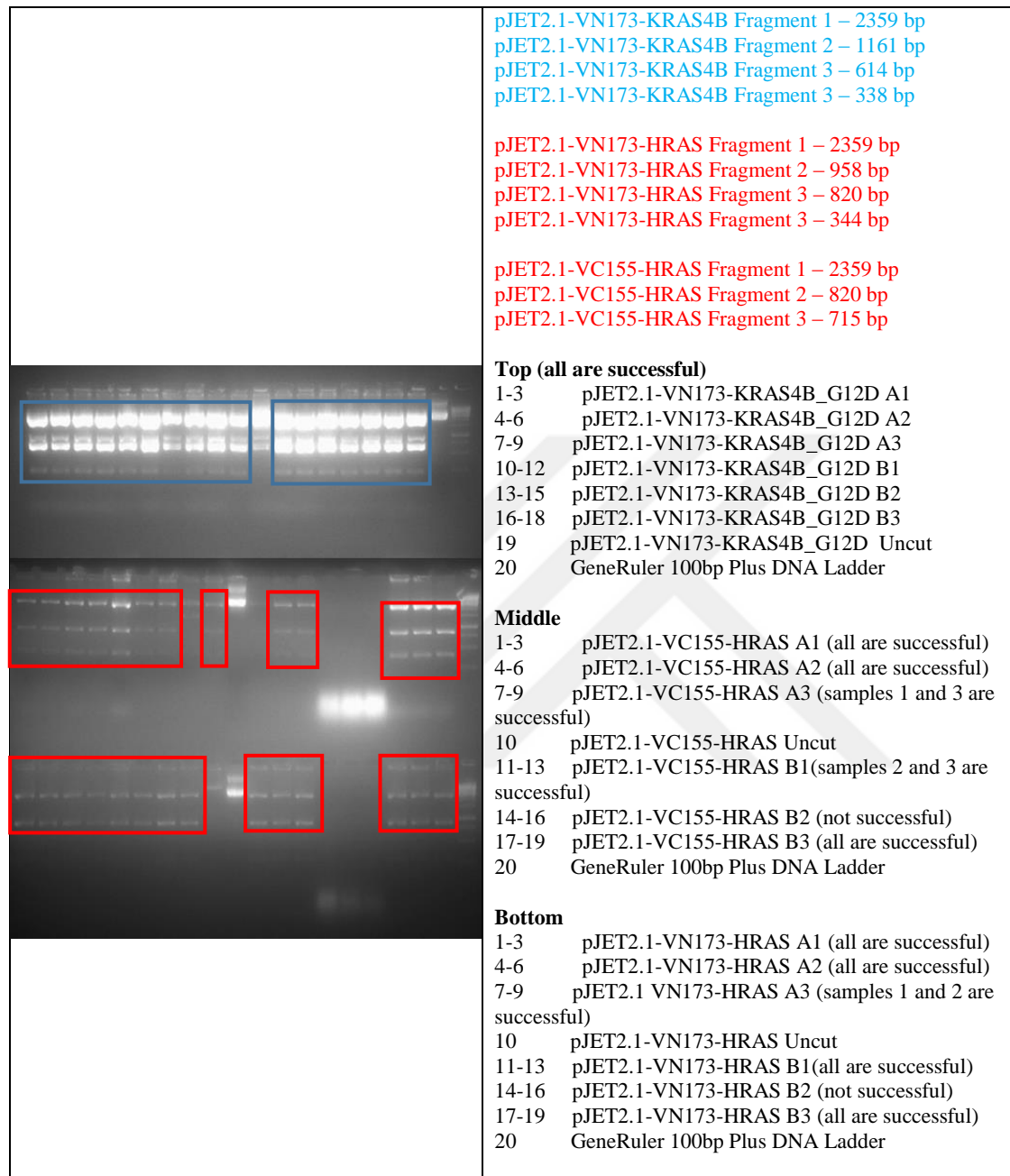


Figure 3.6. Diagnostic digest results of pJET2.1-Venus-RAS and pJET2.1-Venus-HRAS_G12V and pJET2.1-Venus-KRAS4B_G12D interface mutants.

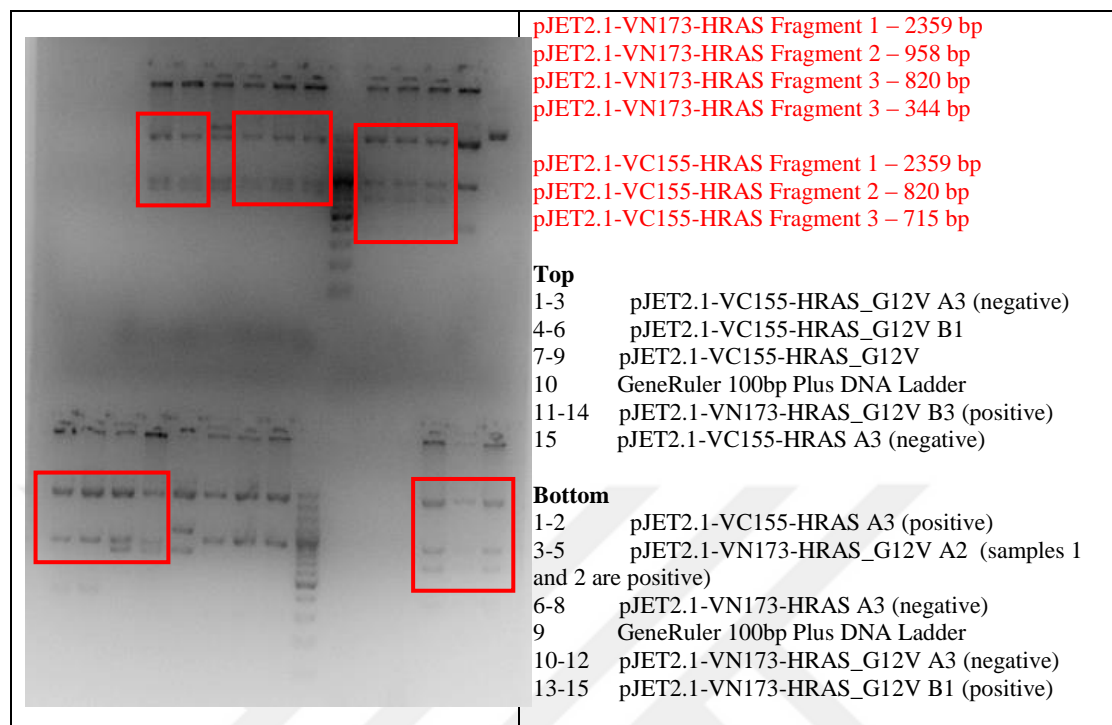


Figure 3.7. Diagnostic digest results of pJET2.1-Venus-HRAS and pJET2.1-Venus-HRAS_G12V interface mutants.

After the diagnostic digest, positive samples were sent to sequencing for further validation. As the results indicated we could obtain all of the interface mutants of K-Ras4B and K-Ras4B^{G12D} and clone these interface mutants into pTTB-Venus vectors. However, we could not obtain B2 (R41A+K42A) and B3 (R41E+K42D) mutants of HRAS(VC155), A1 (E98R) and A2 (K101A+K102A) mutants of HRAS G12V(VN173). Hence, we could clone the A1, A2, A3 and B1 mutants of H-Ras and A3, B1, B2 and B3 mutants of H-Ras^{G12V} into pTTB-Venus vectors.

3.2.2. Transfection of wildtype and oncogenic pTTB-HRAS and pTTB-KRAS4B

The human embryonic kidney cell (HEK 293T) cells were maintained in Dulbecco's Modified Eagle Medium (DMEM, Gibco, Life Technologies, CA, USA) supplemented with 10% tetracycline-free fetal bovine serum (PAN Technologies), 2 mM L-glutamine (Gibco) and 1X Penicillin/Streptomycin (Gibco) at 37°C and 5% (vol/vol) CO₂. HEK 293T cells were plated in 6-well plates (3x10⁵ cells/well), and 24-well plates (0.5x10⁵ cells/well) for western blot and microscopy, respectively, one day before transfection to achieve ~80% confluency. Many lots of bovine sera are contaminated

with tetracycline (Tc) or Tc-derivatives which can affect basal expression or inducibility in Tet-system plasmids. It is critical that the FBS used for cell culture does not interfere with Tet-responsive expression. Thus, tetracycline-free FBS was used. The next day, HEK293T cells were co-transfected with pTTB-RAS and pFUW-M2rtTA (a lentiviral plasmid expressing the reverse tetracycline transactivator, rtTA), using polyethyleneimine (PEI) along with Opti-MEM (Gibco). Total plasmid concentration was kept at 2 $\mu\text{g}/\text{well}$ for the 6-well transfection. Approximately 10 h after transfection, the culture media was changed and Ras expression was induced by 1 ng/mL Doxycycline (Dox). The cells were continuously exposed to Dox for 6, 12 and 24 h before final assays with imaging or Western blotting.

3.2.3. Visualizing the cells by fluorescence microscopy

Transfected HEK293T cells were captured 6, 12 and 24 h after Dox-induction using a Zeiss Axio Observerlight microscope with a EC Plan-Neofluar 20x objective with numerical aperture of 0.5 using AxioCam 702 Monochromatic camera. Microscopic images are recorded with ZEN Studio software. The final resolution of the recorded images was 0.55 $\mu\text{m}/\text{pixel}$. The detection channel for fluorescence was 465nm LED for eGFP (exc: 449-473 nm, em: 470 \pm 40 nm).

3.2.4. Immunofluorescence, Microscopy and Quantification

For immunofluorescence experiments, cells were grown on coverslips and fixed in 4% paraformaldehyde in PBS for 15 min at room temperature. After rehydration in PBS, cells were blocked in 3% BSA (Sigma-Aldrich) in PBS + 0.1% Triton X-100. Coverslips were incubated in primary antibodies diluted in blocking solution, and Alexa Fluor 488, 594-, or 680-conjugated secondary antibodies were diluted in 1:500 in blocking solution (Invitrogen). Rabbit anti-HLA(Santa Cruz Biotechnology) antibody was used for marking the plasma membrane. Samples were mounted using Mowiol. Coverslips of cells were imaged using LAS X software (Premium; Leica) on a scanning confocal microscope (SP8; Leica Microsystems) with Plan Apofluar 63X 1.4 NA objective and by DMi8 inverted microscopy using a cooled charge-coupled device camera (Orca ER, Hamamatsu Photonics; Cascade EM-CCD, Photometrics).

BiFC efficiency was calculated by quantifying the fluorescence intensity ratio of Venus to the internal control Scarlet. Quantitative immunofluorescence for GFP and Scarlet intensities was performed by acquiring a z-stack of cells using identical gain and exposure settings. The z-stacks were used to assemble maximum-intensity projections. Cells were defined by HLA staining and their fluorescence pixel intensity were measured. Quantifications and image processing were performed using ImageJ (National Institutes of Health, Bethesda, MD). Background was quantified by measuring fluorescence intensity of a region of equal dimensions in the area neighboring the cells. Quantification was based on two independent experiments.

Quantification of membrane and cytoplasmic localization of Venus signals were based on analysis of stacks and co-localization of signal with the membrane marker HLA and the cytoplasmic/nuclear marker Scarlet. Cells where Venus co-localizes with HLA were counted as membrane-positive, cells where Venus co-localizes with Scarlet were counted as cytoplasm-positive and cells where Venus co-localizes with both Scarlet and HLA were counted as membrane and cytoplasm-positive. Quantification was based on two independent experiments.

3.2.5. Determination of the Ras expression and pERK, pAKT levels by western blotting

Transfected HEK 293T cells were collected after 3, 6, 12 and 24 h Dox-induction with scraper and stored at -20°C until to be used. Frozen cells were lysed with a mixture of RIPA cell lysis buffer, phosphatase and protease inhibitors. Collected cell lysates were incubated on ice for 30 min and then sonicated 2 times for 5 seconds each. The lysates were then centrifuged at $14,000 \times g$ and 4 °C for 30 min. Supernatants were mixed with a 4× SDS-PAGE sample buffer (200 mM Tris-Cl, pH 6.8, 8% SDS, 4% β-mercaptoethanol, 0.02% bromophenol blue, 40% glycerol). The mixture was then heated at 95 °C for 5 min. After cooling down to room temperature, samples were loaded into a 12% SDS-polyacrylamide gel and run at 100 V for 90 min at room temperature. Protein transfer was performed on a wet-transfer system at 100 V for 60 min with water cooling, using a PVDF membrane (Immobilon-P, Millipore Corp.). Blots were blocked with 5 % w/v powdered nonfat milk in tris-buffered saline with 0.1 % Tween-20 (TBS-

T) for 1 h. They were incubated with primary antibodies overnight at 4 °C, washed, followed by incubation with secondary antibodies for 1h at room temperature for imaging with ChemiDoc™ Imaging system (BIO-RAD). Antibodies used for Western blotting in this study are: Myc (Rabbit monoclonal, Cell Signaling Technology no. 2278), FLAG (Rabbit monoclonal, Cell Signaling Technology no. 14793), ERK (Rabbit monoclonal, Cell Signaling Technology no. 4695), ppERK (Rabbit monoclonal, Cell Signaling Technology no. 4370), Akt (Rabbit monoclonal, Cell Signaling Technology no. 4691), pAkt (Rabbit monoclonal, Cell Signaling Technology no. 4060), Histone H3 (Rabbit monoclonal, Cell Signaling Technology no. 4499), Vinculin (Rabbit monoclonal, Cell Signaling Technology no. 4650), and Anti-rabbit IgG (Cell Signaling Technology no. 7074).

3.2.6. Real-time PCR

Total RNA was extracted with Direct-zol™ RNA Kit (Zymo Research). 500 ng of total RNA was used for first strand cDNA synthesis in a mixture containing RevertAid Reverse Transcriptase, oligo-dT, RiboLock RNase inhibitor and dNTPs (10mM). Subsequently, JUN, FOS, and EGR1 cDNAs were subjected to a SYBR green-based method for real-time polymerase chain reaction (PCR) relative quantification. The real-time PCR primers were as follows: for human JUN, forward, 5'-TTCTATGACGATGCCCTCAACGC-3' and reverse, 5'-GCTCTGTTTCAGGATCTTGGGGTTAC-3'; for FOS, forward, 5'-GCATCTGCAGCGAGCATCTGAGAA-3' and reverse, 5'-AGAGCTGGGTAGGAGCACGGTCACT-3'; for human EGR1, forward, 5'-CTTCAACCCTCAGGCGGACA-3' and reverse, 5'-GGAAAAGCGGCCAGTATAGGT-3'. JUNB, FOS and EGR-1 expression levels were calculated relative to the level of the glyceraldehyde-3-phosphate dehydrogenase (GAPDH) housekeeping gene.

3.2.7. Statistical analysis

Statistical significance and p values were assessed by one-way analysis of variance and Student's t tests using Prism software (GraphPad Software, La Jolla, CA). Error bars

reflect SEM. Following key is followed for asterisk placeholders for p-values in the figures: *** $p < 0.001$, ** $p < 0.01$, * $p < 0.05$.

3.3. Computational Prediction of Ras-Effector Interactions

Crystal structures of the H-Ras with Raf-1, PI3K γ , RalGDS, PLC ϵ , Bry22, and RASSF5 are available in PDB (Table A.5). Using PRISM all of the other effector binding regions on Ras were predicted. The structural data for the target proteins were obtained from the PDB. Some effectors (RASSF1, RAIN, RGS12, RGL1, AFAD, RIN1) do not have a tertiary structure in PDB. The 3D models of these proteins were built using I-TASSER [191]. Then, the complex structures of the binding partners with H- and K-Ras4B proteins were predicted.

3.4. Computational prediction of the structure of K-Ras4B with CaM and PI3K

To model the interactions between K-Ras, calmodulin and PI3K p85 regulatory subunit, I used PRISM [183-185]. Here, the structural data was obtained from the PDB. The G-domain of K-Ras (166 residues), full length CaM (149 residues) and the p85 regulatory subunit of PI3K were used as target proteins. K-Ras catalytic domain has 27 structures in the PDB. They include GDP- and GTP-bound conformations. The GTP-loaded active K-Ras molecules were used in the predictions. Full length CaM has about 75 structures in the PDB. Only X-ray structures with $< 3.00 \text{ \AA}$ resolution were considered. In this way, the number of CaM structures was reduced to 43 with 71 chains in total. There are five variants of the p85 regulatory subunit, designated p85 α , p55 α , p50 α , p85 β , and p55 γ . p85 α structures were used. p85 α contains a Rho-GAP domain, 2 SH2 domains (nSH2 and cSH2) and a SH3 domain. The interaction between CaM and the 2 SH2 domains was investigated. I predicted models for the binary interactions between K-Ras and PI3K, and CaM and PI3K. The contact regions were identified using HotRegion [188]. The models based were built based on the binary interactions and available literature data.

3.5. MD Simulations of the K-Ras4B/PDE δ and HVR/PDE δ Complexes

3.5.1. Generating initial configurations

The simulation inputs were built using CHARMM [192] c39b2 with the CHARMM 36 force field [193]. Bonded parameters for the GTP and the prenylated and methylated cysteine were adopted from previous works.[194-197] Farnesylated and geranylgeranylated K-Ras4B-GTP proteins were constructed using the crystal structures (PDB ID: 3GFT and 4DSO) as described earlier.[194, 196, 198] The former is GNP-bound K-Ras4B₁₋₁₆₇ with Q61H mutation, and the latter is GSP-bound K-Ras4B₁₋₁₈₀ with G12D mutation. Both GTP analogs were converted to GTP, and their sequences were modified into human. The missing HVR coordinates, HVR₁₆₈₋₁₈₅ for the former and HVR₁₈₁₋₁₈₅ for the latter were modeled as a flexible loop. At the C-terminus, Cys185 was modified with the farnesyl/geranylgeranyl and methyl groups. Thus, we obtained two K-Ras4B-GTP models denoted KM1 and KM2. The HVR of KM1 is a flexible chain, while the HVR of KM2 partially folds into an α -helix extending from α 5 of the catalytic domain (Figure 1A). To model the interactions of PDE δ with farnesyl and geranylgeranyl moieties, two crystal structures were used (PDB ID: 5F2U and 5E8F). The former PDE δ crystal structure contained the farnesyl group in the hydrophobic cavity, and the latter involved the geranylgeranyl group in the cavity. Due to the relatively longer geranylgeranyl moiety, the latter PDE δ has a deeper hydrophobic cavity resulting from the Phe133 aromatic ring flipped downward. In contrast, the former PDE δ embedding the farnesyl has a shallower cavity resulting from the Phe133 aromatic ring flipped upward. Depending on the orientations of the Phe133 sidechain, we designated PDE δ into two different states; state 1 is for the downward sidechain, and state 2 is for the upward sidechain (Figure 1B). In the initial model construction, with farnesylated K-Ras4B-GTP, we took these two PDE δ states. For state 1, the originally embedded geranylgeranyl group was replaced with the farnesyl group. As a result, a couple of HVR backbone residues slipped into the cavity. For geranylgeranylated K-Ras4B-GTP, only state 1 of PDE δ was modeled. The combinations of two K-Ras4B models, KM1 and KM2, and PDE δ in states 1 and 2, obtained six model systems; four with farnesylated and two with geranylgeranylated K-Ras4B-GTP (Table 1). For

comparison, we also simulated another six PDE δ systems containing the HVR peptide only, without the catalytic domain. The HVR peptides of three Ras isoforms, K-Ras4A, K-Ras4B, and N-Ras, were modeled with PDE δ in states 1 and 2. Two modeled systems for each Ras isoform's HVR with PDE δ in states 1 and 2 are designated: System A1 and System A2 for K-Ras4A, System B1 and System B2 for K-Ras4B, and System N1 and System N2 for N-Ras (Table 2). In the HVR/PDE δ complex, the HVR peptides of both K-Ras4A and N-Ras were modified with a depalmitoylation, but with a farnesyl modification as the HVR peptide of K-Ras4B.

3.5.2. Atomistic MD simulations

The crystal structures of PDE δ provided a short peptide with 4-5 residues along with the prenyl group at the gate of the hydrophobic pocket. The sequence of the prenylated peptide was converted to that of the anchor portion of the HVR at the C-terminal region of K-Ras4B. In the initial construction towards the starting point, the backbone of the peptide and the prenyl group were kept intact during the preequilibration cycles. The rest of the HVR backbone was modeled as a flexible loop and then covalently connected to both the catalytic domains using the crystal structures and the HVR anchor portions converted from the crystal peptides. To align the two proteins well with each other, the K-Ras4B-GTP/PDE δ systems were minimized with a rigid body motion for the K-Ras4B catalytic domain and PDE δ in order to enhance the interaction between them. A number of rigid body minimization steps were performed for the systems with the modeled HVR portion the only held unrestrained. The CHARMM36 [192] program was used to construct six initial configurations of the K-Ras4B-GTP/PDE δ system (Figure S1 of the Supporting information). A total of 13 MD simulations including three K-Ras4B-HVR/PDE δ , two K-Ras4A-HVR/PDE δ , and two N-Ras-HVR/PDE δ) were performed in a water environment. The initial K-Ras4B-GTP/PDE δ and HVR/PDE δ configurations were solvated by the modified TIP3P water model [199] and gradually relaxed with the proteins held rigid. For both the farnesylated and geranylgeranylated K-Ras4B-GTP/PDE δ systems the unit cell box of 100 \AA^3 contains around 102,000 atoms with ions, 31 Na^+ , 1 Mg^{2+} , and 30 Cl^- , to satisfy a total cation concentration near 100 mM. For the farnesylated HVR/PDE δ systems the unit cell box of 80 \AA^3 contains around

51,900 atoms with ions, 20 Na⁺, and 20 Cl⁻, for systems with N-Ras, 20 Na⁺, and 25 Cl⁻ for systems with K-Ras4A, and 20 Na⁺, and 28 Cl⁻ for systems with K-Ras4B. In the dynamics, long range electrostatic interactions were calculated by using the particle mesh Ewald (PME) method. The Langevin temperature control was used to maintain the constant temperature at 310 K, and Nosé-Hoover Langevin piston pressure control was used to maintain the pressure at 1 atm. A total of 1.8 μs simulation were performed for the six K-Ras4B-GTP/PDEδ systems; each has 300 ns simulation with the constant temperature at 310 K. The HVR/PDEδ systems were simulated for 200 ns. All simulations were performed in the NPT (constant number of atoms, pressure, and temperature) ensemble. The NAMD 2.10 [200] parallel computing code was employed in the production runs on a Biowulf cluster at the National Institute of Health.

3.5.3. MM/GBSA calculations

To compare the interaction strengths of the systems, binding energy calculations have been performed. To this end, the sum of gas-phase energies (including coulombic energy, van der Waals energy as determined by a Lennard–Jones potential and internal energy), and solvation free energies (including a non-polar part and an electrostatic part obtained from generalized Born (GB) calculations) were calculated using the molecular mechanics energies combined with the GB and surface area continuum solvation (MM/GBSA) method. The gas-phase and solvation free energy values were averaged over 3000 snapshots taken at 100 ps intervals from the 300 ns of MD simulations of K-Ras4B-GTP/PDEδ and 2000 snapshots taken at 100 ps intervals from the 200 ns of MD simulations of HVR/PDEδ systems. The calculations were performed with Amber v14 software using a modified GB model developed by Onufriev *et al.*[201] To this end, the NAMD PSF and coordinate files were converted into Amber format using the chamber program in Amber.[202] The change in binding energy due to the dimerization is calculated by using the equation

$$\Delta G_b = G_b^{system} - (G_b^{K-Ras4B} + G_b^{PDE\delta}). \quad (1)$$

The binding energy was calculated as a sum of the gas phase contribution and the solvation energy contribution $\langle \Delta G_b \rangle = \langle \Delta G_{gas} \rangle + \langle \Delta G_{sol} \rangle$, where $\langle \rangle$ denotes an average along the MD trajectory.



Chapter 4

H-Ras and K-Ras4B HOMODIMERS

4.1. Computational Prediction of the Structures of H-Ras and K-Ras4B Dimers

Modeling results suggested that in both GTP- and GDP-bound states, K-Ras4B₁₋₁₈₀ can form homodimers through the same interface (Figures 4.1 and 4.2). The binding energy score (BES) for the predictions is lower than -10. On the basis of our previous studies [185, 203-205], we set the energy score cutoff value as -10. Thus, predictions with BESs lower than -10 are considered as favorable interactions. In both cases, the interface regions include $\alpha 1$, $\beta 2$, and $\beta 3$. However, the K-Ras4B-GTP homodimer is more stable than its GDP counterpart [206]. The enhanced stability is associated with a larger interface and more hot spots in the GTP-bound homodimer and thus greater favored binding energy score (BES) (Figure 4.1). Analysis of atomic interactions showed that the Ras-GTP homodimer interface contains more H-bonds than the GDP-bound. To corroborate the predicted interface, all possible crystal dimer interfaces of Ras structures were reconstructed using the Evolutionary Protein-Protein Interface Classifier (EPPIC) [189] Server. The crystal interface of the Ras dimer showed remarkable similarity to my predicted K-Ras4B-GTP homodimer and even H-Ras-GTP dimer interfaces (Figure 4.3). The first predicted dimer interface involves a β -sheet extension, forming intermolecular H-bonds between $\beta 2$ strands (hereafter referred as β -Homodimer). Computations also predict a second dimer interface, involving an α -helical interface in the $\alpha 3$ and $\alpha 4$ regions at the C-terminal allosteric lobe of the G-domain (hereafter referred as α -Homodimer) (Figures 4.1 and 4.2). I further predicted that GTP-bound Ras can bind GDP-bound Ras through different interface regions with differing stabilities (Figure 4.4); however, the most favorable interface (Heterodimer 1) remarkably overlaps with the major one predicted for the GTP- and GDP-bound homodimers, involving a β -sheet extension. The results point to these interfaces taking place between the catalytic domains in the farnesylated HVR-anchored HVR state.

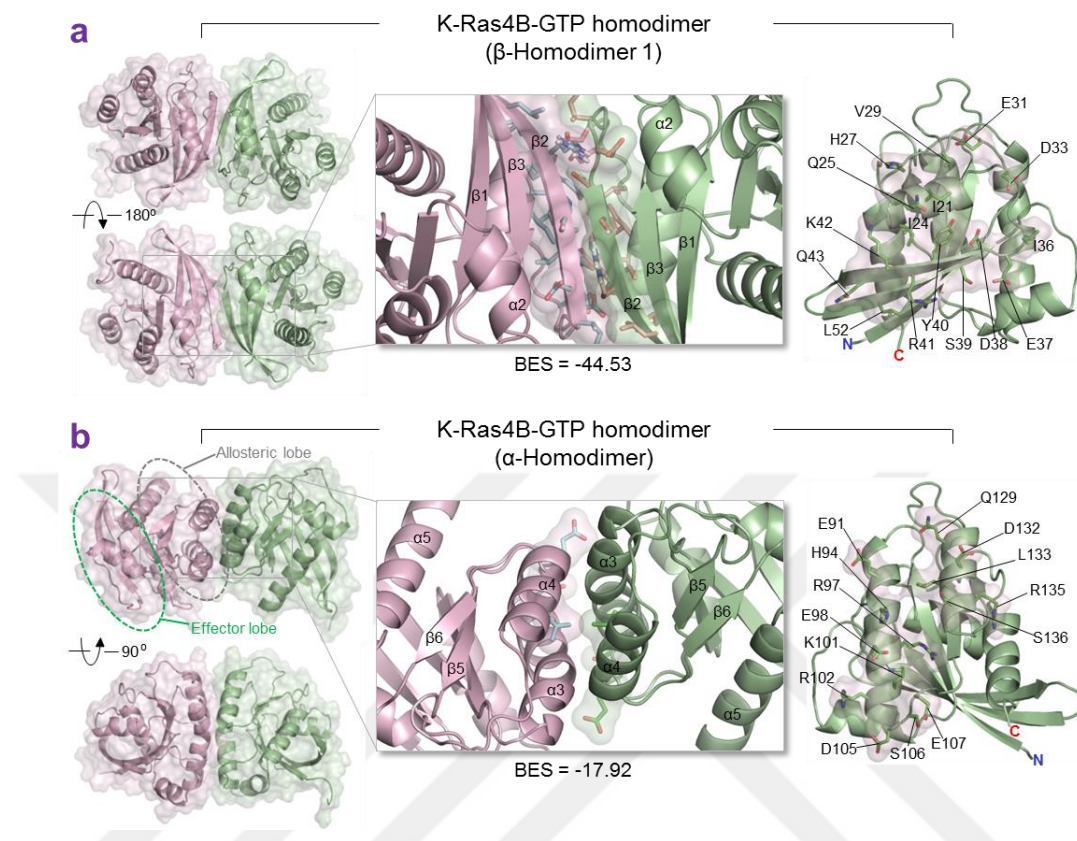


Figure 4.1. Predicted homodimer structure of active Ras isomer. (a) Predicted homodimer structure of GTP-bound K-Ras4B₁₋₁₈₀ with a β -sheet extension (β -Homodimer 1; PDB code: 4DSO). Binding energy score (BES) for the prediction is -44.53 (Template interface: 2erxAB). Interface residues are I21, I24, Q25, H27, V29, E31, D33, I36, E37, D38, S39, Y40, R41, K42, Q43, and L52. (b) Predicted homodimer structure of GTP-bound K-Ras4B₁₋₁₆₇ with an α -helical interface (α -Homodimer; PDB code: 3GFT). Dimer interface is found to be at the allosteric lobe with binding energy score (BES) of -17.92 (Template interface: 4a9eAB). Interface residues are E91, H94, R97, E98, K101, R102, D105, S106, E107, Q129, D132, L133, R135, and S136.

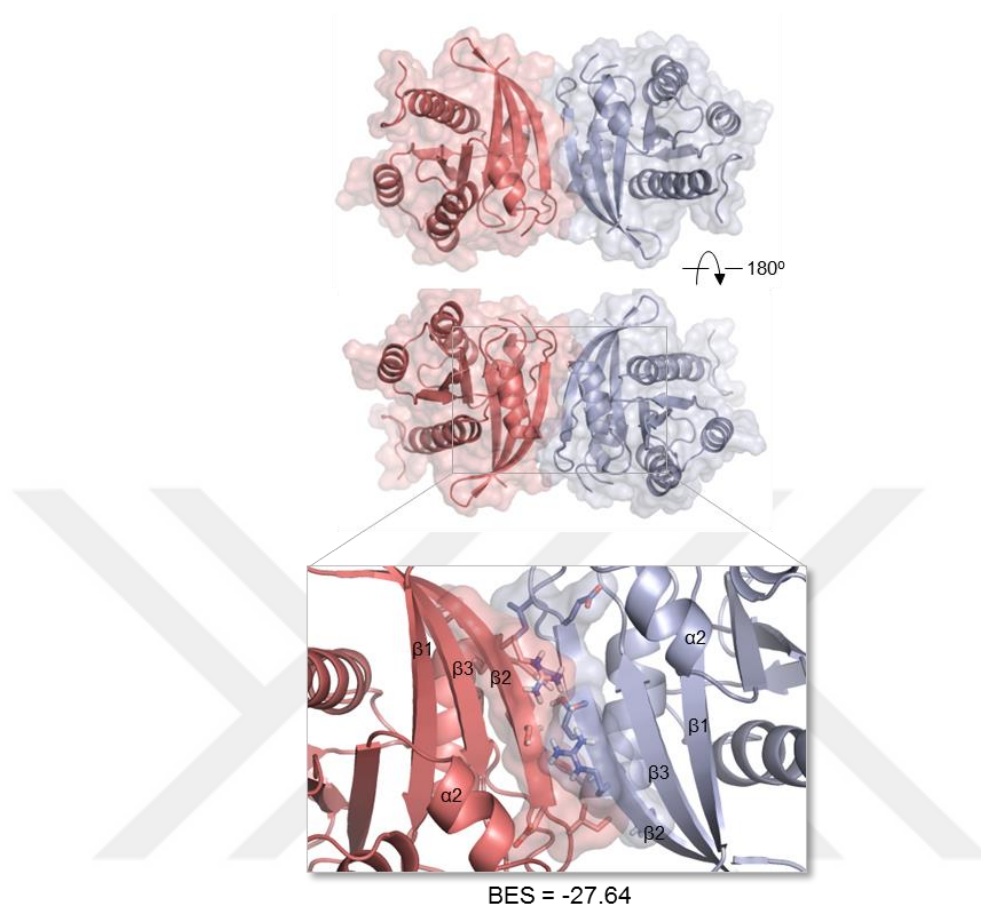


Figure 4.2. Predicted homodimer structure of inactive Ras isomers. Predicted homodimer structure of GDP-bound K-Ras4B₁₋₁₈₀ (PDB code: 4DSU) with BES = -27.64 (Template interface: 2erxAB). Dimer interface with the β -sheet formation is shown in the rectangular panel. Interface residues are I24, Q25, I36, E37, D38, S39, Y40, R41, and K42.

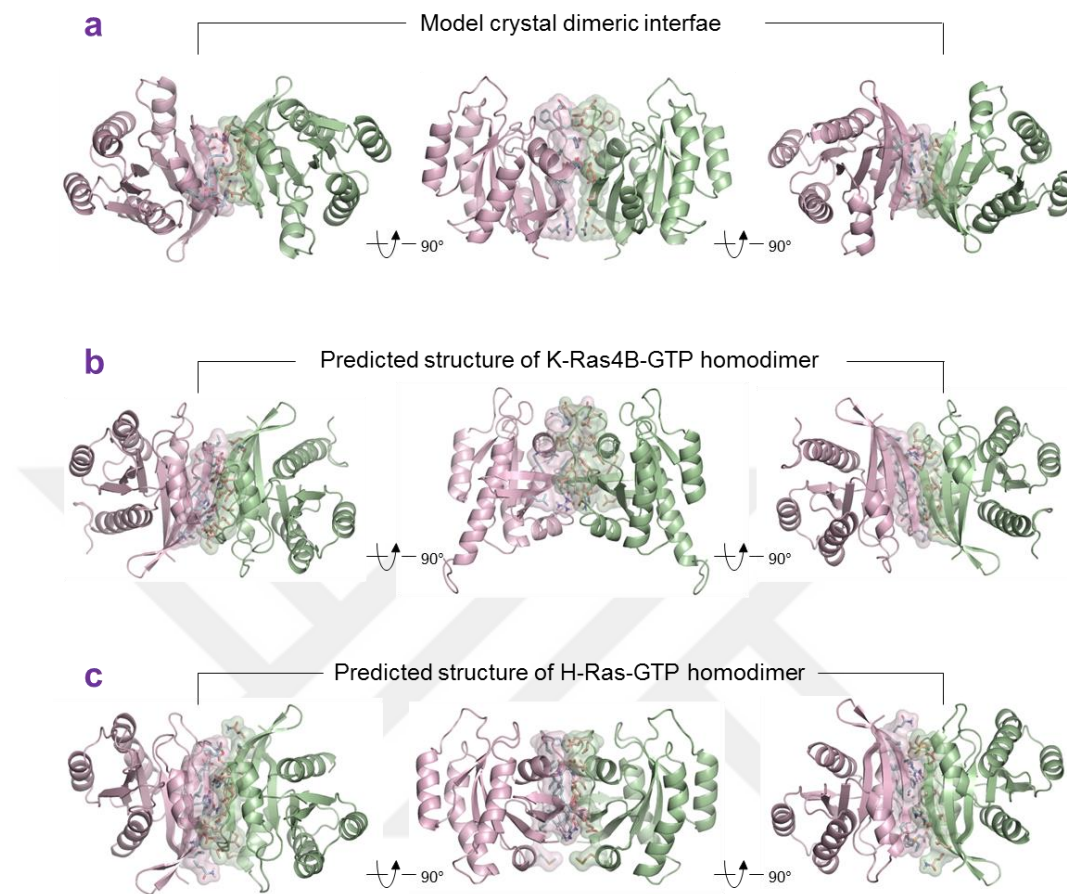


Figure 4.3. Crystal and predicted structures of Ras dimers. (a) Crystal interfaces projected on the GTP-bound Ras homodimer (H-Ras-GTP was used as an example, PDB code: 1LF0). Interface residues are I21, I24, Q25, H27, F28, V29, D30, E31, D33, D38, S39, Y40, R41, and L52. (b) Predicted homodimer structure of GTP-bound K-Ras4B (PDB code: 4DSO). The dimer structure is β -Homodimer 1 in Fig. 3a. (c) Predicted homodimer structure of GTP-bound H-Ras (PDB code: 1LF0). Binding energy score (BES) for the prediction is -44.53, the same as the K-Ras4B-GTP β -Homodimer 1. Interface residues are I21, I24, Q25, H27, V29, E31, D33, I36, E37, D38, S39, Y40, R41, K42, Q43, L52, and M67.

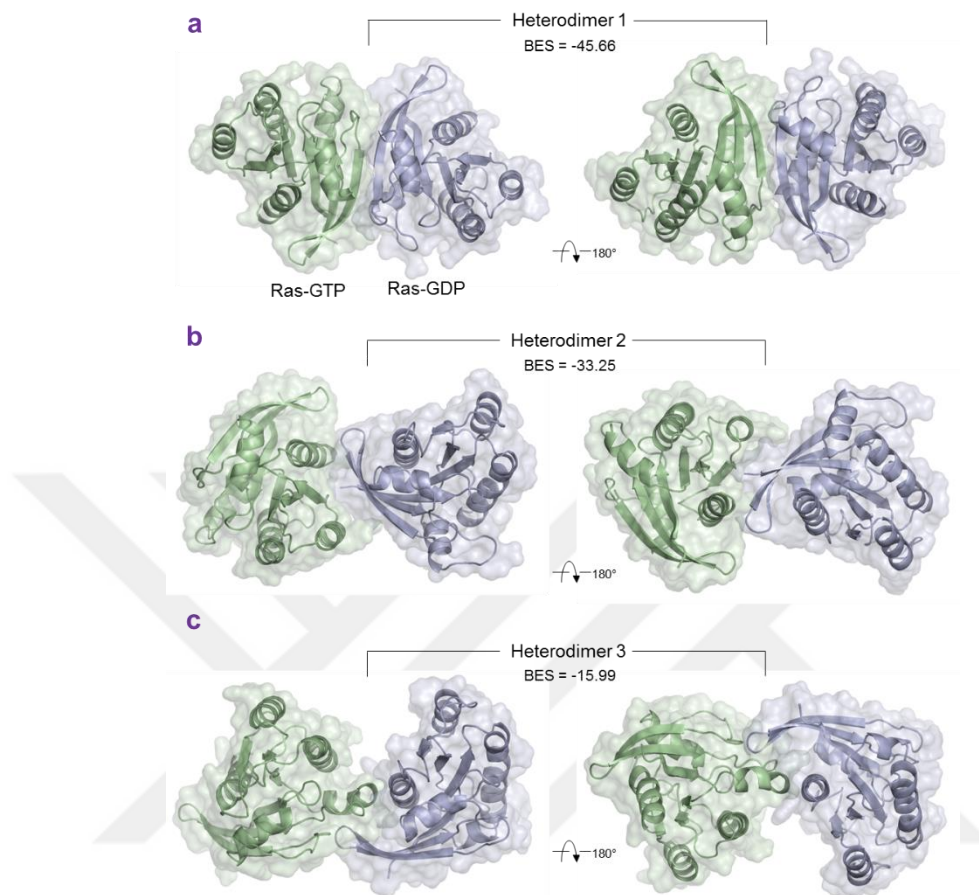


Figure 4.4. Predicted structures of Ras heterodimers. (a) The 1st predicted heterodimer structure of H-Ras (Heterodimer 1) in the GTP-bound (PDB code: 1QRA, green) and GDP-bound (PDB code: 1IOZ, blue) states with binding energy score (BES) of -45.66 (Template interface: 2erxAB). Interface residues for the Ras-GTP are I21, I24, Q25, D33, I36, E37, D38, S39, Y40, R41, K42, Q43, L52, Y64, and M67. For the Ras-GDP, they are I24, Q25, Y32, D33, I36, E37, D38, S39, Y40, R41, K42, Q43, and L52. (b) The 2nd predicted heterodimer structure of H-Ras (Heterodimer 2) in the GTP-bound (PDB code: 1GNR, green) and GDP-bound (PDB code: 4Q21, blue) states with BES = -33.25 (Template interface: 6q21AB). Interface residues for the Ras-GTP are M1, E3, R41, Q43, V45, G48, E49, and T50. For the Ras-GDP, they are R128, D132, R135, G138, I139, P140, Y141, I142, T158, R161, E162, and Q165. (c) The 3rd predicted heterodimer structure of H-Ras (Heterodimer 3) in the GTP-bound (PDB code: 1QRA, green) and GDP-bound (PDB code: 1IOZ, blue) states with BES = -15.99 (Template interface: 1gylAB). Interface residues for the Ras-GTP are I36, E37, E62, E63, Y64,

A66, M67, R68, D69, Q70, and Y71. For the Ras-GDP, they K42, V44, V45, I46, D47, G48, E49, L53, E153, Y157, T158, V160, and R161.

These results are significant since they not only validate the ability of Ras catalytic domain to form dimers and present the possibility of Ras nanocluster formation through the two dimer interfaces, (Figure 4.5), but also suggest that dimer formation, in particular, provide a previously unknown mechanism for how Ras dimerization may regulate signaling outputs and Raf dimerization. We observe that the binding surfaces and interaction modes of Raf (Figure 4.6 a, b) overlap Ras's β -sheet dimer interface. Thus, Raf's dimerization can be facilitated when Ras dimerizes through the second helical interface (Fig. 4.6 c). Taken together, these results argue that therapeutically abolishing the major β -sheet mediated dimerization may not deter Raf's activation; however, targeting the helical interface exploiting state-of-the-art techniques, orthosteric or allosteric [207-210] may prove an effective therapeutic intervention.

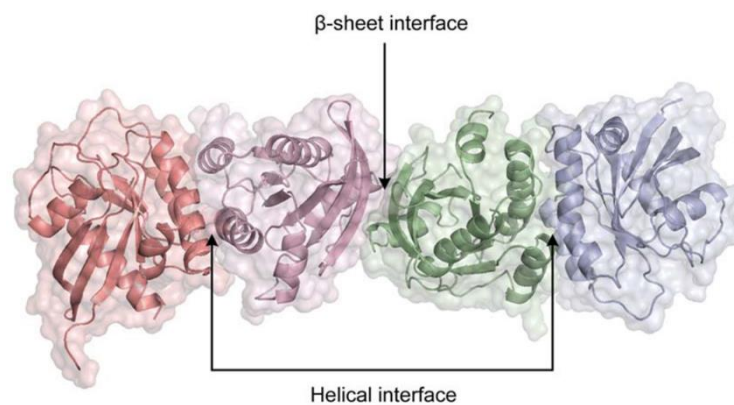


Figure 4.5. Predicted tetramer structure of active K-Ras4B (PDB ID: 3GFT) [48]. Active Ras can form tetramers or higher-order oligomers using β -sheet extension and helical interfaces. It can dimerize through the β -sheet extension and tetramerize through the helical interface, or *vice versa*.

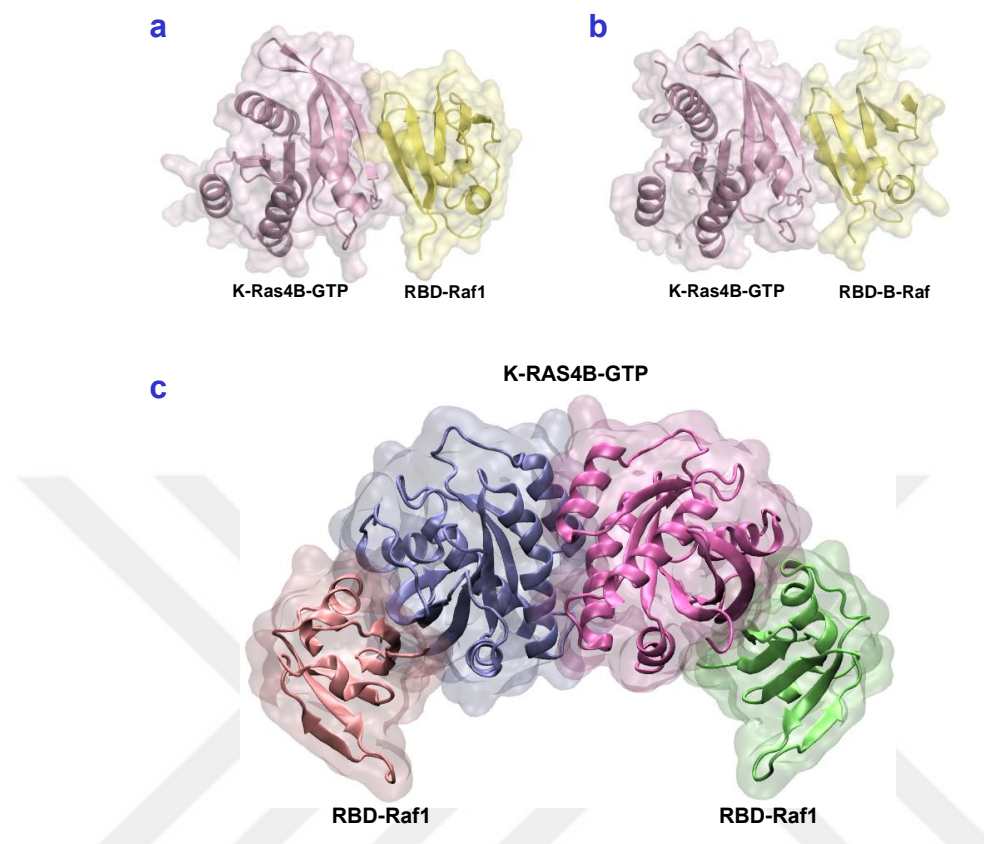


Figure 4.6. Ras-effector binding and tetramerization. Predicted dimer structures of the GTP-bound K-Ras4B with (a) Ras-binding-domain (RBD) of Raf1 (Target PDB code: 1C1Y, Template interface: 1c1yAB) and (b) RBD-B-Raf (Target PDB code: 3NY5, Template interface: 1c1yAB). (c) Predicted tetramer structures of the GTP-bound K-Ras4B dimers with Ras-binding-domain (RBD) of Raf1 (Target PDB code: 1C1Y, Template interface: 1c1yAB).

4.2. Determination of the Residues to Be Mutated

Predictions reveal that Ras-Ras β -homodimer and the majority of the Ras-effector interactions share coinciding or overlapping interfaces. Thus, a mutation on these interfaces might affect both associations. Nevertheless, the two interfaces (α - and β -homodimers) were considered while determining the residues to be mutated experimentally to confirm our predicted dimer interfaces and investigate the effects of different mutations on Ras dimerization and signaling.

Ras dimer interfaces were evaluated by our collaborators using explicit MD simulations on both GTP-bound K-Ras4B and H-Ras dimers at the anionic lipid bilayer (Figures 4.7 and 4.8) and in solution and observed that the stability of the Ras dimers is isoform-specific, controlled by their distinct HVRs [197]. Atomic interactions in the GTP-bound H-Ras and K-Ras4B homodimers were analyzed at the membrane to narrow down the number of the residues to be mutated. Then, FoldX [190] was used to compute the change in binding free energy ($\Delta\Delta G$) upon mutation. Tables A.7 and A.8 show the residues tested and the corresponding $\Delta\Delta G$ values upon mutations.

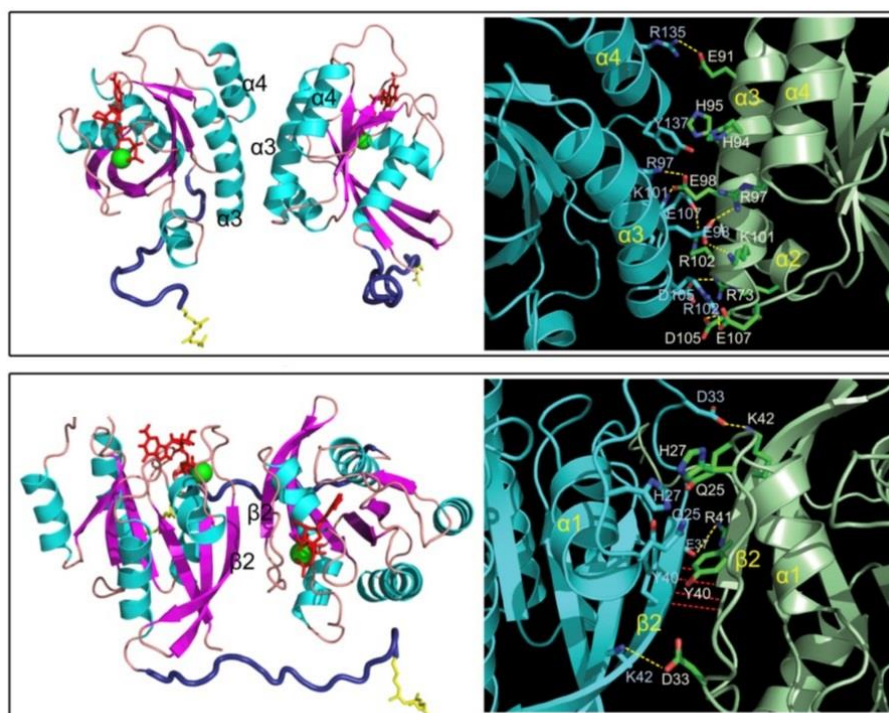


Figure 4.7. Relaxed K-Ras4B dimers at the membrane. Snapshots representing average conformations of GTP-bound K-Ras4B with the post-translational modifications (PTMs) on the anionic lipid bilayer composed of DOPC:DOPS (mole ratio 4:1). The K-Ras4B-GTP dimers with different dimer interfaces are shown (left column). Lipids and water are removed for clarity. In the catalytic domain, the red sticks and green spheres represent GTP and Mg^{2+} ions, respectively. The HVR in the tube representation is colored deep blue, and the farnesyl as a stick is colored yellow. Highlighted dimer interfaces are shown (right column). In the highlight, yellow dotted

lines denote salt bridges and red dotted line indicate the intermolecular backbone hydrogen bonds (H-bonds). Residues involving the hydrophilic and hydrophobic interactions are also marked [197].

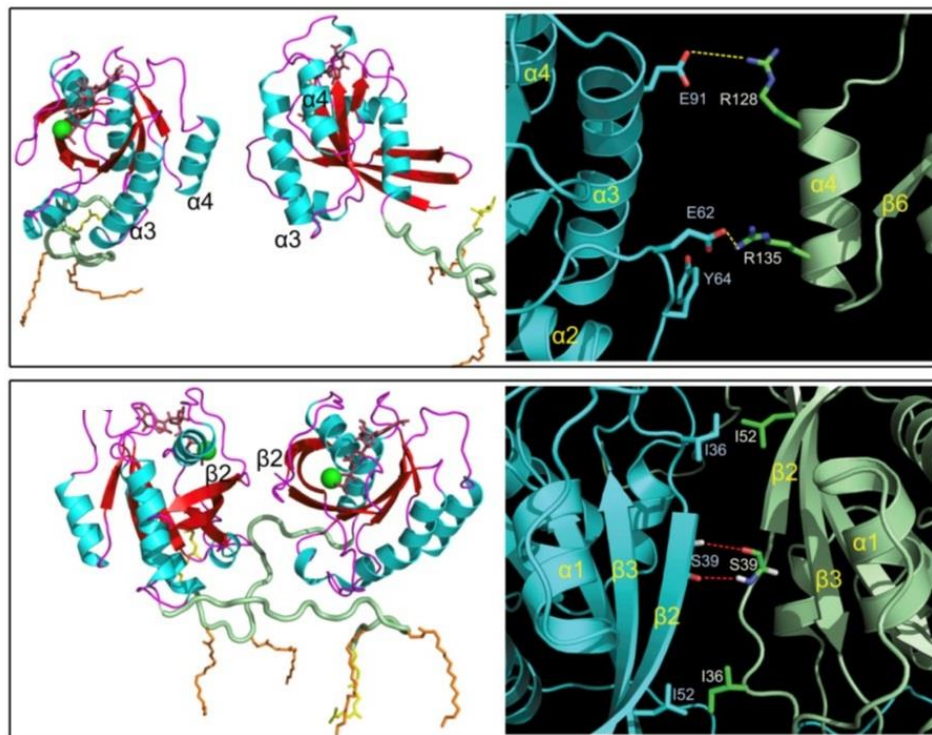


Figure 4.8. Relaxed H-Ras dimers at the membrane. Snapshots representing average conformations of GTP-bound H-Ras with the post-translational modifications (PTMs) on the anionic lipid bilayer composed of DOPC:DOPS (mole ratio 4:1). The H-Ras-GTP dimers with different dimer interfaces are shown (left column). Lipids and water are removed for clarity. In the catalytic domain, the red sticks and green spheres represent GTP and Mg^{2+} ions, respectively. The HVR in the tube representation is colored light green, and the farnesyl and palmitoyl as sticks are colored yellow and orange, respectively. Highlighted dimer interfaces are shown (right column). In the highlight, yellow dotted lines denote salt bridges and red dotted line indicate the intermolecular backbone hydrogen bonds (H-bonds). Residues involving the hydrophilic and hydrophobic interactions are also marked [197].

MD simulations of the K-Ras4B α -homodimer indicate that E98 forms four salt bridges with R97, and K101. Similarly, R102 forms four salt bridges with D105, and E107 and these interactions are maintained throughout the simulations. β -homodimer simulations show that R41 and K42 forms salt bridges with E37 and D33, respectively. Analyzing the MD trajectories (Tables A.5 and A.6) and considering the FoldX calculations (Tables A.7 and A.8) three mutant sets were selected from each interface (Table 4.1 and Figure 4.9) and charge reversal mutations were performed to disrupt the described electrostatic interactions. S39A+Y40A double mutation was included as our positive control. The hydrogen bonding between S39 residues is a backbone interaction. Thus, as indicated by the energy values substitution of Ser39 should not affect this association.

Table 4.1. Residues selected for site-directed mutagenesis. I will refer the mutations as written in the parenthesis in the text. (A stands for alpha and B stands for beta.)

	Mutants
β-Homodimer	S39A+Y40A (B1)
	R41A+K42A (B2)
	R41E+K42D (B3)
α-Homodimer	E98R (A1)
	K101A+R102A (A2)
	K101D+R102E (A3)

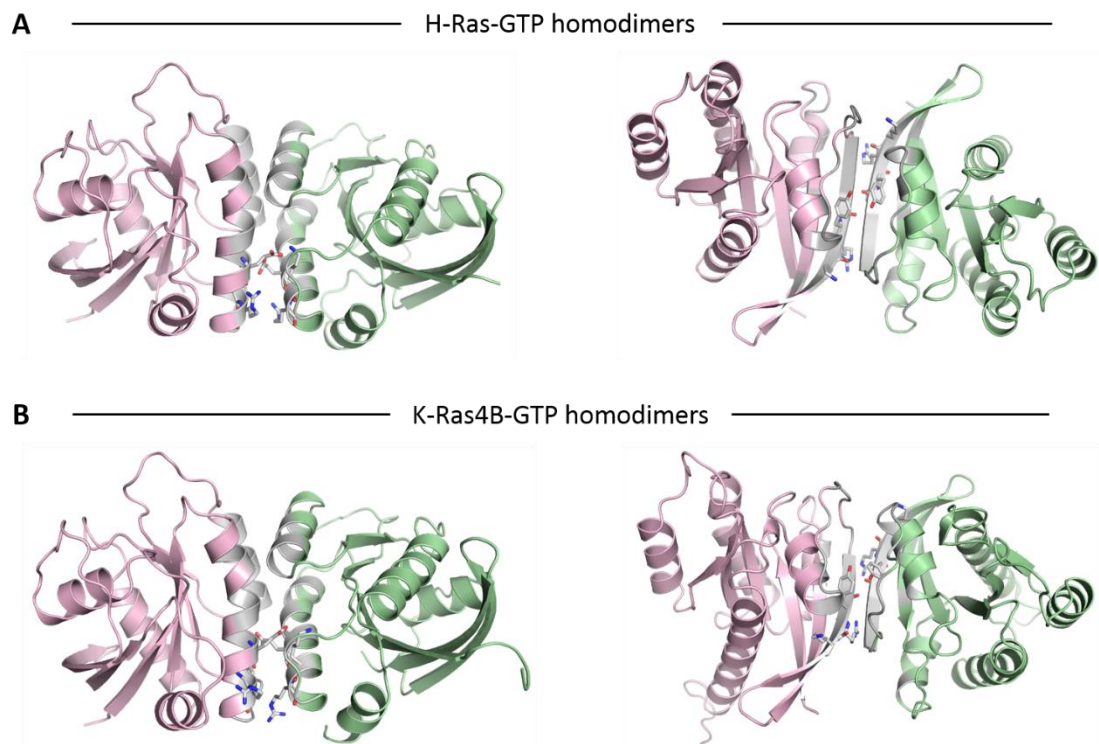


Figure 4.9. Predicted homodimer structures of active H- and K-Ras4B. **A)** Predicted α and β homodimer structures for GTP-bound H-Ras. **B)** Predicted α and β homodimer structures for GTP-bound K-Ras4B. Interface regions are colored gray and the mutated residues (E98, K101, R102 on the α interface and S39, Y40, R41, K42 on the β interface) are shown as sticks.

4.2. Experimental Investigation of H-Ras and K-Ras4B Dimers

4.2.1. Investigation of the interaction by bimolecular fluorescence complementation

Bimolecular fluorescence complementation (BIFC) system was used to investigate Ras-Ras interaction in HEK 293T cells. Wild type or mutant *HRAS/KRAS* cDNA were cloned into pTTB-BiFC as fused with the C- and N-terminal of Venus proteins. Then Sanger sequencing was performed to make sure all cDNAs are in frame with Venus cDNAs and don't contain any mutation possibly can come from PCR amplification. When there is an interaction between different Ras proteins, a strong fluorescence signal was expected due to close proximity of the Venus proteins, fused with Ras proteins.

This expectation will enable us to assess whether Ras proteins interact and in turn yields fluorescence signal. For the proper assessment following controls were included during the course of the experiment. HEK293T cells were transfected with pTTB-BIFC-*HRAS* or pTTB-BIFC-*KRAS* without the pFUW-M2rtTA vector as control, to compare the amount of signals with cells co-transfected with *HRAS/KRAS* and pFUW-M2rtTA. 1ng/mL Dox was used to induce Ras expression from the recombinant pTRE-Tight-BI vector. pTRE-Tight-BI contains a modified Tet response element (TREmod), which consists of seven direct repeats that contains the tet operator sequence (tetO). The multiple cloning sites (MCS) I and MCS II flank the BI-Tet-responsive pTight promoters on either side. Both genes inserted into MCS I and MCS II will be responsive to the rtTA regulatory protein in Tet-On system. The rtTA, expressed from FUW-M2rtTA, binds to tetracycline operator elements (TetO) in the presence of Dox, causing transcriptional activation of genes downstream of TetO.

The presence of a fluorescence signal was detected 3, 6, and 12 hour after Dox induction (Figures 4.10 and 4.11). Cells that express *HRAS/KRAS* genes displayed strong fluorescent signal, which indicates their interaction and also co-localization site, whereas cells transfected only with plasmid that contains *RAS* (No FUW) do not show any fluorescent signal. The signals were mainly around the plasma membrane where Ras is located and suggested that Ras proteins interact. After the verification of interaction between the wild type (H-Ras/K-Ras4B) or oncogenic Ras proteins (H-Ras^{G12V}/K-Ras4B^{G12D}) the fluorescent signal intensities of interface mutants were compared. The cells expressing K101D/R102E double mutants yielded less fluorescence signal compared to the cells expressing the controls (H-Ras^{G12V}/K-Ras4B^{G12D}) suggesting that K101/R102 residues play a role in interaction between Ras proteins. As expected, the fluorescence signals increase over time since the amount of Ras in the cell increases due to the continuous Dox induction.

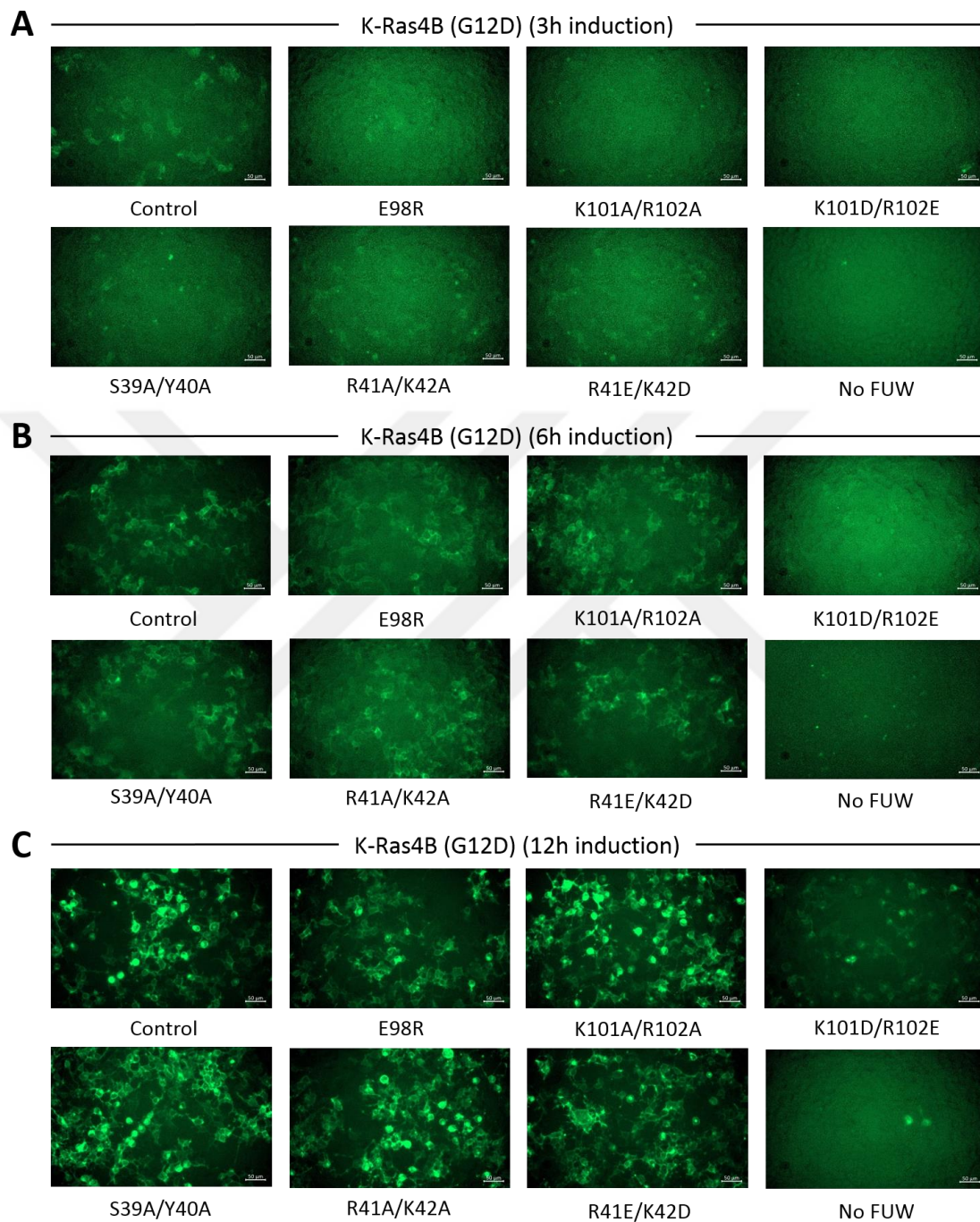


Figure 4.10. K-Ras4B dimerization was confirmed with BIFC system in HEK 293T cells. The images of the cells transfected with Ras mutants were taken (A) 3 (B) 6 and (C) 12h after 1 ng/mL Dox-induction. Scale bar: 50 μ m

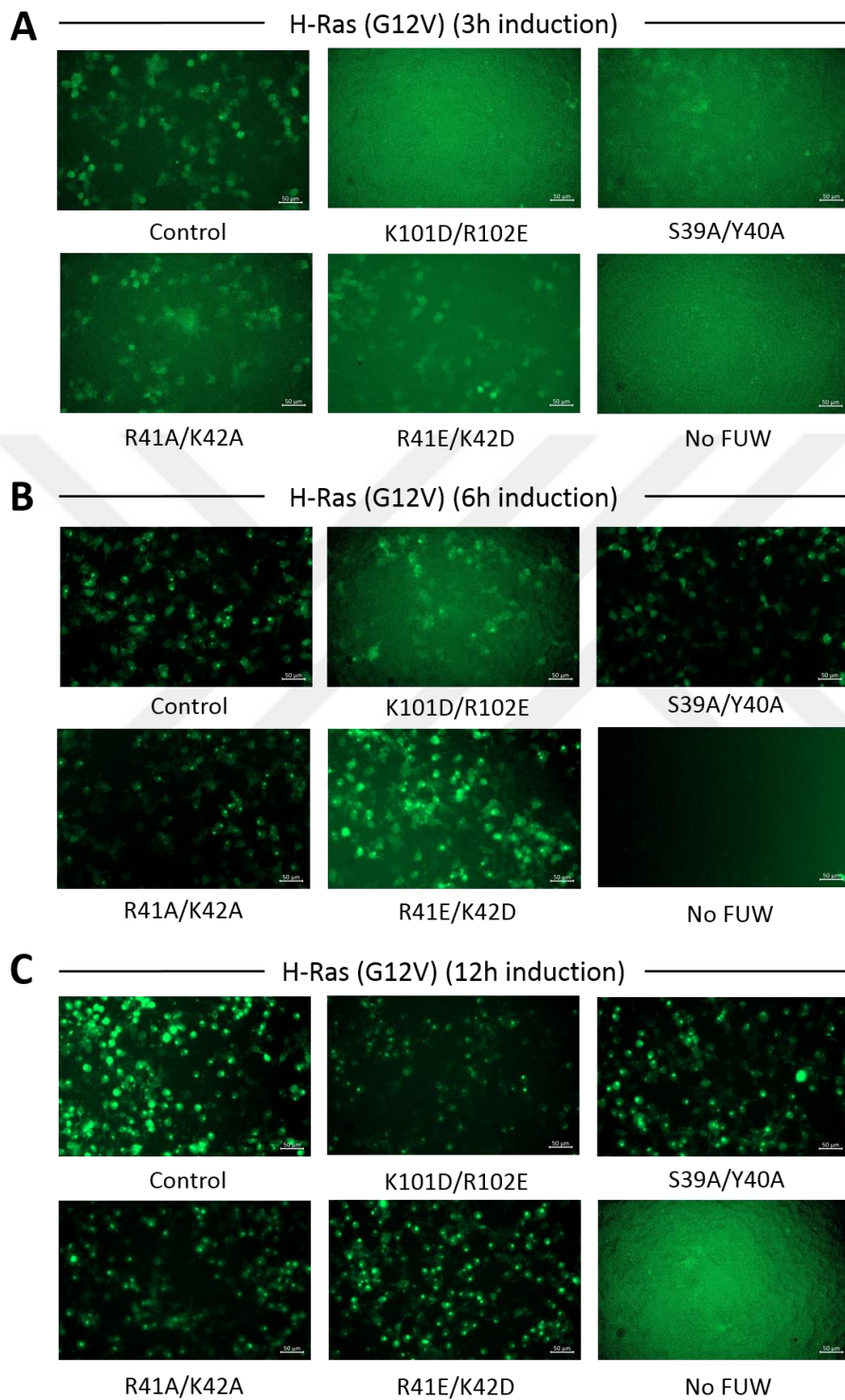


Figure 4.11. H-Ras dimerization was confirmed with BIFC system in HEK 293T cells. The images of the cells transfected with Ras mutants were taken (A) 3 (B) 6 and (C) 12h after 1 ng/mL Dox-induction. Scale bar: 50 μ m

Ras dimerizes and activates Raf when it localizes at the plasma membrane. Thus, to determine where the dimerization takes place, the cells were transfected with constitutively active and interface mutant plasmids and analyzed with confocal microscopy by Assist. Prof. Elif Nur Fırat Karalar. As expected, imaging showed that for K-Ras^{G12D} BiFC signals were predominantly in the membrane, whereas the BiFC signal was weak and diffused throughout the cytoplasm for K-Ras4B^{G12D/K101D/R102E} (Figure 4.12). In K-Ras4B^{G12D/R41E/K42D} mutant, the BiFC signal was dispersed in the cytoplasm and membrane. In addition, Venus intensity of the R41E/K42D mutant was 133.1 ± 2.7 relative to the K-Ras^{G12D} control, indicating that this mutant dimerizes. However, the relative Venus intensity of the K101D/R102E mutants is 47.49 ± 7.5 relative to the K-Ras^{G12D} control, suggesting that the mutant is defective in dimerization (Figure 4.12B). Together, these results suggest that residues K101 and R102, but not R41 and K42, amino acids were required for K-Ras dimerization. Reversing the charges at these residues also interfered with plasma membrane localization of mutant K-Ras^{G12D} dimers. None of the catalytic domain residues indeed are specifically involved in plasma membrane association of K-Ras, it is the farnesylated HVR that mediates the interaction between K-Ras and plasma membrane. However, decreasing net charge by substituting the positively charged residues with the negatively charged ones may increase the fluctuations of the HVR with respect to the membrane, thus weaken the interaction. Changes in mutant K-Ras^{G12D} location might also be due to electrostatic repulsion occurring between the negatively charged residues and membrane.

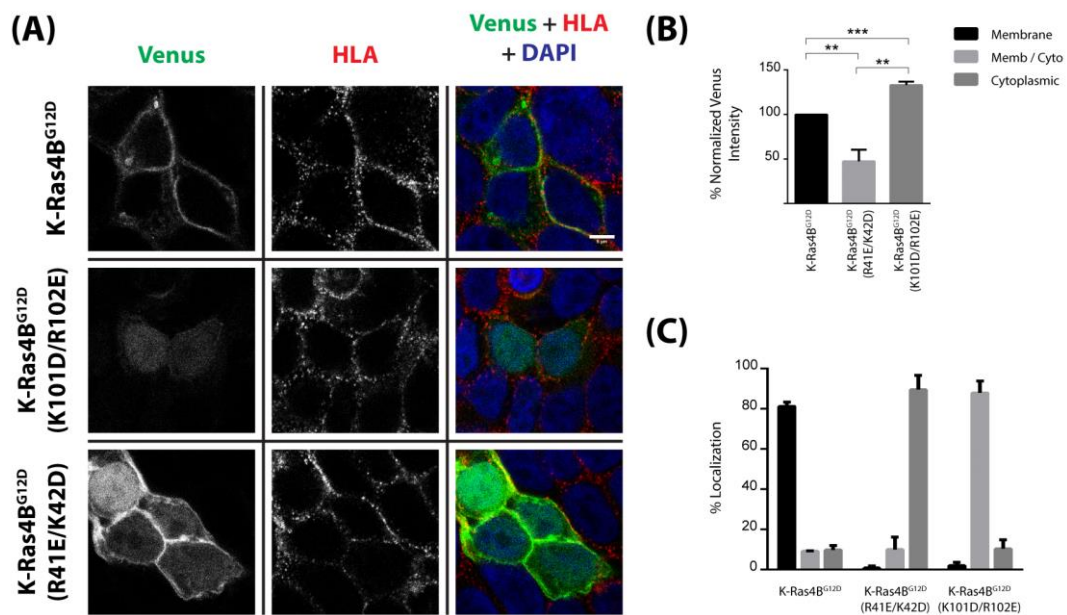


Figure 4.12. Charge reversal mutations decrease Ras dimerization and interfere with Ras membrane localization. **A)** Confocal microscopy of HEK 293T cells transfected with pTTB-KRAS4B constructs (K-Ras^{G12D}, K-Ras^{G12D}/K101D/R102E and K-Ras^{G12D}/R41E/K42D), FUW-M2rtTA and pmScarlet-H_C1. **B)** Normalized Venus intensity of the transfected HEK293T cells. **C)** Localization of the Ras dimers in transfected HEK293T cells. Cells where Venus co-localizes with HLA were counted as membrane-positive, cells where Venus co-localizes with Scarlet were counted as cytoplasm-positive and cells where Venus co-localizes with both Scarlet and HLA were counted as membrane and cytoplasm-positive. Quantification was based on two independent experiments.

Here, I validate our previously-proposed dimer structures through site-directed mutagenesis of selected interface residues. The β -homodimer interface overlaps with the majority of the Ras-effector binding regions including major Ras effectors, Raf and PI3K. Thus, in principle, depending on its exact location with respect to the specific interface, a mutation on these interfaces might affect both Ras-Ras and Ras-effector associations. The helical dimer, on the other hand, may promote Raf dimerization and enhance MAPK signaling; but likely not PI3K, nor other Ras effectors which act as monomeric units [158, 161]. I applied BiFC to investigate Ras-Ras interaction in HEK

293T cells. Quantification of the BiFC Venus signal indicates that charge reversal mutations on K101 and R102 (K101D/R102E) located at the α -dimer interface reduced Ras-Ras association. Interestingly, in double interface mutants, dimers were observed both in the cytoplasm and on the membrane surface unlike the control in which dimerization occurs mainly in the plasma membrane (PM) where Ras is functional. Differences in the subcellular localization of the dimers may relate to unfavorable mutant Ras environment at the PM due to the modified charges at the surface of a protein facing the membrane [211-213]. However, such an observation indicate that K-Ras monomers could associate in cytoplasm supporting that Ras can form dimers in solution [206].

4.2.2. Determination of the Ras expression and pERK, pAKT levels upon mutation

To understand the effect of Ras-Ras interaction on function, phosphorylation of ERK and AKT were measured in HEK 293T cells transfected with oncogenic/mutant pTTB-KRAS constructs by Western blot analysis K101D/R102E and R41E/K42D double mutants were specifically used because K101/R102 residues are located at the helical dimer interface and K102D/R102E seems to affect dimerization and R41/K42 residues are located at the beta dimer interface and overlaps the Raf binding site.

Before the functional assays, the expression levels of the mutant proteins were checked to see whether they are comparable with wild type proteins. Analysis of the Western results indicate that the level of the K101D/R102E and R41E/K42D double mutants were low compared to wild type proteins (Figures 4.13 and 4.14). The decrease in the protein levels may result from a problem at the expression level or these mutations decrease protein stability and promote protein misfolding/degradation. The latter is more reasonable since two charge reversal mutations were introduced into the structure. Mutagenesis studies where ionizable surface residues are perturbed and the fact that pH affects the stability of the proteins indicate that electrostatic interactions are significant for the stability of proteins. Thus, introducing two charge reversal mutations disrupts electrostatic interactions leading to decreased Ras stability.

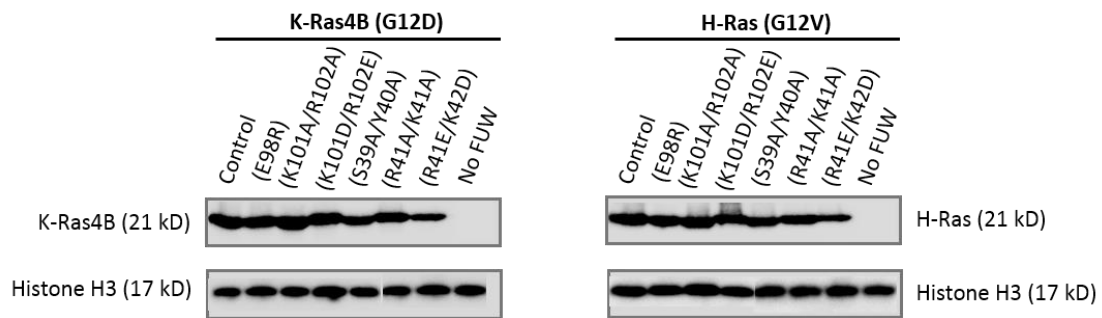


Figure 4.13. Western blot analysis for expression of K-Ras4B^{G12D}, H-Ras^{G12V} and their interface mutants 24 h after Dox-induction. Cells transfected with only pTTB-Ras (without FUW-M2rtTA: no FUW) were used to show that Ras expression depends on the presence of rtTA.

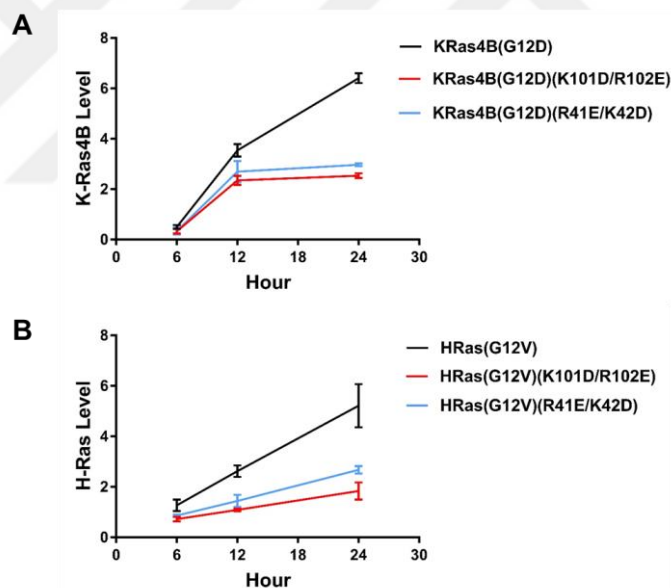


Figure 4.14. Comparison of the protein levels of (A) K-Ras4B^{G12D}, K-Ras4B^{G12D/K101D/R102E}, and K-Ras4B^{G12D/R41E/K42D} (B) H-Ras^{G12V}, H-Ras^{G12V/K101D/R102E} and H-Ras^{G12V/R41E/K42D} 6, 12, and 24 h after Dox-induction.

Among the seven key Ras effectors (RIN1, PLC ζ , Ral guanine nucleotide dissociation stimulator (RalGDS), phosphatidylinositol 3-kinase (PI3K), Raf, Tiam1, RASSF [1]), Raf plays major roles in primary pathways in the cell. Raf (A-Raf, B-Raf, and Raf-1,

also called C-Raf) is a MAPK kinase kinase (MAP3K). Distinct Raf isoforms relate to specific Ras isoforms and cancer types, e.g. B-Raf is the primary isoform associating with K-Ras4B. The Ras/Raf/MAPK pathway is a major mechanism by which mitogens stimulate cell proliferation. Activated Raf activates MEK1/2 that can phosphorylate and activate ERK1/2. ERK phosphorylates cytoplasmic signaling proteins, including p90 ribosomal S6 kinase (RSK), and transcription factors, like the ETS family, which regulate the expression of c-Fos and c-Jun, which activates AP1.

Here, the effects of K102D/R102E, and R41E/K42D double mutations were investigated on phosphorylated ERK (pERK) levels. As the results indicate both mutations in K-Ras4B decrease pERK concentration compared to the K-Ras4B^{G12D}, however, this decrease is coupled with the decrease in Ras level. When the difference in Ras concentrations were taken into account and the results were normalized accordingly, there was no significant decrease in pERK levels in K-Ras4B^{G12D/K102D/R102E} (Figure 4.15A). Thus, the results suggest that K102D/R102E double mutation decreases Ras concentration in the cell, and downregulates ERK phosphorylation. In H-Ras^{G12V} case, K102D/R102E double mutation do not affect the pERK levels at all, but still decreases the Ras concentration. In K-Ras4B^{G12D/R41E/K42D} and H-Ras^{G12V/R41E/K42D} mutants, on the other hand, a significant decrease in pERK levels was observed even after the normalization (Figure 4.15). This is an expected result, since these residues are located at the Ras-Raf interface, thus can affect with Raf binding (Figure 4.18). At first, Histone H3 was used as a loading control, however, since it is a nuclear protein involved in structure of chromatin, the total H3 protein levels may not be equal. Thus, the experiments were repeated using vinculin, membrane-cytoskeletal protein, as a loading control (Figure 4.16). Both experiments yielded similar results, indicating that R41E/K42D double mutation decreases Ras concentration in the cell, and interferes with Raf binding, thus downregulates ERK phosphorylation.

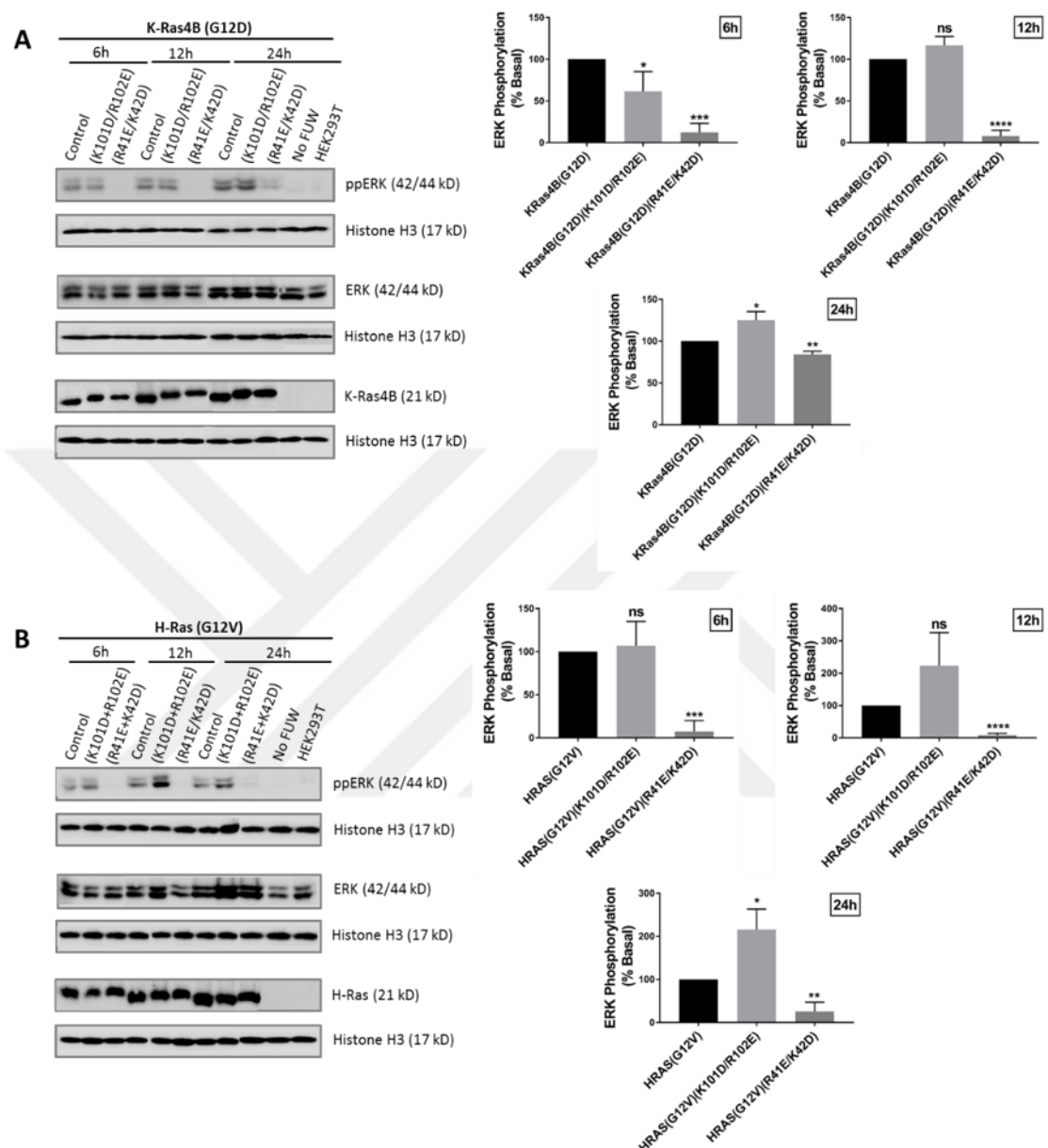


Figure 4.15. Effect of interface mutations on **A**) K-Ras4B and **B**) H-Ras mediated ERK phosphorylation in HEK293T cells. Cells were co-transfected with FUW-M2rtTA and Myc-tagged Ras (K-Ras4B^{G12D}, K-Ras4B^{G12D/K101D/R102E}, K-Ras4B^{G12D/R41E/K42D}, H-Ras^{G12V}, H-Ras^{G12V/K101D/R102E} or H-Ras^{G12V/R41E/K42D}) and phosphorylation of ERK at 6, 12, and 24h was detected by Western blot with phosphospecific ERK antibodies. Cells transfected with only Ras (No FUW), and non-transfected HEK293T cells were used as controls. Error bars represent means + SEM (n = 3). Corresponding analysis of Western blots relative to Histone H3 and Ras are presented in the *right panels*. All *p* values were

obtained using Student t test, **** $p \leq 0.0001$, *** $p \leq 0.001$, ** $p \leq 0.01$, * $p \leq 0.05$, ns $p > 0.05$.

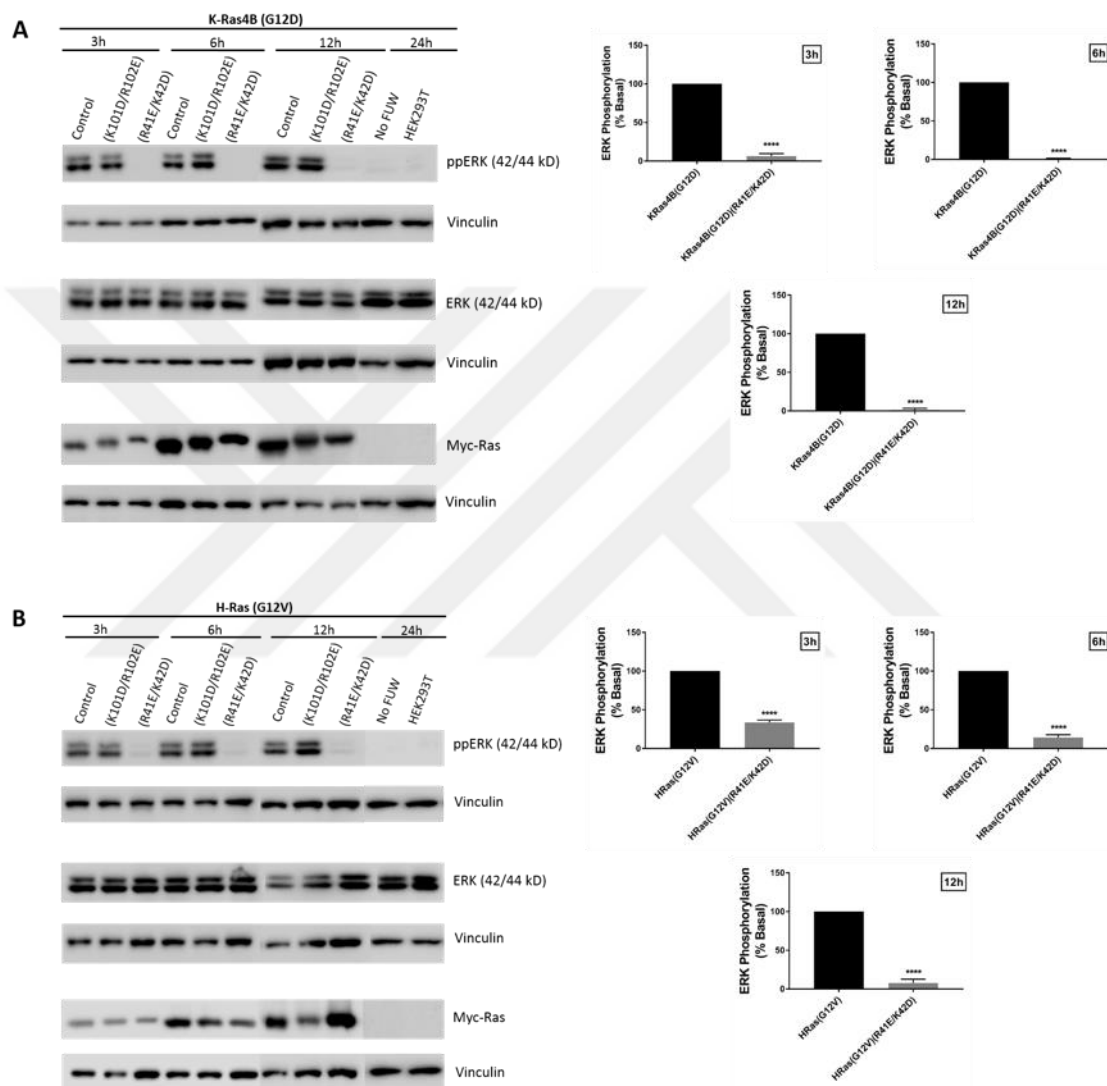


Figure 4.16. Effect of interface mutations on **A)** K-Ras4B and **B)** H-Ras mediated ERK phosphorylation in HEK293T cells. Cells were co-transfected with FUW-M2rtTA and Myc-tagged Ras (K-Ras4B^{G12D}, K-Ras4B^{G12D/K101D/R102E}, K-Ras4B^{G12D/R41E/K42D}, H-Ras^{G12V}, H-Ras^{G12V/K101D/R102E} or H-Ras^{G12V/R41E/K42D}) and phosphorylation of ERK at 6, 12, and 24h was detected by Western blot with phosphospecific ERK antibodies. Cells transfected with only Ras (No FUW), and non-transfected HEK293T cells were used as controls. Error bars represent means + SEM (n = 3). Corresponding analysis of Western

blots relative to vinculin and Ras are presented in the *right panels*. All p values were obtained using Student t test, **** $p \leq 0.0001$.

Though microscopy and western data were collected at 3rd, 6th, 12th and 24th hours, confocal images indicate a decrease in Ras dimerization at third hour. Thus, I focused on the third hour and checked the expression levels of the K-Ras4B^{G12D} interface mutants to see whether they are comparable with K-Ras4B^{G12D} proteins. The assays showed that they were not affected significantly. However, there is a slight shift in the lanes which may indicate that mutants Ras might undergo increased post-translational modifications.

Ras activation induces the downstream phosphorylation and activation of ERK1/2 and Akt serine/threonine kinases in the two major Ras signaling pathways: Ras-Raf-MEK-ERK and PI3K/Akt, respectively. The levels of phosphorylated ERK and AKT were measured by Western blot using anti-ppERK and -pAKT. Unexpectedly, constitutively active K-Ras^{G12D} overexpression in HEK 293T cells led only to the enhancement in the activation of the ERK signaling pathway and not the PI3K/Akt signaling pathway. Results indicated that mutagenesis of K101 and R102 to aspartate and glutamate, respectively, resulted in approximately a 20% reduction in ERK phosphorylation in K-Ras4B^{G12D}, whereas mutagenesis of R41 and K42 to glutamate and aspartate, respectively, almost abrogated ERK phosphorylation. Interestingly, mutagenesis of both sites increased Akt phosphorylation, thus almost restored to HEK 293T levels (Figure 4.17).

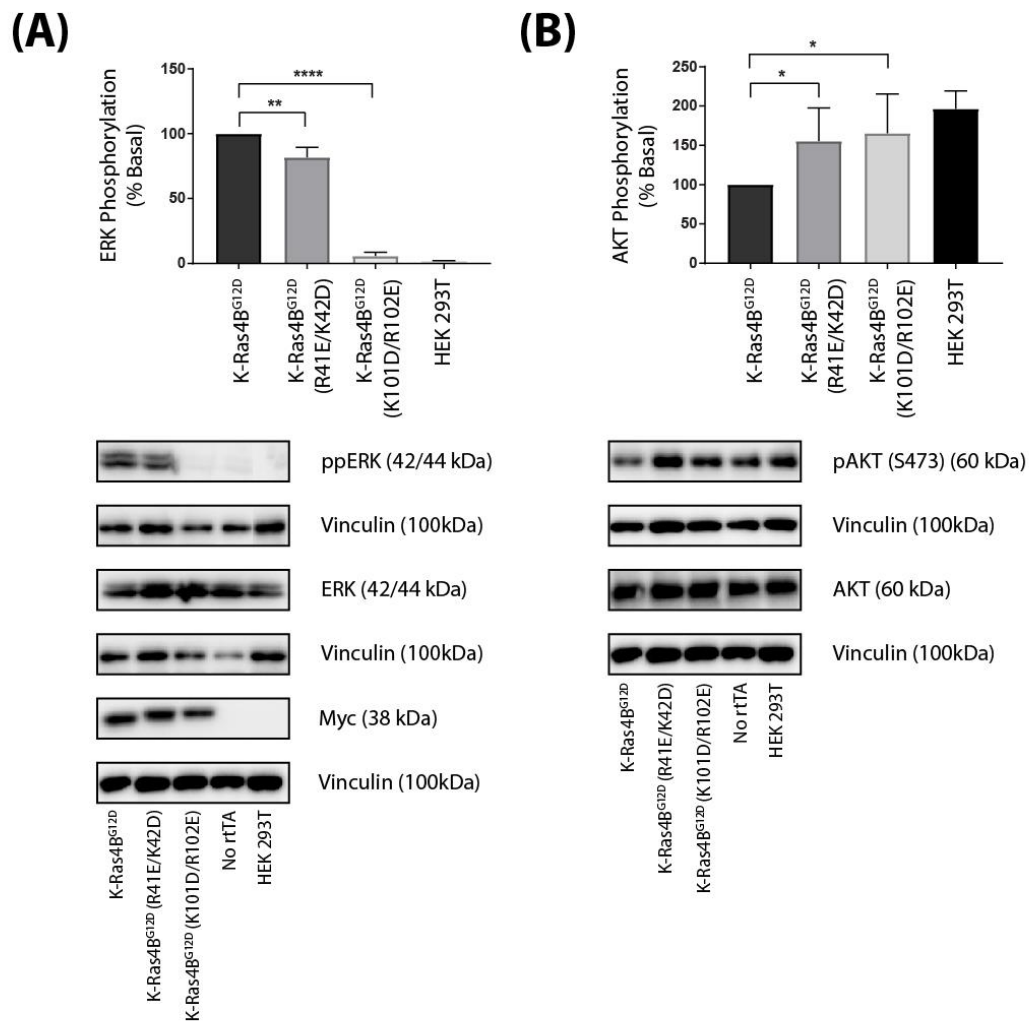


Figure 4.17. K101D/R102E and R41E/K42D reduce ERK phosphorylation, but increase Akt phosphorylation. Effect of interface mutations on K-Ras mediated **A)** ERK and **B)** Akt phosphorylations in HEK 293T cells. Cells were co-transfected with FUW-M2rtTA and Myc-tagged K-Ras (K-Ras4B^{G12D}, K-Ras4B^{G12D}/K101D/R102E or K-Ras4B^{G12D}/R41E/K42D) and phosphorylation of ERK at 3 h was detected by Western blot with phosphospecific ERK antibodies. Cells transfected with only Ras (No FUW), and non-transfected HEK 293T cells were used as controls. Error bars represent means + SEM (n = 3). Corresponding analysis of Western blots relative to vinculin and Ras are presented in the *upper panels*. All p values were obtained using Student t test, ****p < 0.0001, ***p < 0.001, **p < 0.01, *p ≤ 0.05, ns p > 0.05.

The key question was whether the interface mutants (K-Ras4B^{G12D/K101D/R102E}, and K-Ras4B^{G12D/R41E/K42D}) can induce ERK and Akt signaling pathways. ERK1/2 and Akt are the downstream serine/threonine kinases in the Ras-Raf-MEK-ERK and PI3K/Akt signal transduction cascades, respectively. Western blot analysis indicated that double mutation K101D/R102E reduced ERK phosphorylation by 20% in cells transfected with mutant pTTB-KRAS supporting the role of dimerization in ERK signaling; but not Akt. Notably, due to the long linker connecting Raf's CRD (cysteine-rich domain, which is adjacent to Raf's Ras binding domain, RBD) and the kinase domain, spatial proximity between Ras G-domains would allow Raf's kinase domain dimerization, as observed here. Double mutant R41E/K42D of K-Ras, on the other hand, almost completely abrogated ERK phosphorylation in HEK 293T cells, though quantification of BiFC signals suggest that this mutant can dimerize. The apparent decrease in phospho-ERK levels may arise from interference with Raf binding since R41 is located at the Ras-Raf interface and is a hot spot (Figure 4.18). Interestingly, biochemical data indicate that K-Ras4B^{G12D} overexpression did not increase Akt phosphorylation in HEK 293T cells. Introducing both charge reversal double mutations, however, restored Akt activity.

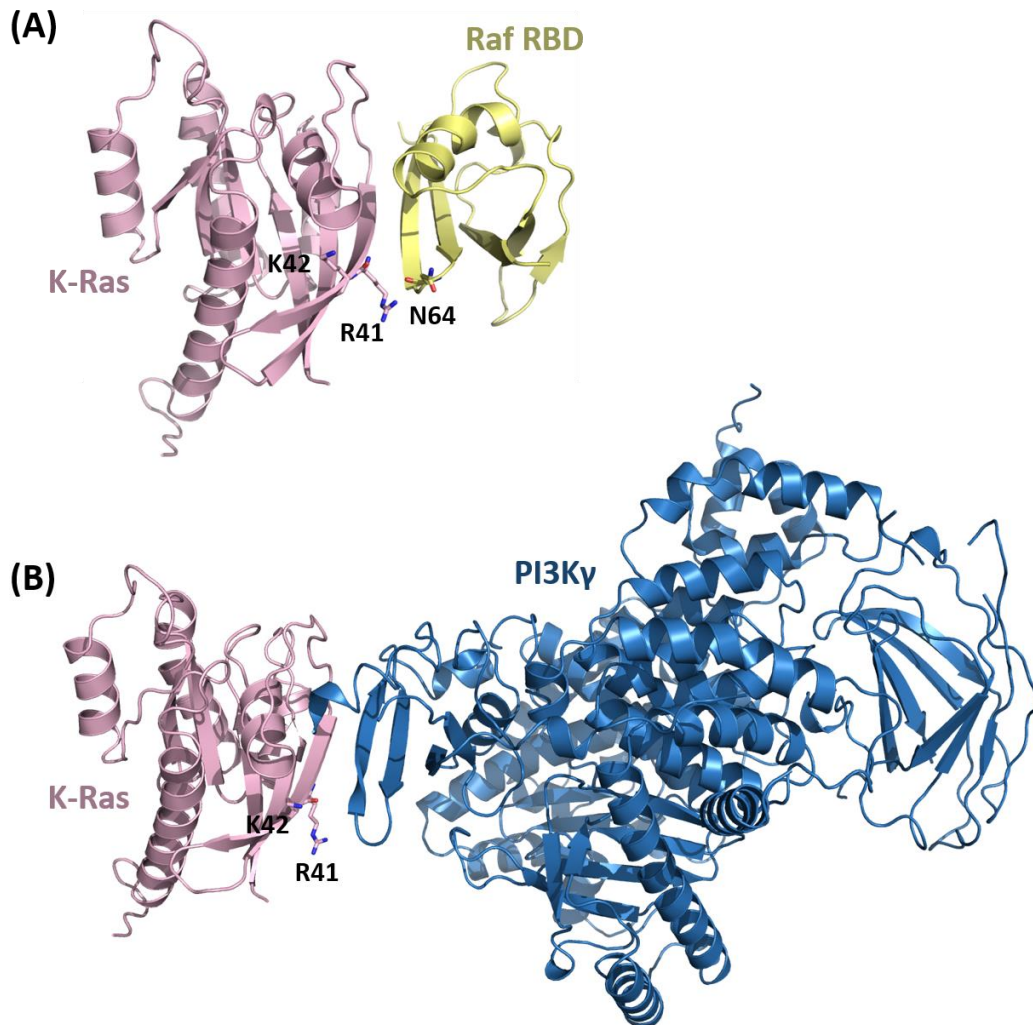


Figure 4.18. **A)** Predicted complex structure of K-RasG12D G-domain (PDB ID: 4DSO) with Ras binding domain (RBD) of Raf-1 (PDB ID: 4G0N). R41 forms H bonds with N64 on Raf RBD. **B)** Predicted complex structure of K-RasG12D G-domain (PDB ID: 4DSO) with catalytic subunit of PI3K γ (PDB ID: 1E8Y). Ras uses the same β -sheet extension motif in the β -homodimer and in Ras-Raf, Ras-PI3K. The mutated residues are shown as pink sticks.

4.2.3. Determination of the mRNA levels of Ras-regulated genes

To examine the effect of K-Ras mutations on MAPK- and Akt- regulated gene expression, we selected six downstream genes whose expressions are controlled by Ras. Three of these (JUN, FOS and EGR1) are downstream genes regulated by MAPK

pathway, while *BCL2L11* is regulated by both ERK and PI3K/AKT pathways (Figure 4.19 A). pTTB-KRAS constructs carrying constitutively active and interface mutants of KRAS were transfected into HEK 293T cells. Approximately 10 h after transfection, K-Ras expression was induced with 1 ng/mL Dox. 3h after induction, the total RNA was isolated from the cells and endogenous *JUN*, *FOS*, *EGR1*, and *BCL2L11* mRNA expression were detected by RT-qPCR. The expression data indicate that constitutively active K-Ras overexpression increased *FOS*, and *EGR1* expressions but did not affect *JUN* expression compared to HEK 293T cells. In addition, overexpression of mutant Ras (K-Ras4B^{G12D/K101D/R102E} and K-Ras4B^{G12D/R41E/K42D}) down-regulated *FOS*, and *EGR1* expression, but did not affect *JUN* expression compared to constitutively active K-Ras overexpression (Figure 4.19). Additionally, both mutations decreased *BCL2L11* expression, but the effect is more distinctive in K-RasG12D/K101D/R102E mutant (Figure 4.19 B).

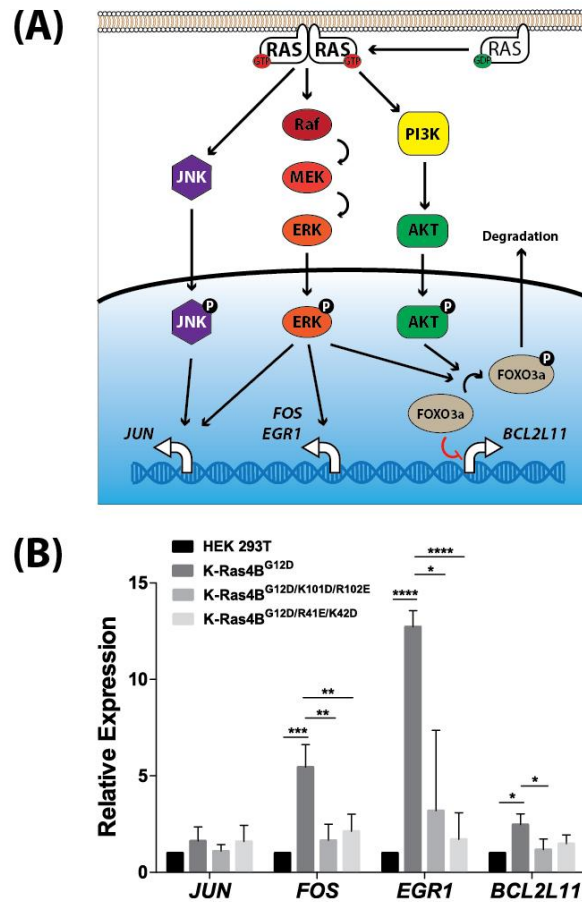


Figure 4.19. Ras mutations cause downregulation of *FOS* and *EGR1* in HEK293T cells. **A)** Schematic models illustrating MAPK-mediated regulation of JUN, FOS, and EGR1 expression and MAPK- and Akt-mediated regulation of BCL2L11 expression. **B)** *JUN*, *FOS*, *EGR1*, and *BCL2L11* gene expression levels in transfected HEK 293T cells were evaluated by real-time PCR, expressed as relative values by the comparative Ct method. Data are mean (\pm standard deviation [SD]) from 3 individual experiments performed in duplicates. Statistically significant differences from control levels are indicated by **** $p < 0.0001$, *** $p < 0.001$, ** $p < 0.01$, * $p \leq 0.05$, ns $p > 0.05$.

ERK1/2 phosphorylate and activate a large number of cytoplasmic and nuclear molecules including regulatory proteins and transcription factors involved in immediate early gene (IEG) expression such as FOS, JUNB, MYC, and EGR1 [214-217]. Phosphorylated active ERK translocates to the nucleus where it phosphorylates Elk-1

transcription factor within its C-terminal domain [218]. Elk-1 forms a ternary complex with a dimer of serum response factor (SRF) at the serum response element (SRE) on the target gene, and activates transcription [52, 53]. Thus, to investigate the outcome of decreased ERK phosphorylation, I looked at the endogenous mRNA levels of immediate early genes (IEGs), JUN, FOS, and EGR1, in HEK 293T cells by RT-qPCR. The data clearly shows that reduced ERK phosphorylation in cells expressing double mutant K-Ras downregulates FOS, and EGR1 expressions indicating that these mutations can decrease uncontrolled growth, and proliferation associated with oncogenic Ras. JUN expression, on the other hand, did not change in cells expressing mutant Ras. This is mainly due to the fact that ERK is not the only regulator of JUN expression. The transcription of JUN is activated upon phosphorylation of c-Jun by various protein kinases, such as ERK1/2 and c-Jun NH2-terminal kinase (JNK) [219, 220]. However, in vivo the primary regulation of JUN expression is by JNK [219, 221]. Dimers of c-Jun and ATF factors bind to TRE binding sites on JUN promoter [222], indicating that c-Jun activates its own expression [223]. Together, these data indicate that introducing charge reversal mutations in positions R41, K42 and K101, R102 impair Ras-mediated ERK signaling, thus can be used to abate MAPK oncogenic activity of Ras.

Both ERK and Akt signaling pathways are involved in the transcriptional control of BCL2L11 gene. ERK and protein kinase B (Akt) can phosphorylate Forkhead box O 3a (FOXO3a) which is responsible for the upregulation of Bim expression, resulting in its degradation or cytoplasmic retention, respectively [224, 225]. ERK can also act post-transcriptionally by promoting Bim phosphorylation and degradation [226]. To investigate how these two major Ras pathways co-regulate BCL2L11 expression, we also looked at the mRNA level of BCL2L11 in HEK 293T cells by RT-qPCR. Mutations at both sites decrease BCL2L11 expression, however the effect is more significant in K101D/R102E double mutation. K101D/R102E double mutant, unlike the R41E/K42D mutant, can still induce ERK phosphorylation which in turn leads to downregulation of BCL2L11 gene through a transcriptional mechanism.

Chapter 5

RAS-EFFECTOR INTERACTIONS

Active Ras proteins transmit the information through a physical interaction with its downstream effector proteins. Therefore, it is of capital importance to determine the complex structures of Ras with these proteins to understand the pathways at the structural level. Crystal structures of the H-Ras with some regulator and effector proteins are available in PDB (Table A.5). These structures indicate that effector binding sites overlap Ras's β -sheet dimer interface. Overlapping interfaces argue for an effective local effector concentration threshold as a regulatory mechanism in activation and signaling. They suggest that Ras-binding domains of these effectors and regulators under certain conditions can compete with K-Ras4B' β -sheet dimer interface. Using PRISM we identified all of the other regulator/effector binding regions on H- and K-Ras. Figures 5.1 and 5.2 show the complex structures of H-Ras and K-Ras4B proteins with their binding partners, respectively.

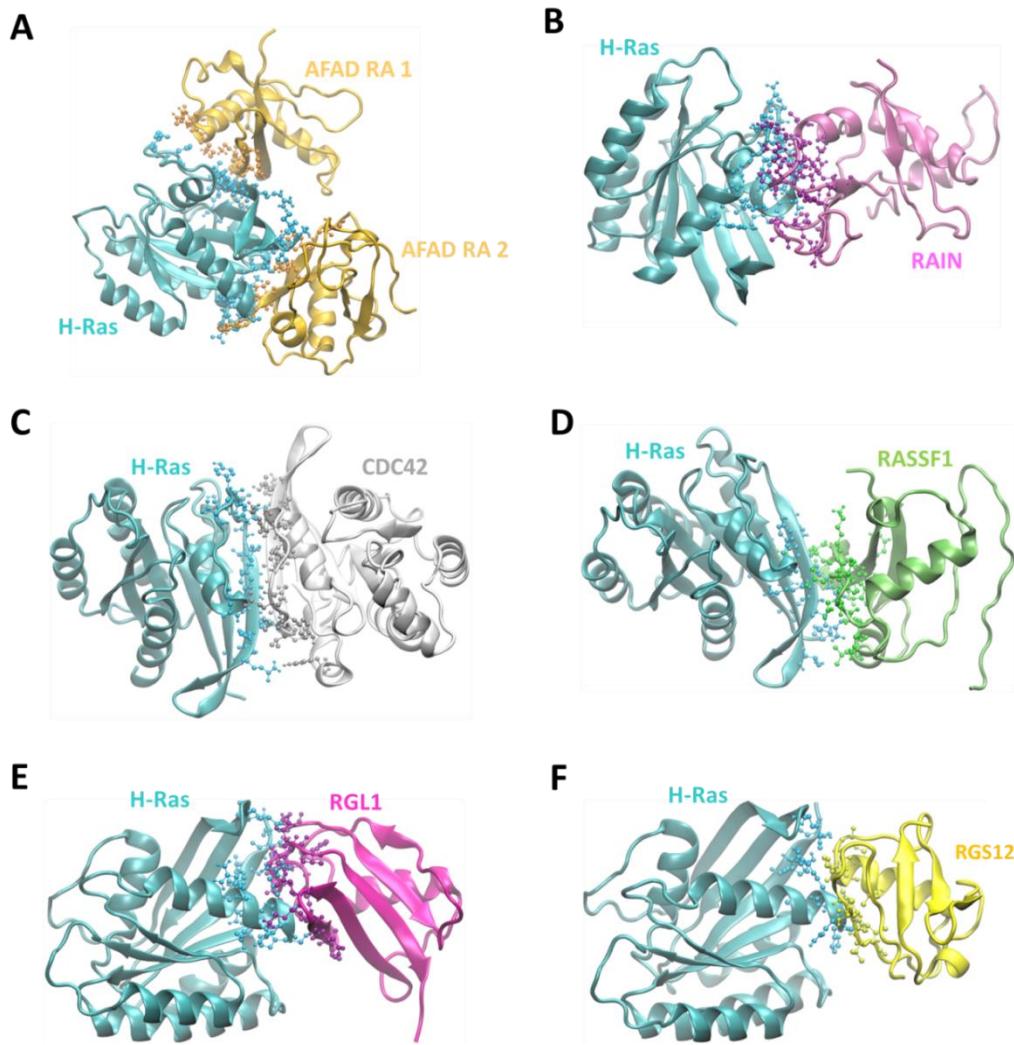
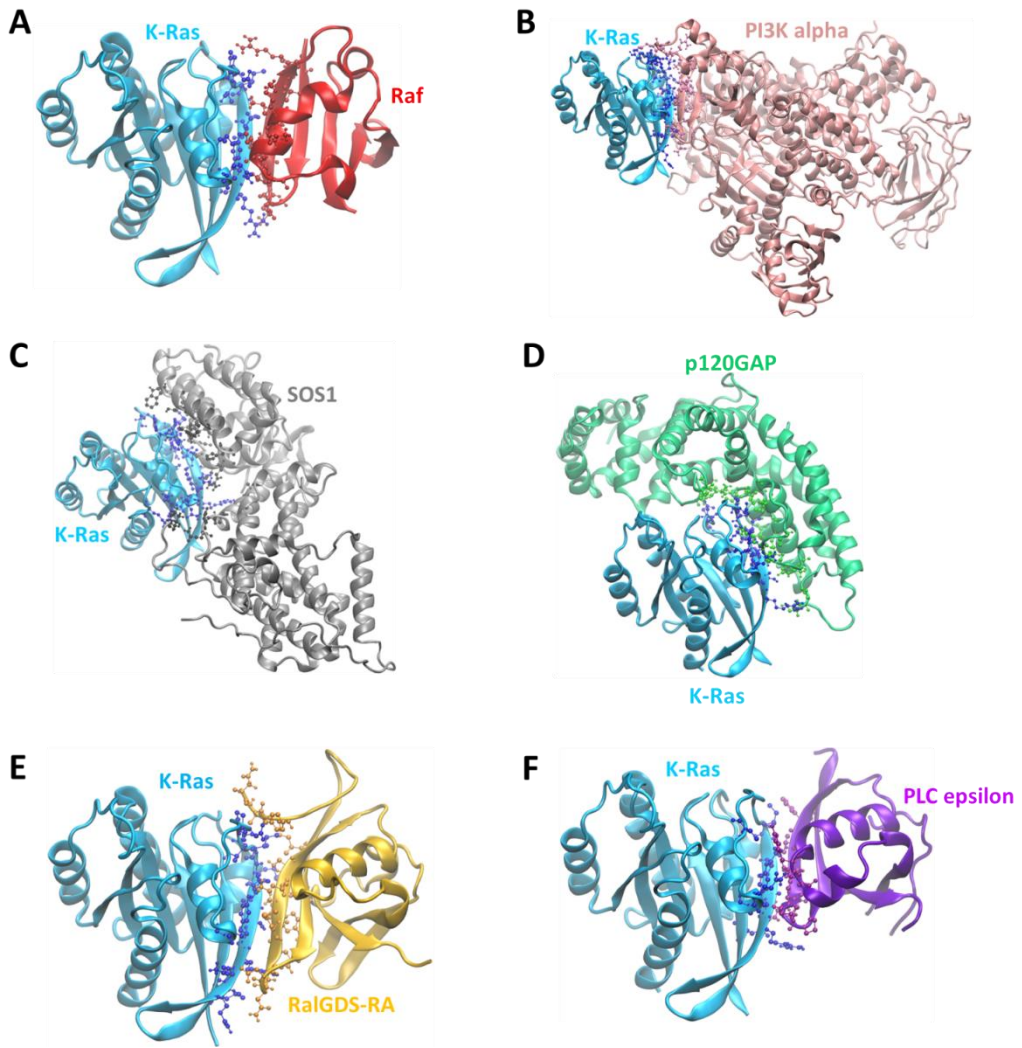


Figure 5.1. **A)** Predicted complex structure of H-Ras (PDB ID: 1QRA) with Ras associating 1 and 2 (RA) domains of Afadin (Models). Binding energy score (BES) for the interaction between H-Ras and AFAD RA 1 is -21.71 . (Template interface: 1lfdCD). Interface residues of H-Ras are E31, D33, I36, E37, D38, S39, R41, Y64, A66, and M67. Interface residues of Afadin are F55, T57, K58, C59, I60, R61, E77, K78, and R80. Binding energy score (BES) for the interaction between H-Ras and AFAD RA 2 is -17.8 . (Template interface: 1mo1AB). Interface residues of H-Ras are M1, T2, E3, K5, T74, E76, K104, S106, D108, P110, and H166. Interface residues of Afadin are S246, G247, G248, T249, R251, Y263, T265, L267, and D310. **B)** Predicted complex structure of H-Ras (PDB ID: 1QRA) with Ras associating (RA) domain of Ras interacting protein 1 (RAIN, Model). Binding energy score (BES) for the prediction is -32.06 . (Template interface: 3iicAB). Residues participating in the interface are shown in ball-and-stick

representation. Interface residues of H-Ras are Q22, L23, I24, Q25, N26, H27, F28, V29, D30, K147, T148, R149, V152, E153, and Y157. Interface residues of RAIN are L208, R210, A211, H225, V238, L241, W242, R243, A244, R245, P246, G247, W248, and R250. **C)** Predicted complex structure of H-Ras (PDB ID: 1QRA) with cell division control protein 42 homolog (Cdc42) (PDB ID: 2NGR). Binding energy score (BES) for the prediction is -26.56 . (Template interface: 2erxAB). Residues participating in the interface are shown in ball-and-stick representation. Interface residues of H-Ras are N26, E31, D33, I36, E37, D38, S39, Y40, R41, K42, Q43, L52 and Y64. Interface residues of Cdc42 are M1, I21, T24, T25, K27, E31, V33, V36, F37, D38, N39, Y40, A41, V42, T43, T52 and Y64. **D)** Predicted complex structure of H-Ras (PDB ID: 1QRA) with Ras associating (RA) domain of Ras association domain-containing protein 1 (RASSF1, Model). Binding energy score (BES) for the prediction is -32.49 . (Template interface: 1whmAB). Residues participating in the interface are shown in ball-and-stick representation. Interface residues of H-Ras are M1, E3, K5, I24, S39, R41, K42, Q42, T50, D54, and T74. Interface residues of RASSF1 are E250, A252, R254, H255, R261, K262, L263, L264, E267, Q268, L272 and L275. **E)** Predicted complex structure of H-Ras (PDB ID: 1QRA) with Ras associating (RA) domain of Ral guanine nucleotide dissociation stimulator-like 1 (RGL1, Model). Binding energy score (BES) for the prediction is -35.4 . (Template interface: 1fr3AB). Residues participating in the interface are shown in ball-and-stick representation. Interface residues of H-Ras are M1, T2, E3, Y4, E49, E76, V160, I163, R164, Q165, H166. Interface residues of RGL1 are D648, E704, K706, E707, L708, V709, F717, Y718, A719, M720, N721, S722, Q723, and V724. **F)** Predicted complex structure of H-Ras (PDB ID: 1QRA) with Ras binding domain 1 (RBD) of Regulator of G-protein signaling 12 (RGS12, Model). Binding energy score (BES) for the prediction is -14.28 . (Template interface: 1fr3AB). Residues participating in the interface are shown in ball-and-stick representation. Interface residues of H-Ras are T2, Y4, E49, I163, R164, Q165, and H166. Interface residues of RGS12 are S973, C974, V975, V976, L991, E993, R994, H995, and G996.



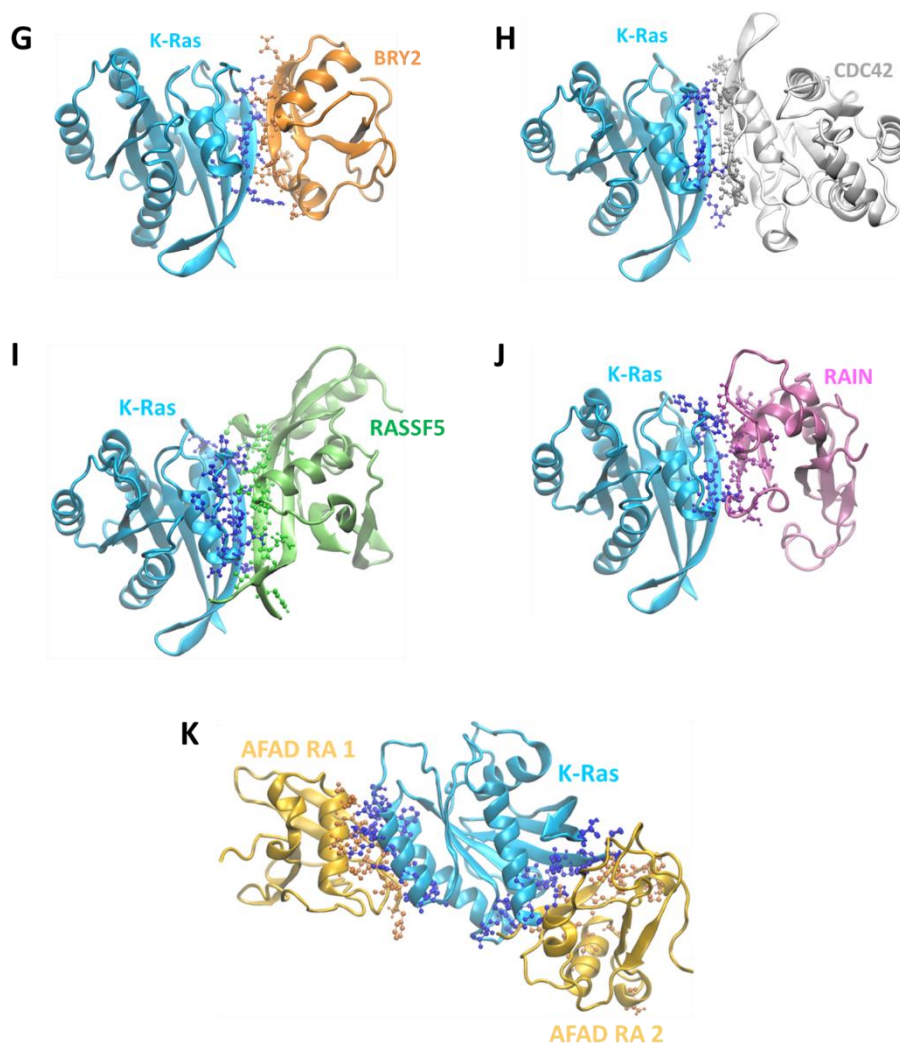


Figure 5.2. **A)** Predicted complex structure of K-Ras4B (PDB ID: 3GFT) with Ras binding domain (RBD) of Raf kinase (PDB ID: 1C1Y). Binding energy score (BES) for the prediction is -51.19. (Template interface: 1c1yAB). Residues participating in the interface are shown in ball-and-stick representation. Interface residues of K-Ras4B are I21, Q25, V29, D30, D33, I36, E37, D38, S39, Y40, R41, D54, and L56. Interface residues of Raf are T57, N64, K65, Q66, R67, T68, V69, K84, V88, R89, G90. **B)** Predicted complex structure of K-Ras4B (PDB ID: 3GFT) with Ras binding domain (RBD) of PI3K p110 α (PDB ID: 2RD0). Binding energy score (BES) for the prediction is -23.24. (Template interface: 1lfdCD). Residues participating in the interface are shown in ball-and-stick representation. Interface residues of K-Ras4B are I24, Q25, D30, E31, D33, I36, E37, D38, S39, Y40, R41, K42, Q43, M67 and Q70. Interface

residues of PI3K α are W195, N201, N202, D203, K204, Q205, K206, T208, K227, R230, S231, M232, L233, and M282. **C)** Predicted complex structure of K-Ras4B (PDB ID: 3GFT) with Son of sevenless homolog 1 (Sos 1) (PDB ID: 1BKD). Binding energy score (BES) for the prediction is -37.47. (Template interface: 1nvuQS). Residues participating in the interface are shown in ball-and-stick representation. Interface residues of K-Ras4B are Q22, I24, Q25, N26, Y32, D33, P34, T35, I36, E37, D38, S39, Y40, R41, L56, H61, M67, Q70, and R149. Interface residues of Sos 1 are H616, M617, Y618, P621, N622, R625, P684, L687, R688, N691, R694, H699, W729, S732, R739, I752, A965, E966, G969, Q973, N976, and Q977. **D)** Predicted complex structure of K-Ras4B (PDB ID: 3GFT) with Ras-specific GTPase-activating protein (GAP) p120GAP (PDB ID: 1WQ1). Binding energy score (BES) for the prediction is -23.16. (Template interface: 1wq1GR). Residues participating in the interface are shown in ball-and-stick representation. Interface residues of K-Ras4B are S17, I21, Q25, H27, Y32, D33, P34, T35, I36, E37, D38, S39, Y40, R41, H61, E63, A66, and M67. Interface residues of p120GAP are T785, R789, E799, P832, S833, L902, R903, C906, L910, N911, I931, A934, K935, Q938, N942, V944, G947, A948, K949, E950, and Y952. **E)** Predicted complex structure of K-Ras4B (PDB ID: 3GFT) with Ras-associating (RA) domain of RalGDS (PDB ID: 3KH0). Binding energy score (BES) for the prediction is -45.24. (Template interface: 1lfdCD). Residues participating in the interface are shown in ball-and-stick representation. Interface residues of K-Ras4B are D33, P34, T35, I36, E37, D38, S39, Y40, R41, K42, and L52. Interface residues of RalGDS are N787, L788, Y789, I801, R803, D809, N810, G811, N812, M813, Y814, K815, S816. **F)** Predicted complex structure of K-Ras4B (PDB ID: 3GFT) with phospholipase C epsilon (PLC ϵ) (PDB ID: 2C5L). Binding energy score (BES) for the prediction is -37.26. (Template interface: 1lfdCD). Residues participating in the interface are shown in ball-and-stick representation. Interface residues of K-Ras4B are I36, E37, D38, S39, Y40, R41, D54, M67 and Q70. Interface residues of PLC ϵ are F2138, P2146, E2147, Q2148, P2149, R2150, T2151, V2152, Y2174, and S2175. **G)** Predicted complex structure of K-Ras4B (PDB ID: 3GFT) with Bry2 protein kinase (Bry2) (PDB ID: 1K8R). Binding energy score (BES) for the prediction is -43.5. (Template interface: 1k8rAB). Residues participating in the interface are shown in ball-and-stick representation. Interface residues of K-Ras4B are I24, Q25, V29, I36, E37, D38, S39, Y40, R41, and D54.

Interface residues of Bry2 are I72, R74, G80, Q81, T82, R83, A84, V85, Q86, K101, D142, E156, R160, and E165. **H)** Predicted complex structure of K-Ras4B (PDB ID: 3GFT) with the cell division control protein 42 homolog (Cdc42) (PDB ID: 2NGR). Binding energy score (BES) for the prediction is -18.29. (Template interface: 2erxAB). Residues participating in the interface are shown in ball-and-stick representation. Interface residues of K-Ras4B are Q25, H27, E31, D33, I36, E37, D38, S39, Y40, R41, and M67. Interface residues of Cdc42 are T25, K27, S30, E31, V33, V36, F37, D38, N39, Y40, A41, V42, and T43. **I)** Predicted complex structure of K-Ras4B (PDB ID: 3GFT) with Ras association domain-containing protein 5 (RASSF5, Model). Binding energy score (BES) for the prediction is -51.49. (Template interface: 1lfdCD). Residues participating in the interface are shown in ball-and-stick representation. Interface residues of K-Ras4B are I21, I24, Q25, N26, H27, V29, D30, D33, P34, T35, I36, E37, D38, S39, Y40, R41, and M67. Interface residues of Cdc42 are T25, K27, S30, E31, V33, V36, F37, D38, N39, Y40, A41, V42, S65, A66, M67, and Q70. **J)** Predicted complex structure of K-Ras (PDB ID: 3GFT) with Ras associating (RA) domain of Ras interacting protein 1 (RAIN, Model). Binding energy score (BES) for the prediction is -8.31. (Template interface: 1lfdCD). Residues participating in the interface are shown in ball-and-stick representation. Interface residues of K-Ras are I21, I24, Q25, E31, Y32, D33, P34, T35, I36, E37, D38, S39, and Y40. Interface residues of RAIN are A156, S157, G158, A159, N160, Y161, K162, S163, L165, E181, R182, G184 and P189. **K)** Predicted complex structure of K-Ras (PDB ID: 1QRA) with Ras associating 1 and 2 (RA) domains of Afadin (Models). Binding energy score (BES) for the interaction between K-Ras and AFAD RA 1 is -32.66. (Template interface: 2pmcAB). Interface residues of K-Ras are T87, K88, F90, E91, H94, T124, V125, D126, K128, Q129, D132, L133, S136, and Y137. Interface residues of Afadin are F39, H40, G41, V42, C59, I60, R61, V62, S63, D70, E73, T74, E77, and K78. Binding energy score (BES) for the interaction between K-Ras and AFAD RA 2 is -31.2. (Template interface: 1mo1AB). Interface residues of K-Ras are M1, T2, E3, Y4, K5, T50, T74, E76, K104, D108, I163, H166, and K167. Interface residues of Afadin are S246, G247, G248, T249, L250, R251, Y253, Y263, T265, L267, D310, L326, F329, R330, I338, and L339.

We used HotRegion to identify the hotspot residues and hot regions on modelled Ras-Ras homodimer and Ras-effector heterodimer interfaces. (Tables A.7 and A.8, Figure 5.3).

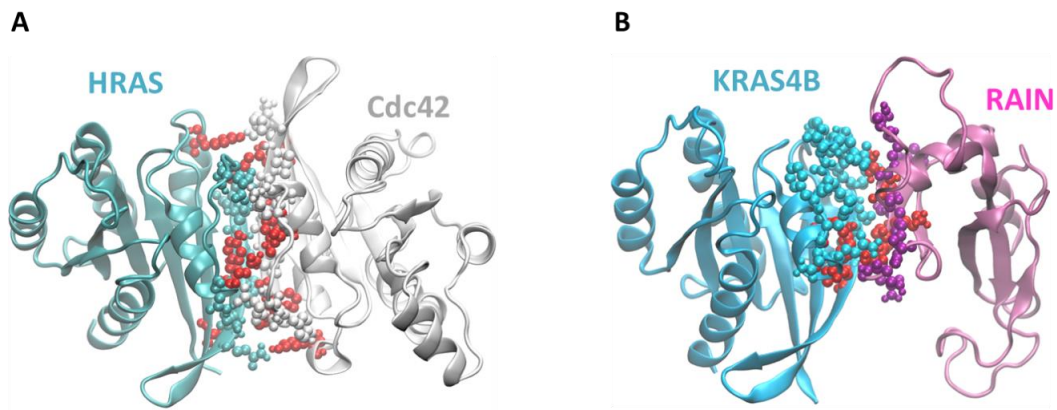


Figure 5.3. **A)** Predicted complex structure of H-Ras (PDB ID: 1QRA) and cell division control protein 42 homolog (Cdc42) (PDB ID: 2NGR). **B)** Predicted complex structure of K-Ras4B (PDB ID: 3GFT) and Ras associating (RA) domain of Ras interacting protein 1 (RAIN, Model). Interface residues are displayed as CPK balls and labeled in the color of the corresponding chain. Hotspots are shown in red balls.

Multiple sequence alignment of Ras isoforms indicate that conserved residues in protein-protein interfaces correlate with residue hot-spots (Figure 5.4).

is constitutively activated by mutations, calmodulin can act to accomplish the full activation of the PI3K/Akt pathway role. Thus, by activating the PI3K α /Akt pathway in the absence of a growth signal calmodulin may play a critical role in adenocarcinomas, particularly pancreatic cancer. The high calcium levels observed in adenocarcinomas may explain calmodulin's involvement in recruiting and activating PI3K α through interaction with its n/cSH2 (N- and C- terminal SH2) domains as well as K-Ras, and why K-Ras4B specifically is a key player in these cancers.

Experiments with K-Ras4B-negative fibroblasts indicate that Akt growth factor-dependent cell migration and activation requires K-Ras4B. The inability of K-Ras4A or oncogenic N-Ras to restore K-Ras4B function in these cells suggests the involvement of a unique binding partner [133, 227]. Cells treated with CaM antagonists phenocopied the biological outcomes of K-Ras4B-negative cells, failed to activate Akt and induce migratory response through matrix metalloproteinase 2 (MMP-2) expression. MMP-2 is involved in the breakdown of type IV collagen and induces cell detachment, migration, and metastasis of invasive tumors. MMP-2 levels are elevated in breast, brain, ovarian, pancreas, colorectal, bladder, prostate and lung cancers and melanoma [228]. Treating cells with PI3K or Akt inhibitors confirmed that the transcriptional activity of the *MMP-2* gene is specifically controlled by K-Ras4B through a PI3K/Akt-dependent signaling pathway [135]. Taken together, these results indicate that the K-Ras4B/CaM complex along with Ca²⁺ is the driving force behind growth factor-dependent Akt activation and that the PI3K/Akt pathway is essential for migratory activity. The fact that the K-Ras4B/calmodulin complex and PI3K are involved in Akt activation and the observation that calmodulin can directly activate PI3K [133], support the notion of a ternary complex between K-Ras4B, calmodulin, and PI3K α suggested by Liao and colleagues [134], albeit not necessarily with p110. Exploiting the PRISM [183-185], we modeled the binary interactions of PI3K p110 α catalytic subunit with GTP-loaded K-Ras4B, and the Ca²⁺/calmodulin interaction with the PI3K p85 α cSH2 domain, in agreement with the earlier indications from Joyal and colleagues experiments [133]. A possible model of a ternary complex between K-Ras4B, calmodulin, and PI3K p110/p85 is shown in Figure 5.5 [139]. Calmodulin's binding to the cSH2 and nSH2

domains of p85 are more stable than to p110 and is in line with PI3K activation scenario [229], as detailed below. While the model may not reflect accurately the interaction details, it nevertheless not only supports the idea of ternary complex formation, but also indicates that calmodulin may indeed have a key function in Akt activation.

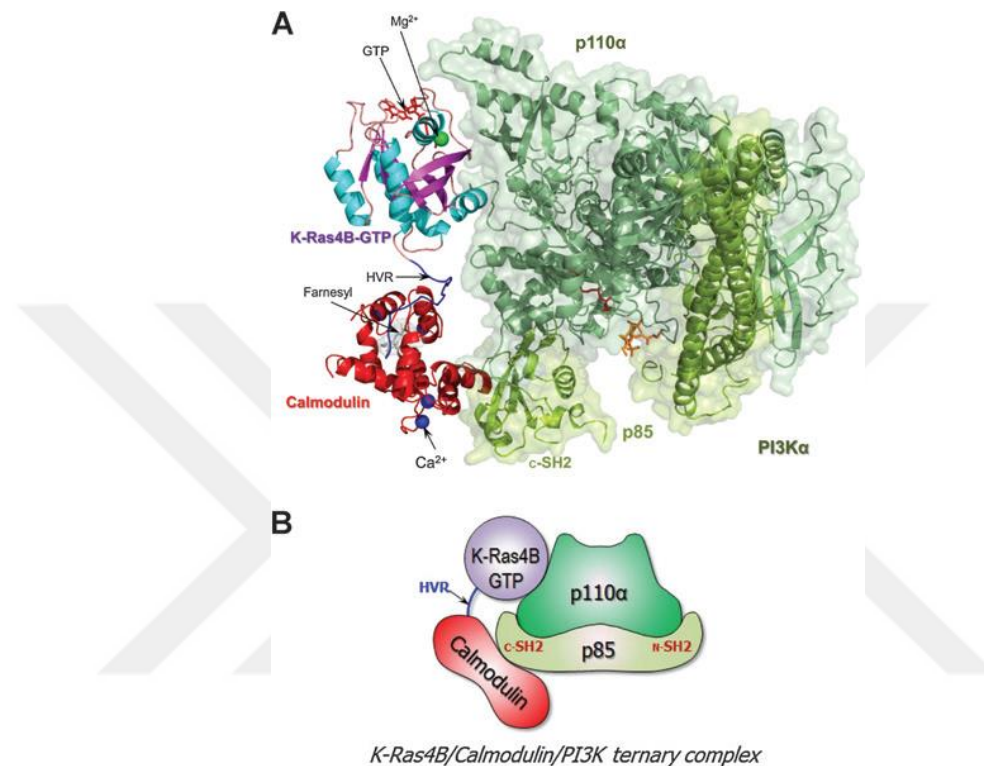


Figure 5.5. A K-Ras4B-GTP/calmodulin/PI3K ternary complex model based on the prediction [139]. We used the G-domain of K-Ras (166 residues), full-length calmodulin (149 residues), and the p110 catalytic p85 regulatory subunits of PI3K as target proteins. Full-length calmodulin has about 75 structures in the PDB. We considered only X-ray structures with $<3.00 \text{ \AA}$ resolution. In this way, we reduced the number of calmodulin structures to 43 with 71 chains in total. PI3K p110 catalytic domain has 4 isoforms, p110a, p110b, p110g, and p110d. We used the p110a and p110g structures in the PDB. We predicted models for the binary interactions between K-Ras and PI3K, and calmodulin and PI3K. We identified the contact regions using HotRegion [188]. Then, we built a model for the ternary complex based on the binary interactions and available literature data. A, the detailed structure; B, a simplified cartoon rendering for clarity.

Activated Ras can directly bind p110 and activate PI3K; however, the dissociation constant, K_d , for the Ras–PI3K complex is higher than the K_d for the Ras–Raf RBD complex (K_d : 160 nmol/L) [112, 230] and the Ras-Ral guanine nucleotide dissociation stimulator (RalGDS) RBD complex (K_d : 1 mmol/L) [231] indicating that the Ras-binding domain of PI3K p110 has a relatively lower affinity for Ras. This suggests a significant role for calmodulin in ternary complex formation and PI3K activation. Calmodulin binding might allosterically induce a conformational change in the RBD of PI3K in a way that cooperatively increases the affinity of K-Ras for PI3K, extending the duration of PI3K/Akt signaling. The low binding affinity of p110/K-Ras4B and the catalytic enhancement (8- to 10-fold) of p110 by GTP-bound K-Ras [121] highlight the importance of membrane localization of p110a via p85 nSH2 domain binding to the phosphorylated tyrosine of RTKs (or GPCR or cytokine receptors for p110g) or their associated adaptor proteins.

Coimmunoprecipitation and affinity chromatography suggested that CaM/Ca²⁺ binds p85; this was further affirmed by CGS9343B, a calmodulin antagonist that inhibited basal and Ca²⁺-stimulated phosphorylation of phosphatidylinositol in intact cells [133]. While no direct affinity measurements are available, we expect that CaM/Ca²⁺ bind to the cSH2-p85 with much higher affinity than to the nSH2-p85. The phosphorylated insulin receptor substrate-1 (IRS-1) peptide KKHTDDGYMPMSPGVA (residues 605–615) with the pYXXM motif can disrupt the cSH2/CaM/Ca²⁺ binding. CaM stimulates PI3K α phosphorylation of phosphatidylinositol (PtdIns) to PtdIns-3-P or PtdIns-4-P; but not PtdIns-4,5-P₂ to PtdIns-3,4,5-P₃. In the Joyal *et al.* experiment, a concentration of 2 and 5 μ M CaM with 100 μ M Ca²⁺ in a Chinese hamster ovary cell line showed only 10% and 50%, respectively, stimulation of PI3K activity [133]. These data imply that CaM might only have a high μ M affinity to cSH2. The interaction of CaM with PI3K α 's nSH2 and cSH2 domains were modeled, and the CaM/cSH2 interaction was simulated. The stability of CaM/Ca²⁺/cSH2 interaction was tested with flexible and stiff linker; both bound CaM states are stable throughout the simulation (unpublished observation).

Chapter 6

PDE δ BINDING TO RAS ISOFORMS**6.1. The Interaction of the Catalytic Domain of K-Ras4B-GTP with PDE δ**

We carried out standard Rosetta [232, 233] global docking to build putative models for the K-Ras4B catalytic domain interacting with PDE δ . We selected the top four models from the prediction for further evaluation (Figure B.7). Since the interaction of K-Ras4B with PDE δ is mediated mainly through the contacts between the HVR/farnesyl group and the prenyl binding pocket, we investigated whether the orientation of the catalytic domain with respect to PDE δ in the selected models allows the penetration of the farnesyl group into the prenyl binding pocket. However, none of the models are compatible with this scenario, since the predicted models are almost identical. The models show that the K-Ras4B catalytic domain locates at the opposite side of the gate of prenyl binding pocket. The distance between the C-terminus of the K-Ras4B catalytic domain and the PDE δ prenyl binding pocket is larger than the length of the HVR. The catalytic domain and the PDE δ are away from each other in the initial structures, suggesting that the interaction between these two proteins occurs only through the prenylated C-terminus [97].

6.2. The Interaction of the Prenylated K-Ras4B-GTP with PDE δ .

I carried out 300 ns MD simulations on the six systems described in the Methods section to analyze the interactions between the prenylated K-Ras4B-GTP and PDE δ hydrophobic pocket in detail. During the simulations, no immediate dissociation of the prenyl groups of K-Ras4B-GTP from the hydrophobic pocket of PDE δ was observed (Figure B.7). The K-Ras4B-GTP/PDE δ complex was highly preserved, although there are large fluctuations between these two proteins connected by the HVR (Figure 6.1). The fluctuations are eminent when we superimposed the systems with respect to the K-Ras4B catalytic domain (Figure B.9). To monitor and compare the stability of the systems, the root-mean-squared deviations (RMSDs) with respect to the initial structures of the six K-Ras4B/PDE δ systems were calculated (Figure B.10 and Table A.11). As expected, K-Ras4B has a larger RMSD than PDE δ due to the HVR. The results also suggest that the

averaged RMSDs of the complexes of systems 4 and 6 are smaller than for the other four systems. The center of mass distance between K-Ras4B and PDE δ was also computed (Figure B.11). The results indicate that unlike the other systems, the distance between the two proteins remain larger in System 1 (where the farnesylated HVR is a flexible loop and Phe133 is flipped downward) and lower in Systems 4 (where the farnesylated HVR is partially folded into a α -helix and Phe133 is flipped upward) and 6 (where the geranyl-geranylated HVR is partially folded into a α -helix and Phe133 is flipped downward), which explain why System 1 has the least and Systems 4 and 6 have the best binding energies. The dynamics of both the catalytic domain and PDE δ show a rigid body motion with respect to each other, which is supported by the flexible HVR. The fluctuations of the prenyl groups cause a conformational rearrangement of the β -sandwiched pocket in PDE δ . For Systems 1, 2, 5, and 6, the conformational transition of PDE δ from state 1 to 2 can be observed. PDE δ shifts the equilibrium toward the Phe133 aromatic ring flipping upward, suggesting that both farnesyl and geranylgeranyl favor the upward state of the aromatic ring. However, System 3 shows the transition from state 2 to 1 during the simulations, indicating that interconversion between the states of the Phe133 sidechain is possible, depending on the dynamics of the prenyl groups. Pseudo-helical conformation of the HVR in KM2 (where the HVR is partially folded into a α -helix) gradually unfolds to the chain conformation, suggesting that the HVR is intrinsically disordered [234].

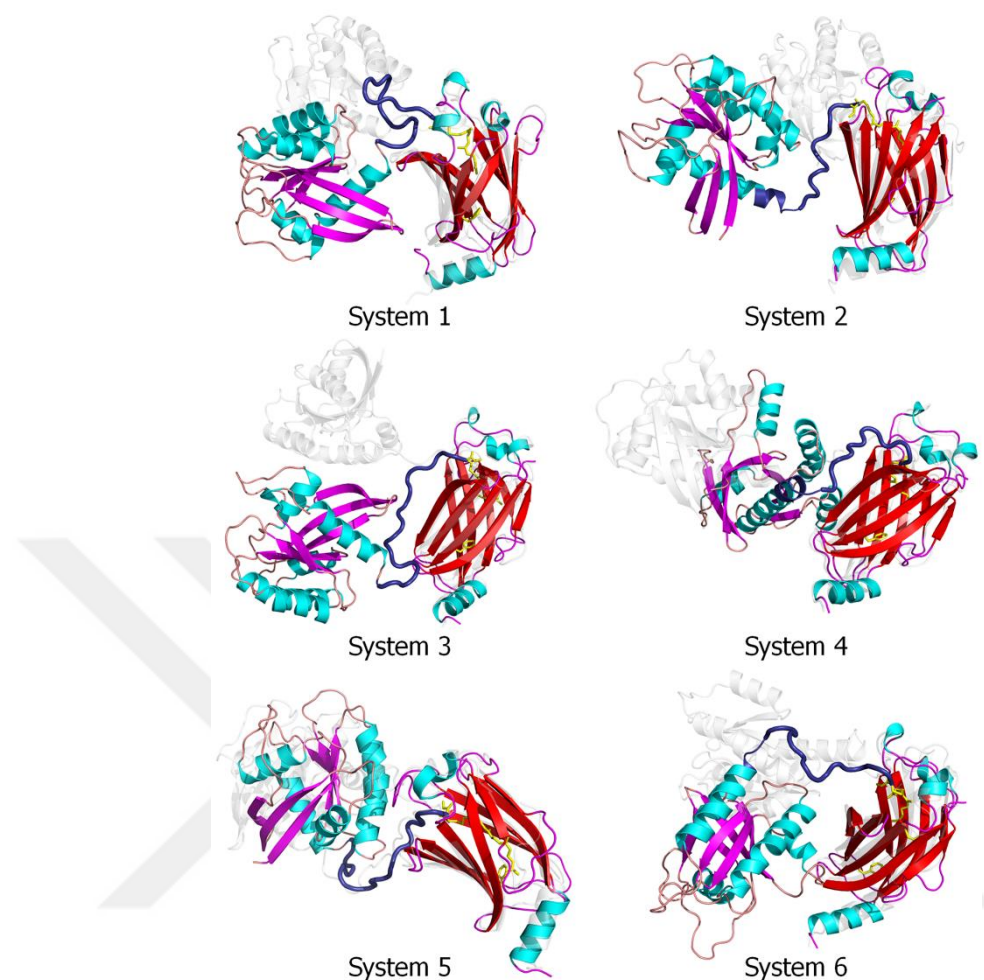


Figure 6.1. The superimposed snapshots of the final conformation (colored cartoon) and the starting point (white transparent cartoon) of these six K-Ras4B-GTP/PDE δ systems (System 1 – System 6). All coordinates were reoriented with respect to the PDE δ coordinates.

The major interaction of K-Ras4B with PDE δ derives from the HVR. In contrast, the catalytic domain interaction is transient, marginally contacting the PDE δ in some system configurations. To corroborate the K-Ras4B interaction with PDE δ , we analyzed key residues involved in dimer formation (Figure 6.2 and Table A.12). The results indicate that the anchor HVR residues, Lys182, Thr183, and Lys184 play a significant role in PDE δ binding. They form hydrogen bonds (H-bonds) and salt bridges with Glu88 from PDE δ . In addition, the linker HVR residues, Lys169, Lys172, and Lys177 also participate in K-Ras4B/PDE δ association. Lys169 forms a salt bridge with Glu93 from PDE δ . Lys172 forms multiple H-bonds and salt bridges with residues Asp136 and Asp137.

Lys177 forms a H-bond and a salt bridge with Glu89. In particular, Ser181 makes stronger associations with Glu88 in geranylgeranylated systems via main and sidechain oxygen atoms. Comparison of the interacting residues between the farnesylated and geranylgeranylated systems also suggests that the catalytic domain of geranylgeranylated K-Ras4B forms some interactions with PDE δ . The catalytic domain residues, Arg73 and Asp69 on the α 2 helix form H-bonds with Glu77 and Lys79 from PDE δ , respectively. However, no catalytic domain interaction with PDE δ was observed in the farnesylated systems, suggesting that the interactions between the catalytic domain of farnesylated K-Ras4B and PDE δ are highly transient.

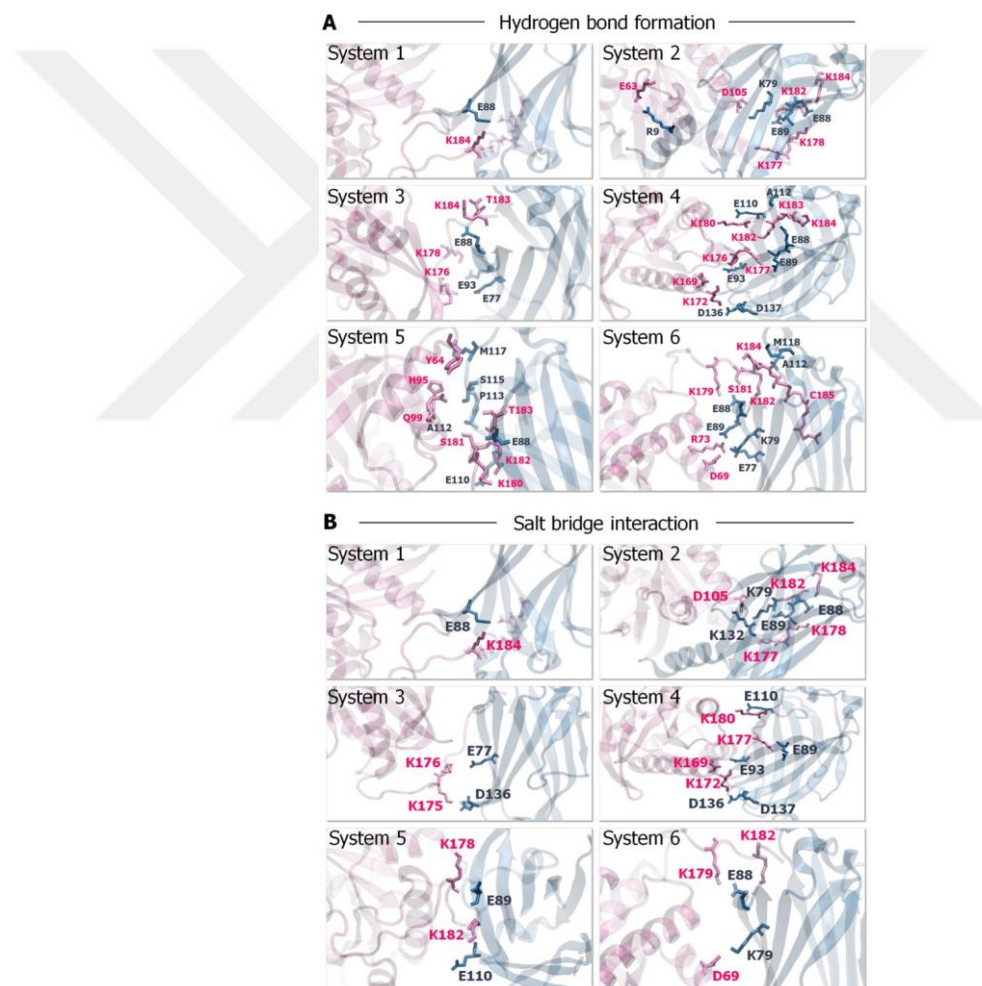


Figure 6.2. The key residues involved in K-Ras4B-GTP/PDE δ complex formation. (A) The prominent hydrogen bonds and (B) salt bridges formed between K-Ras4B and PDE δ during the simulations. The residues involved in hydrogen bonding are represented as ball-and-stick with parental colors.

At the starting point of farnesylated systems with PDE δ in state 1, the farnesyl group inserted deeply into the pocket. Subsequently, a couple of the HVR backbone residues initially slipped into the hydrophobic cavity. However, during the simulations the HVR residues bounced from the pocket due to unfavorable interactions taking place at the gate of the pocket. As a result, PDE δ allowed the farnesyl to reside in the shallow region of the cavity. In the pocket, the farnesyl favors hydrophobic interactions with Trp32, Ile53, Val59, Leu87, and Val145 from PDE δ (Figure 6.3A). At the starting point of the farnesylated systems with PDE δ in state 2, the farnesyl group inserted shallowly into the pocket. The shallow farnesyl insertion was favorable for PDE δ , which provides many hydrophobic residues, Met20, Leu22, Trp32, Leu38, Ile53, Trp90, Ile109, Phe133, and Leu147, to interact with the farnesyl moiety (Figure 6.3B). Evidently, the farnesyl group makes more contacts with the PDE δ hydrophobic pocket. The geranylgeranylated systems have only PDE δ in state 1 due to the longer hydrocarbon chain. In the pocket, geranylgeranyl favors the hydrophobic interactions with Trp32, Leu38, Val59, Ala111, Phe133, Val145, and Leu147 from PDE δ (Figure 6.3C).

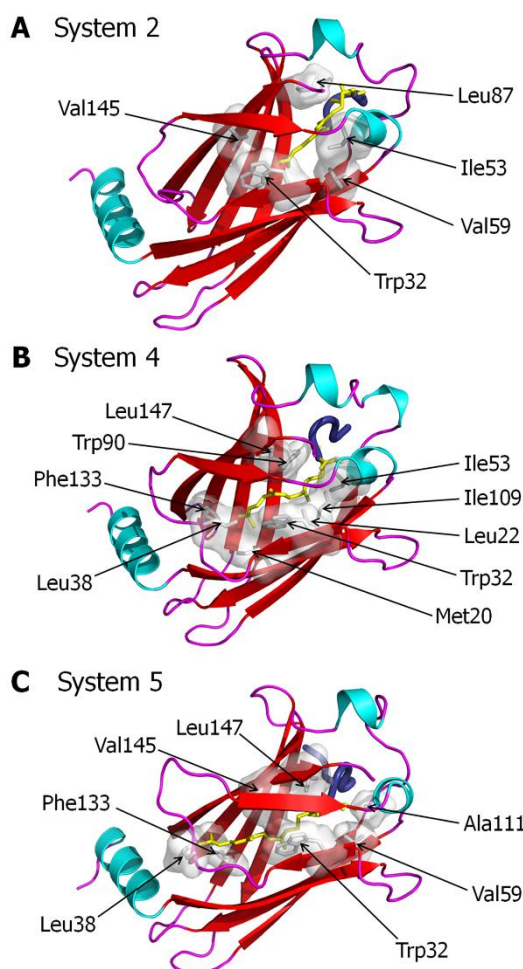


Figure 6.3. Hydrophobic interactions involved in K-Ras4B-GTP/PDE δ complex formation. PDE δ residues that participate in hydrophobic interactions with K-Ras4B prenyl group for (A) System 2, (B) System 4, and (C) System 5.

Comparison of the crystal with the simulated states, indicates that the long helix observed in state 2 in the crystal structure becomes partially disordered; in state 1 about a third of the helix becomes disordered as well. Inspection of the crystal lattice indicates that the disordered part of the helix in form 1 (state 1) is stabilized by crystal packing in form 2 (state 2).

6.3. Binding Energy in Dimer Formation

To quantify the six K-Ras4B-GTP/PDE δ complex systems, we calculated the binding energy, ΔG_b , using the MM/GBSA method (Table 6.1). With an entropic contribution, the binding energy is directly related to the binding free energy of dimer formation. For

the farnesylated systems, shallowly inserted configurations yield stronger binding for the K-Ras4B-GTP/PDE δ complex, which suggests that the farnesyl interaction in the pocket is significant for high affinity binding. For the geranylgeranylated systems, the binding energies are comparable to those of the farnesylated systems. Overall, the binding energy results suggest that PDE δ can transport the K-Ras4B protein, whether it is modified with farnesyl or geranylgeranyl. In general, prenylated K-Ras4B interacts more strongly with the PDE δ hydrophobic pocket when the HVR is folded, since under these circumstances additional catalytic domain interactions with PDE δ partially contribute to the binding energy as well. We expect that the simulation times were not long enough to achieve comparable energies for the two minima (Systems 1 and 2 versus 3 and 4).

Table 6.1. Binding energy in dimer formation using MM/GBSA method for the prenylated K-Ras4B-GTP/PDE δ systems.

K-Ras4B/PDEδ	$\langle \Delta G_{gas} \rangle$ (kcal/mol)	$\langle \Delta G_{sol} \rangle$ (kcal/mol)	$\langle \Delta G_b \rangle$ (kcal/mol)
System 1	-411.3 \pm 162.0	368.8 \pm 158.6	-42.5 \pm 8.5
System 2	-694.5 \pm 235.4	635.4 \pm 217.0	-59.2 \pm 23.6
System 3	-769.5 \pm 266.0	705.2 \pm 247.8	-64.2 \pm 21.2
System 4	-820.6 \pm 96.4	736.7 \pm 86.0	-83.9 \pm 13.3
System 5	-621.4 \pm 74.9	548.5 \pm 68.3	-71.9 \pm 11.0
System 6	-570.9 \pm 112.4	487.9 \pm 105.8	-83.0 \pm 17.2

6.4. The Interactions of Farnesylated HVRs of K-Ras4A, K-Ras4B, and N-Ras with PDE δ

We carried out 200 ns MD simulations on the HVR/PDE δ systems described in the Methods section to investigate the isoform-specific interactions between the farnesylated HVR peptides and the PDE δ hydrophobic pocket. During the simulations, even without the catalytic domain, no immediate dissociation of the HVR peptide from PDE δ was

observed (Figure 6.4). The HVR/PDE δ complex was highly preserved for all farnesylated Ras isoforms, supporting the observation that the catalytic domain interaction with PDE δ is transient. Similar to the K-Ras4B-GTP/PDE δ systems, for all HVR/PDE δ systems including K-Ras4A and N-Ras, the conformational transition of PDE δ from state 1 to 2 with the Phe133 aromatic ring flipping upward can also be observed, verifying that the farnesyl favors the upward state of the aromatic ring of PDE δ .

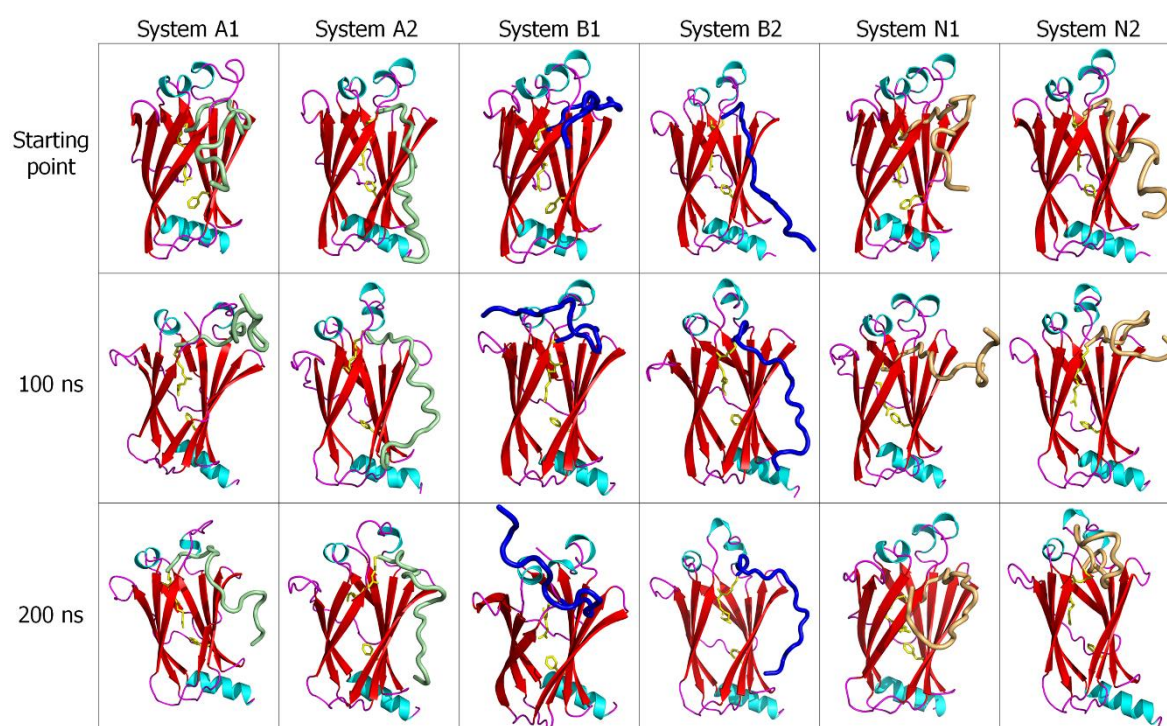


Figure 6.4. The snapshots of farnesylated HVR/PDE δ complex for K-Ras4A (System A1 & A2), K-Ras4B (System B1 & B2), and N-Ras (System N1 & N2) at the start point, 100 ns, and 200 ns points. In the cartoon, green, blue, and orange tubes represent the K-Ras4A, K-Ras4B, and N-Ras HVRs, respectively.

To identify the key binding residues in the HVR/PDE δ complex, we performed a detailed interface analysis. Since the K-Ras4B HVR interactions with PDE δ are similar to those defined for the K-Ras4B-GTP/PDE δ complexes, we closely monitored the atomic pair interactions of the HVRs of both K-Ras4A and N-Ras with PDE δ (Figure 6.5 and Table A.13). We observed that the residues at the anchor region of K-Ras4A HVR, Lys182, Lys184, and Lys185 are important for PDE δ binding. They form H-bonds and salt

bridges with Glu88 from PDE δ via main and side-chain oxygen atoms. For the N-Ras HVR/PDE δ complex, we observed that the anchor residues of N-Ras HVR, Cys181, Met182, and Gly183 interact with Glu88, and Glu110 from PDE δ via H-bonds and salt bridges. For both K-Ras4A and N-Ras, the linker residue Arg167 at the HVR commonly participates in the HVR/PDE δ association, suggesting that the linker interaction occurs due to the peptide effect, in the absence of the catalytic domain. Compared to K-Ras4A and K-Ras4B, the N-Ras HVRs do not form a salt bridge with PDE δ , since the anchor region of the N-Ras HVR is electrostatically neutral. Overall, the residue Glu88 on the β 6 of PDE δ constitutes the most important residue in the interactions of both farnesylated K-Ras4A and N-Ras HVRs with PDE δ [234].

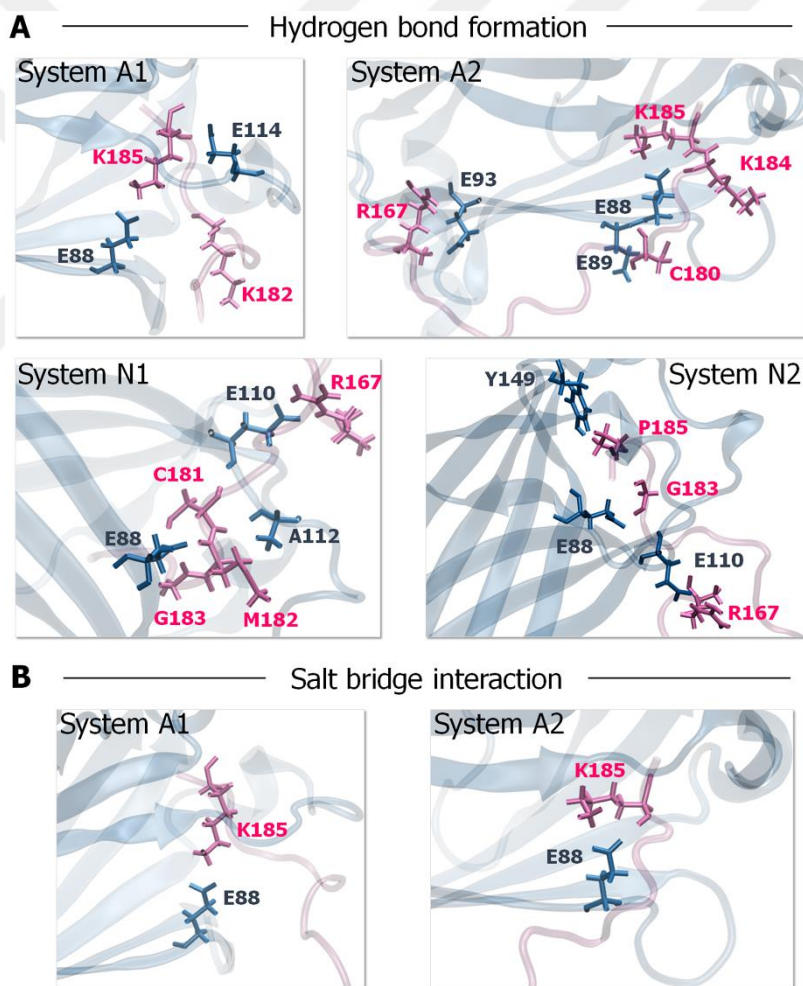


Figure 6.5. The key residues involved in HVR/PDE δ complex formation. **(A)** The prominent hydrogen bonds and **(B)** salt bridges formed between the farnesylated HVR and PDE δ during the simulations. The residues involved in hydrogen bonding are represented as ball-and-stick with parental colors.

A detailed analysis of the resulting structures reveals that the stabilizing interactions of the farnesyl with the hydrophobic residues in the pocket of PDE δ support the conformation of the HVR/PDE δ complex. In System A1, the farnesyl favors the hydrophobic interactions with Met20, Trp32, Leu38, Val49, Val59, Ile109, and Ile129 from PDE δ (Figure 6.6A). In System A2, the farnesyl favors the hydrophobic interactions with Trp32, Ala47, and Met117 from PDE δ (Figure 6.6B). For the K-Ras4A HVR/PDE δ complex, the deep farnesyl insertion results in increased contacts between the farnesyl and PDE δ . In contrast, for the N-Ras HVR/PDE δ complex, there are more hydrophobic contacts of the farnesyl with PDE δ when the farnesyl inserted shallowly into the pocket. This is most likely to compensate for the lack of hydrogen bonds and salt bridges. In System N1, the farnesyl favors the hydrophobic interactions with Trp32 and Trp90 from PDE δ (Figure 6.6C). In System N2, the farnesyl favors the hydrophobic interactions with Met20, Trp32, Leu63, Ile109, Ala111, Val145, and Leu147 from PDE δ (Figure 6.6D). While the catalytic domains were not included in these simulations, we expect that their fluctuations would weaken the associations – both in K-Ras4A and N-Ras.

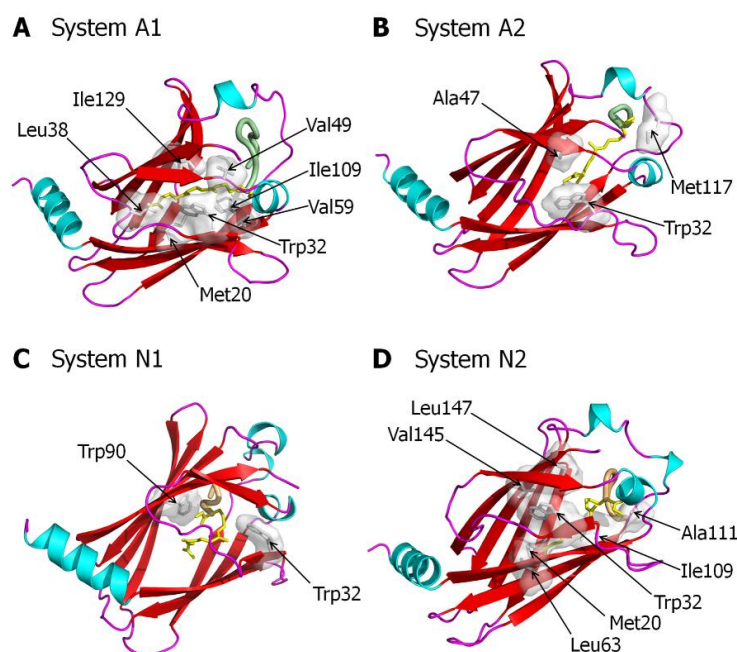


Figure 6.6. Hydrophobic interactions involved in HVR/PDE δ complex formation. PDE δ residues that participate in hydrophobic interactions with the farnesylated HVR for (A) System A1, (B) System A2, (C) System N1, and (D) System N2.

6.5. Discussion

Over the years, numerous attempts have been made to pharmacologically inhibit oncogenic Ras. Despite intensive efforts, Ras is still widely considered as “undruggable”. The prenyl binding protein PDE δ has been shown to augment (oncogenic) Ras signaling by enriching Ras at the PM.[89, 98, 99] Ras localization at the PM profoundly influences its activation and signaling capacity. This localization increases its effective local concentration through dimerization[158, 206, 235] and nanocluster formation,[58, 78, 79] as well as acts in signaling selectivity of Ras isoforms.[167, 195-197, 236-239] Importantly, it also locates Ras in the vicinity of receptors that receive the signaling cues, such as EGFR, its nucleotide exchange factors, and membrane-recruited kinase effectors,[157] such as Raf and PI3K, and non-kinase effectors, such as RASSF5, which links Ras with the MST1/2 kinase and the Hippo pathway.[240, 241] Therefore, interfering with Ras localization by inhibiting its interaction with PDE δ can be an alternative approach to target oncogenic Ras.[242] Here, we simulated six full-length prenylated K-Ras4B-GTP/PDE δ complex systems and six prenylated HVR/PDE δ systems. Structural analysis of snapshots of the interfaces of K-Ras4B-GTP/PDE δ reveals a remarkable similarity to the recently solved crystal structures as well as their behavior in solution.[97] Our results indicate that the HVR/prenyl moiety of K-Ras4B is responsible for the interaction with PDE δ and the “SKTK” motif plays a significant role in PDE δ binding. They further suggest that glutamate residues at positions 88, 89, 110, 136, and 137 are the key binding residues of PDE δ . The conserved aspartates 136 and 137 are also involved in the interaction of RhoGDI and Cdc42. They help stabilizing the interaction of the N-terminal helix–loop–helix region of RhoGDI and the switch II domain of Cdc42.[101] Thus, the electrostatically-negative surface of PDE δ plays an important role in the interaction with the positively charged K-Ras4B HVR. They also point to two dynamic states.

Comparison of the interfaces of farnesylated and geranylgeranylated systems reveals that a few residues on the catalytic domain of geranylgeranylated but not farnesylated K-Ras4B interact with PDE δ . Our results are in accordance with the previous findings showing that the interaction between the catalytic domain of farnesylated K-Ras4B and PDE δ is very weak and transient.[97, 99] The absence of any specific interaction between

the catalytic domain and PDE δ makes this association nucleotide-independent. MM/GBSA calculations of the full-length prenylated K-Ras-4B-GTP/PDE δ systems indicate that the interaction between farnesylated K-Ras4B and PDE δ is stronger when the farnesyl inserts properly into the pocket. To understand the contribution of the catalytic domain, if any, to the binding, we also studied the prenylated K-Ras4B HVR/PDE δ systems. The results corroborate other studies, pointing out that the HVR and the prenyl moiety are the main players of PDE δ binding.[97, 99] Overall, the simulations indicate that factors such as the prenylation status and the HVR conformation affect the K-Ras4B/PDE δ interaction, and that K-Ras4B has the highest affinity for PDE δ when it is farnesylated.

Experimental data were taken to imply that PDE δ binds to K-Ras4B and to N-Ras;[98] but not to *K-Ras4A*, a splice variant of K-Ras4B.[92] K-Ras4B is only farnesylated; K-Ras4A and N-Ras are farnesylated and palmitoylated – however, palmitoylation is reversible. Sequence-wise, the HVR of K-Ras4A is very similar to that of K-Ras4B, with both being highly positively charged; on the other hand, the anchor region of the N-Ras HVR is electrostatically neutral. With respect to the catalytic domain, the K-Ras isoforms are highly similar: K-Ras4A differs from K-Ras4B by only four residues. This raises the significant question of how to resolve these apparently puzzling experimental observations.

Oncogenic K-Ras4A was observed to be involved in K-Ras4B colorectal cancer, which is a K-Ras4B cancer, in addition to involvement in N-Ras cancer, such as melanoma, which led us to propose that K-Ras4A can exist in two states, depalmitoylated K-Ras4B-like, which we called state 1, and palmitoylated N-Ras-like, which we called state 2.[196, 243] Thus, to address the question of why K-Ras4B and in particular also N-Ras were observed to bind to PDE δ but apparently not K-Ras4A, we simulated PDE δ with the HVRS of K-Ras4A and N-Ras isoforms. We observed that even though steric clashes appear to exist with the two K-Ras4A lysines located upstream of the farnesylated Cys, conformational dynamics can accommodate these, to permit the interaction of a depalmitoylated K-Ras4A molecule with PDE δ . This was not surprising as along similar lines, calmodulin, which has been suggested to be K-Ras4B-specific, appears to also

interact with depalmitoylated K-Ras4A.[139, 244] Moreover, the proposition that depalmitoylated K-Ras4A can interact with PDE δ is supported by experimental N-Ras observations. Co-expression of N-Ras and PDE δ showed that a marked fraction of N-Ras in the cytoplasm interacts with the PDE δ . Comparison of the level of palmitoylation indicated that at least half of the N-Ras molecules were depalmitoylated at the steady state. We observe that the interaction of K-Ras4A with PDE δ is comparable to that of N-Ras. Further in line with this, H-Ras (with a farnesyl and two palmitoyls) experiments pointed to less than a quarter of the molecules at the steady state.[98] This led the authors to conclude that a substantial fraction of N-Ras is already depalmitoylated when it reaches the PM through the secretory pathway and the relative palmitoylation level (H-Ras > N-Ras) determines the PDE δ binding tendencies of Ras isoforms.

To explain why PDE δ can extract from the PM K-Ras4B and N-Ras but not K-Ras4A,[92] it was proposed that Ras family proteins that bind to PDE δ avoid large/charge residues adjacent to the prenylated site. However, our conformational dynamics indicate that the disordered fluctuating K-Ras4A HVR can accommodate the two adjacent lysine residues and bind PDE δ . Here we argue that PDE δ can bind to all farnesylated but non-palmitoylated Ras isoforms, with affinities that may reflect the electrostatic properties of the HVR and the adjacent residues. A key factor in understanding why K-Ras4B and N-Ras are extracted from the PM by PDE δ but not K-Ras4A is the relative stabilities of the interactions with the PM versus in solution with PDE δ . The stabilities of the interactions with PDE δ of the electrostatically neutral N-Ras and the electrostatically positively-charged K-Ras4A – but with an apparent steric hindrance that needs to be accommodated – are similar; however, that is not the case with respect to the PM. There, K-Ras4A and H-Ras are more stably lodged. This emphasizes the need to consider both environments when seeking to understand physical observations. The Tsai *et al.* experiment [92] considered extraction from the membrane; not direct PDE δ binding in solution. The consideration of steric hindrance based on the crystal and our modeling and simulations are in solution – and do not consider the competing PM interactions. Thus, PDE δ can shuttle isoforms that have farnesyl (but not palmitoyl), positively-charged HVR and preferentially lack bulky residues adjacent to the prenylated sites which could weaken the interaction, even though these can be accommodated.

The implications of our observations are significant. In a recent remarkable paper, Schmick *et al.*[89] posited that PDE δ acts to counteract an otherwise entropy-driven localization of Ras isoforms in endomembranes. The large total surface area that they present would result in randomized Ras distributions. PDE δ solubilizes the Ras molecules and shuttles Ras to the PM opposing the inward cytoplasmic flow driven by endocytosis. Schmick *et al.* argued that cytosolic PDE δ s constantly sequester mislocalized K-Ras from endomembranes, shuttling it to the recycling endosome, where it is trapped, and subsequently vesicle-transported to restore its enrichment on the PM. Here we show that in principle, all Ras isoforms can be shuttled. This emphasizes the potential of small molecules interfering with this action. The conformational details of the two states provided here may help in this venture.

Chapter 7

CONCLUSION

The main focuses of this dissertation are to predict Ras homodimer and Ras/effector complex structures, validate Ras dimerization *in vivo*, and investigate the significance of oligomerization/nanoclustering on Ras signaling. It also explains how K-Ras4B is shuttled to the PM by PDE δ , and discusses the implications of Ras/PDE δ interaction for other Ras isoforms.

Ras dimerization and higher oligomerization states were long believed to increase signaling output and facilitate interactions with effectors, such as Raf [2, 114]. However, dimerization was not observed in soluble Ras leading to an assumption that interfaces observed in crystals were due to crystal packing interactions. Dynamic light scattering studies have unexpectedly revealed GTP-dependent dimerization of K-Ras G-domain, which was further confirmed by other experimental studies and computational analysis [206]. Computational tools help enrich the available structural data for PPIs and analyze the effects of mutations on the interactions. Application of a powerful structural prediction algorithm, PRISM, I confirmed high affinity homodimer formation for K-Ras4B-GTP through two dimer interfaces: helical and beta interfaces, but only low affinity dimerization for K-Ras4B-GDP. A survey of Ras crystal structures showed that while the functional state of Ras has been identified as a monomer, its predicted membrane-anchored dimeric interface is among its crystal packing interactions. To validate the predicted interfaces, I performed site-directed mutagenesis and investigated their effects on ERK phosphorylation. Two double mutations (K101D/R102E and R41E/K42D) presented promising results in the preliminary results. However, western blot analysis indicated that these mutations decrease the Ras concentration in the cell, thus reduce Ras clustering and ERK phosphorylation. R41E/K42D, on the other hand, decreases pERK levels even when the results are normalized with respect to Ras levels. Looking at its position (located on the beta-interface), it, most probably, interferes with Raf binding.

Ras interacts with many proteins, thus regulate a wide variety of cellular functions. However, for only a few of the Ras/effector complexes the crystal structures are available in PDB. I modeled the interactions of H- and K-Ras4B with their effector proteins using PRISM. The results indicate that most of the effectors bind to the effector binding region that involves the β -sheet extension on Ras, thus competes with Ras dimerization through beta interface. However, a few of them binds to the allosteric region that involves the helices 3, 4 and 5 on Ras suggesting a new role for this region.

Ras relays the signal when it is membrane-attached. Thus, it needs to be shuttled to the PM following the synthesis and PTMs. PDE δ is responsible for the shuttling of K-Ras4B. Studies indicate that PDE δ can bind to K-Ras4B, and N-Ras, but not to K-Ras4A. To study Ras/PDE δ interaction, and elucidate the differences among the isoforms, I performed explicit-solvent MD simulations of K-Ras4B/PDE δ and the HVRs of N-Ras and K-Ras4A with PDE δ . The results indicate that PDE δ can interact with depalmitoylated K-Ras4A, as well as K-Ras4B and depalmitoylated N-Ras, albeit with different affinities [234]. The results further emphasize the importance of considering and comparing the interactions in the respective environments. The crystal structures and the K-Ras4B simulations underscore PDE δ evolution to preexist in two major states, which can accept farnesyl and geranylgeranyl. These two minima are critical in permitting enrichment of Ras family GTPases at the plasma membrane, which is required for Ras to fulfil its function. This work emphasizes the notion that fundamental concepts from physical chemistry and chemical physics dominate the structure-function paradigm.[245] Here, I elucidate the K-Ras4A behavior, and explain that PDE δ binding to farnesylated Ras family proteins can provide a route to proper membrane localization [89].

APPENDIX A

Table A.1. Oligonucleotide primers designed for Ras and Venus amplification

<u>KpnI</u> _VN173_cMyc_F	GATC <u>ggtacc</u> ATGGAACAAAACTCATCTCAGAAGAGGATCTGATGGT GAGCAAGGGCGAG
<u>BamHI</u> _VN173_Linkers_R	GATC <u>ggatcc</u> GGTGGCGATGGATCTCTCGATGTTGTGGCGGATCT
<u>EcoRI</u> _VC155_FLAG_F	GATC <u>gaattc</u> ATGGACTACAAAGACGATGACGACAAGGACAAGCAGAA GAACGGCATC
<u>BshTI</u> _VC155_Linkers_R	GATC <u>accggt</u> GTGGTTCATGACTTTCTGTTTCAGGTCGTTTCGGGATTTGCACG CCTTGACAGCTCGTCCATGC
<u>BamHI</u> _HRAS_F(VN173)	GATC <u>ggatcc</u> ATGACGGAATATAAGCTTGTTGTTGT
<u>NheI</u> _HRAS_R(VN173)	GATC <u>gctagc</u> TCAGGAGAGCACACACTTGC
<u>BshTI</u> _HRAS_F(VC155)	GATC <u>accggt</u> ATGACGGAATATAAGCTTGTTGTTGT
<u>NdeI</u> _HRAS_R(VC155)	GATC <u>catatg</u> TCAGGAGAGCACACACTTGC
<u>BamHI</u> _KRAS4b_F(VN173)	GATC <u>ggatcc</u> ATGACTGAATATAAACTTGTTGTTAGTTGG
<u>NheI</u> _KRAS4b_R(VN173)	GATC <u>gctagc</u> TTACATAATTACACACTTTGCTTTGACTTC
<u>BshTI</u> _KRAS4b_F(VC155)	GATC <u>accggt</u> ATGACTGAATATAAACTTGTTGTTAGTTGG
<u>NdeI</u> _KRAS4b_R(VC155)	GATC <u>catatg</u> TTACATAATTACACACTTTGCTTTGACTTC

Table A.2. SDM primers designed for the construction of constitutively active Ras mutants.

KRAS4b_G12D_F	GGTAGTTGGAGCTGACGGCGTAGGCAAGAG
KRAS4b_G12D_R	CTCTTGCCACGCGTCAGCTCCAACCTACC
HRAS_G12V_F	GTTGTTGGCGCCGTGGGTGTGGGCAAGAG
HRAS_G12V_R	CTCTTGCCACACCCACGGCGCCAACAAC

Table A.3. SDM primers for the construction of HRAS interface mutants.

<u>HRAS_S39A_Y40A_F1R2</u>	GAGGATGCCGCCCGGAAGCAGGTGGTCATTGATGG
<u>HRAS_S39A_Y40A_R1F2</u>	CCGGCGGCATCCTCTATAGTGGGGTCGATTCCG
<u>HRAS_R41A_K42A_F1R2_v2</u>	GGATTCCTACgcggcGCAGGTGGTCATTGATGG
<u>HRAS_R41A_K42A_R1F2_v2</u>	CTGcgccgcGTAGGAATCCTCTATAGTGGGGTCG
<u>HRAS_R41E_K42D_F1R2</u>	CCTACGAGGACCAGGTGGTCATTGATGGGGAGACG
<u>HRAS_R41E_K42D_R1F2</u>	CCACCTGGTCCTCGTAGGAATCCTCTATAGTGGGG
<u>HRAS_E98R_F1R2</u>	GTACAGGAGGCAGATCAAACGGGTGAAGGACTCGG
<u>HRAS_E98R_R1F2</u>	GATCTGTCCCCTGTAAGTGGTGGATGTCCTCAAAG

<u>HRAS K101A K102A F1R2</u>	GCAGATCGCAGCGGTGAAGGACTCGGATGACGTGC
<u>HRAS K101A K102A R1F2</u>	CCTTCACCGCTGCGATCTGCTCCCTGTAAGTGG
<u>HRAS K101E K102D F1R2</u>	GCAGATCGACGAGGTGAAGGACTCGGATGACGTGC
<u>HRAS K101E K102D R1F2</u>	CCTTCACCTCGTCTGATCTGCTCCCTGTAAGTGG

Table A.4. SDM primers for the construction of KRAS4B interface mutants.

<u>KRAS4b S39A Y40A F1R2</u>	GAGGATGCCGCCAGGAAGCAAGTAGTAATTGATGG
<u>KRAS4b S39A Y40A R1F2</u>	CCTGGCGGCATCCTCTATTGTTGGATCATATTCG
<u>KRAS4b R41A K42A F1R2</u>	CCTACGCGGCGCAAGTAGTAATTGATGGAGAAACC
<u>KRAS4b R41A K42A R1F2</u>	CTACTTGCGCCGCGTAGGAATCCTCTATTGTTGGATC
<u>KRAS4b R41E K42D F1R2</u>	CCTACGAGGACCAAGTAGTAATTGATGGAGAAACC
<u>KRAS4b R41E K42D R1F2</u>	CTACTTGGTCCTCGTAGGAATCCTCTATTGTTGGATC
<u>KRAS4b E98R F1R2</u>	CCATTATAGAAGACAAATTAAGAGTTAAGGACTC
<u>KRAS4b E98R R1F2</u>	CTCTTTAATTTGCTTCTATAATGGTGAATATCTTC
<u>KRAS4b K101A K102A F1R2</u>	CAAATTGCAGCAGTTAAGGACTCTGAAGATGTACC
<u>KRAS4b K101A K102A R1F2</u>	GTCCTTAACTGCTGCAATTTGTTCTCTATAATGGTGAATA TC
<u>KRAS4b K101E K102D F1R2</u>	CAAATTGACGAAGTTAAGGACTCTGAAGATGTACC
<u>KRAS4b K101E K102D R1F2</u>	GTCCTTAACTCGTCAATTTGTTCTCTATAATGGTGAATA TC

Table A.5. Types of atomic interactions in the GTP-bound K-Ras4B homodimer at the membrane. The atomic pair indicates the monomer1/monomer2 pair in the interface, represented in the order of ‘atom:residue:domain’. The number in the parenthesis denotes percentage of the atomic pair interaction based on the distance between the paired atoms [197].

	Salt bridge, M1/M2 pair	Hydrophilic interaction, M1/M2 pair
α-dimer	NH1:R97: α 3 / OE1:E98: α 3 (100) OE2:E98: α 3 / NH1:R97: α 3 (50) OE1:E98: α 3 / NZ:K101: α 3 (100) NZ:K101: α 3 / OE2:E98: α 3 (90) NH1:R102: α 3 / OD2:D105:L7 (90) NH1:R102: α 3 / OE1:E107:L7 (30) OE1:E107:L7 / NH1:R102: α 3 (80) OD2:D105:L7 / NH1:R73:SII (40) OD2:D105:L7 / NH2:R102: α 3 (50) NH1:R135: α 4 / OE1:E91: α 3 (90)	OH:Y137: α 4 / ND1:H94: α 3 (50) OH:Y137: α 4 / ND1:H95: α 3 (60)
	Salt bridge, M1/M2 pair	Hydrogen bond, M1/M2 pair
β-dimer	OD1:D33:SI / NZ:K42: β 2 (90) OE2:E37:SI / NH1:R41: β 2 (100) NZ:K42: β 2 / OD1:D33:SI (100)	O:E37:SI / N:R41: β 2 (100) N:S39: β 2 / O:S39: β 2 (100) O:S39: β 2 / N:S39: β 2 (100) N:R41: β 2 / O:E37:SI (60)

Table A.6. Types of atomic interactions in the GTP-bound H-Ras homodimer at the membrane. The atomic pair indicates the monomer1/monomer2 pair in the interface, represented in the order of ‘atom:residue:domain’. The number in the parenthesis denotes percentage of the atomic pair interaction based on the distance between the paired atoms [197].

	Salt bridge, M1/M2 pair	Cation-π interaction, M1/M2 pair
α-dimer	OE2:E91: α 3 / NH1:R128: α 4 (40) OE2:E62:SII / NH2:R135: α 4 (30)	OH:Y64:SII / NH2:R135: α 4 (20)
	Hydrogen bond, M1/M2 pair	Hydrophobic interaction, M1/M2 pair
β-dimer	N:S39: β 2 / O:S39: β 2 (90) O:S39: β 2 / N:S39: β 2 (80)	CD:I36:SI / CD1:L52: β 3 (60) CD1:L52: β 3 / CD:I36:SI (90)

Table A.7. FoldX energy calculations for H-Ras homodimers

	Mutants	$\Delta\Delta G$ (kcal/mol)
β-Homodimer	Q25A	1.58
	E37K	0.56
	S39A	0.34
	Y40A	0.16
	S39A+Y40A	0.62
	R41E	8.14
	K42D	5.03
	R41E+K42D	11.87
	R41A	1.06
	K42A	5.98
	R41A+K42A	7.64
α-Homodimer	H94A	-5.21
	R97E	2.85
	E98R	5.04
	E98Q	3.27
	K101D	3.27
	R102E	5.59
	K101D+R102E	9.65
	E98A	1.97
	K101A	1.35
	R102A	3.67
	K101A+R102A	5.92

Table A.8. FoldX energy calculations for K-Ras4B homodimers

	Mutants	$\Delta\Delta G$ (kcal/mol)
β-Homodimer	Q25A	1.28
	E37K	2.35
	S39A	0.34
	Y40A	0.16
	S39A+Y40A	0.62
	R41E	8.14
	K42D	5.03
	R41E+K42D	11.87
	R41A	5.04
	K42A	2.83
	R41A+K42A	8.69
α-Homodimer	H94A	0.95
	R97E	-4.00
	E98R	5.31
	E98Q	3.34
	K101D	3.38
	R102E	3.59
	K101D+R102E	9.73
	E98A	0.82
	K101A	0.37
	R102A	1.52
	K101A+R102A	3.22

Table A.9. All available complexes of human H-Ras with protein binding partners in PDB.

Monomer 1	Monomer 2	Complex PDB ID
H-Ras	Sos1	1BKD, 1NVU, 4URU, 4URV, 4URW, 4URX, 4URY, 4URZ, 4US0, US1, 4US2,
	p120GAP	1WQ1
	Raf	4G0N, 4G3X
	PI3Kgamma	1HE8
	RalGDS	1LFD
	PLCepsilon	2C5L
	Bry22	1K8R
	RASSF5 (Nore1A)	3DDC

Table A.10. Predicted complexes of H- and K-Ras proteins with their binding partners.

Ras Isoform	Binding Partner	Template Interface	BES
H-Ras	AFAD RA 1	1lfdCD	-21.71
	AFAD RA 2	1mo1AB	-17.80
	RAIN	3iicAB	-32.06
	RGS12	1fr3AB	-14.28
	RASSF1	1whmAB	-32.49
	RGL1	1fr3AB	-35.40
	CDC42	2erxAB	-26.56
K-Ras	Sos1	1nvuQS	-37.47
	p120GAP	1wq1GR	-23.16
	Raf	1c1yAB	-51.19
	PI3Kalpha	1lfdCD	-23.24
	RalGDS	1lfdCD	-45.24
	PLCepsilon	1lfdCD	-37.26
	Bry2	1k8rAB	-43.50
	AFAD RA 1	2pmcAB	-32.66
	AFAD RA 2	1mo1AB	-31.20
	RAIN	1lfdCD	-8.31
	RASSF5 (Nore1A)	1lfdCD	-51.49
	CDC42	2erxAB	-18.29

Table A.11. Hotspot residues located on the Ras-effector interfaces

Complex	Hotspots on Ras interface	Hotspots on effector interface
H-Ras/AFAD	I36, M67, E76 and H166	C59, I60, T249, R251 and Y263
H-Ras/RAIN	Q22, L23, I24, Q25, H27, F28, R149, V152 and Y157	L208, V238, L241, W242 and R250
H-Ras/Cdc42	Q25, I36, Y40, L52 and Y64	I21, V36, F37, Y40, T52 and Y64

H-Ras/RASSF1	I24, R41 and K42	A252, R254, Q268 and L275
H-Ras/RGL1	T2, Y4, V160, I163 and R164	L708, F717, Y718, M720 and S722
H-Ras/RGS12	Y4, I163 and R164	C974, V976, L991 and H995
K-Ras/Raf	I21, E37, D38, Y40 and L56	Q66, T68, V69 and R89
K-Ras/PI3K p110 α	I24, E37, Y40 and R41	W195, Q205, K206, M282 and L792
K-Ras/Sos1	Q22, N26, D38, Y40, L56 and R149	Y618 and R688
K-Ras/p120GAP	I21, I36, E37, D38, S39 and Y40	R789, L902, C906, L910, I931, K935, Q938, K949 and Y952
K-Ras/RalGDS	I24, I36 ve Y40	M813 and Y814
K-Ras/PLC ϵ	Q25, D38 ve Y40	Q2148, V2152 and S2175
K-Ras/Bry2	I36, Y40 ve R41	R83 and V85
K-Ras/Cdc42	Q25, I36, Y40, L52 and Y64	I21, V36, F37, Y40, T52 and Y64
K-Ras/RASSF5	I21, I24, Q25, Y40, R41 and M67	T25, K27, Y40, A41, V42 and Q70
K-Ras/RAIN	I21, I24 and Y40	A159, Y161, K162 and R182
K-Ras/AFAD	E3, Y4, E76, F90, V125, Q129, L133, Y137 and I163	H40, C59, I60, R61, V62, T74, T249, L250, Y253, L326 and F329

Table A.12. Hotspot residues located on the Ras-Ras interfaces

Ras	Dimer Type	Hotspots
H-Ras-GTP	β -Homodimer	I21, I24, Q25, H27, E37, Y40, R41 and L52
	α -Homodimer	F90, H94, R97, K101, Q129, D132, L133, S136 and Y137
K-Ras4B-GTP	β -Homodimer	I21, I24, Q25, H27, Y40 and R41
	α -Homodimer	H94, R97, L133, S136 and Y137

Table A.13. Average RMSD values of the K-Ras4B, PDE δ and K-Ras4B/PDE δ complex

Configuration	Average RMSD (\AA)		
	K-Ras4B	PDED δ	Complex
System 1	4.9 \pm 0.7	2.8 \pm 0.3	11.9 \pm 3.1

System 2	5.5 ± 0.8	2.1 ± 0.2	13.9 ± 3.6
System 3	6.9 ± 1.2	2.2 ± 0.2	12.3 ± 2.3
System 4	5.8 ± 1.3	1.7 ± 0.1	9.9 ± 2.8
System 5	6.9 ± 0.9	2.5 ± 0.3	11.6 ± 1.7
System 6	3.8 ± 0.5	2.1 ± 0.2	9.6 ± 1.2

Table A.14. Types of atomic interactions in the prenylated K-Ras4B-GTP/PDE δ complex. The number in the parenthesis denotes percentage of the atomic pair interaction based on the distance between the paired atoms.

Configuration	H-bond K-Ras4B / PDEδ (%)	Salt-bridge K-Ras4B / PDEδ (%)
System 1	Lys184 / Glu88 (34.92)	Lys184 / Glu88 (28.92)
System 2	Lys184 / Glu88 (45.50) Lys182 / Glu89 (22.17) Glu63 / Arg9 (19.33) Lys178 / Glu88 (16.75) Lys177 / Glu89 (16.50) Asp105 / Lys79 (16.00)	Lys177 / Glu89 (28.58) Lys184 / Glu88 (25.00) Asp105 / Lys79 (17.92) Lys182 / Glu88 (17.75) Asp105 / Lys132 (16.25) Lys178 / Glu88 (15.08)
System 3	Lys184 / Glu88 (30.92) Thr183 / Glu88 (27.92) Lys176 / Glu77 (24.58) Lys178 / Glu93 (20.25)	Lys176 / Glu77 (33.80) Lys175 / Asp136 (28.92)
System 4	Thr183 / Glu88 (68.25) Lys184 / Glu88 (49.75) Lys172 / Asp137 (37.33) Lys172 / Asp136 (30.67) Lys177 / Glu89 (30.17) Lys182 / Ala112 (28.17) Lys169 / Glu93 (18.92) Lys176 / Glu93 (17.75) Lys180 / Glu110 (16.50)	Lys172 / Asp136 (55.80) Lys172 / Asp137 (53.70) Lys169 / Glu93 (36.80) Lys180 / Glu110 (22.30) Lys177 / Glu89 (15.30)
System 5	Thr183 / Glu110 (63.92) Thr183 / Glu88 (55.42) Ser181 / Glu88 (49.42) Lys182 / Glu88 (45.17) His95 / Pro113 (24.58) Tyr64 / Met117 (24.17) Lys180 / Glu88 (21.50) Lys182 / Ala112 (17.42) Lys180 / Glu89 (15.83) Gln99 / Ser115 (15.08)	Lys182 / Glu110 (16.30) Lys178 / Glu89 (15.25)
System 6	Arg73 / Glu77 (71.17) Ser181 / Glu88 (34.42) Asp69 / Lys79 (33.67) Cys185 / Ala112 (31.08) Lys182 / Glu88 (26.25) Lys184 / Met118 (25.50) Lys179 / Glu88 (23.67) Arg73 / Glu89 (20.33)	Lys182 / Glu88 (25.70) Lys179 / Glu88 (22.60) Asp69 / Lys79 (22.50)

Table A.15. Types of atomic interactions of the HVRs of both K-Ras4A and N-Ras with PDE δ . The number in the parenthesis denotes percentage of the atomic pair interaction based on the distance between the paired atoms.

Configuration	H-bond HVR/ PDE δ (%)	Salt-bridge HVR / PDE δ (%)
System A1	Lys185 / Glu88 (43.95) Lys182 / Glu88 (27.05) Lys185 / Glu114 (18.15)	Lys185 / Glu88 (97.3)
System A2	Lys185 / Glu88 (53.50) Lys184 / Glu88 (45.75) Lys185 / Glu88 (42.10) Arg167 / Glu93 (31.25) Arg167 / Glu93 (35.45) Cys180 / Glu89 (17.60)	Lys185 / Glu88 (93.5) Lys 173 / Glu89 (16.45)
System N1	Arg167 / Glu110 (35.75) Cys181 / Glu110 (31.40) Met182 / Glu88 (26.95) Gly183 / Glu88 (24.60) Cys181 / Ala112 (16.50)	NA
System N2	Gly183 / Glu88 (17.10) Arg167 / Glu110 (16.75) Pro185 / Tyr149 (15.75)	NA

Table A.16: Raw data of the H-Ras westerns at 6, 12 and 24h.

H-Ras (G12V)	Experiment 1			Experiment 2			Experiment 3		
	Ras/H3	ERK/H3	pERK/H3	Ras/H3	ERK/H3	pERK/H3	Ras/H3	ERK/H3	pERK/H3
Control	1,191365	2,96680	0,064280	1,086379	0,678406	13,44283	0,007680	0,292286	0,063725
(A3)	1,397551	2,91023	0,102898	0,638890	0,117146	4,963487	0,012850	0,24042	0,043763
(B3)	0,831188	3,87136	0,000000	1,182865	0,15471	4,208436	0,045827	0,248108	0
Control	7,888772	1,46233	0,187121	1,477236	4,134112	1,27728	1,4860068	0,167498	0,216553
(A3)	3,103672	1,20347	0,24455	1,193897	5,583514	1,491049	0,2500214	0,176207	0,269993
(B3)	3,787316	0,90095	0,008072	1,196992	4,366142	0,130499	2,5795915	0,19536	0
Control	0,630021	1,85578	0,445778	0,749871	1,333526	0,560595	1,2281379	1,802357	0,277023
(A3)	0,139786	1,94855	0,559667	0,615753	0,990786	0,570229	0,7052433	1,643611	0,139796
(B3)	0,382602	1,78691	0,03171	0,709887	0,687250	0,051388	0,7008687	1,294281	0,037204

Table A.17: Raw data of the K-Ras4B westerns at 6, 12 and 24h.

K-Ras4B (G12D)	Experiment 1			Experiment 2			Experiment 3		
	Ras/H3	ERK/H3	pERK/H3	Ras/H3	ERK/H3	pERK/H3	Ras/H3	ERK/H3	pERK/H3
Control	0,543292	0,512375	0,14103	1,716766	8,203758	3,541598	0,475691	0,924046	2,135086
(A3)	0,284679	0,433078	0,096533	0,840630	8,559701	3,111852	0,714146	1,173279	1,773366
(B3)	0,227775	0,430363	0,006058	0,796748	6,962458	0,171926	1,106067	1,292854	0

Control	1,034323	1,05345	0,329811	3,810769	4,501445	1,221561	3,517924	11,53784	6,512694
(A3)	1,113439	0,82469	0,349091	2,457235	5,950749	1,309192	2,148108	9,947246	6,733794
(B3)	1,000848	0,505756	0	3,217347	5,845702	0	1,874572	7,29874	0,477005
Control	3,112618	1,447845	0,996164	6,402493	10,56648	6,642594	0,785993	1,25748	0,428135
(A3)	0,967939	1,828573	1,151567	1,331477	10,76926	7,153003	0,533727	1,200185	0,351475
(B3)	0,956988	1,543837	0,359568	2,217664	12,28029	1,780111	0,560565	0,853198	0,027449



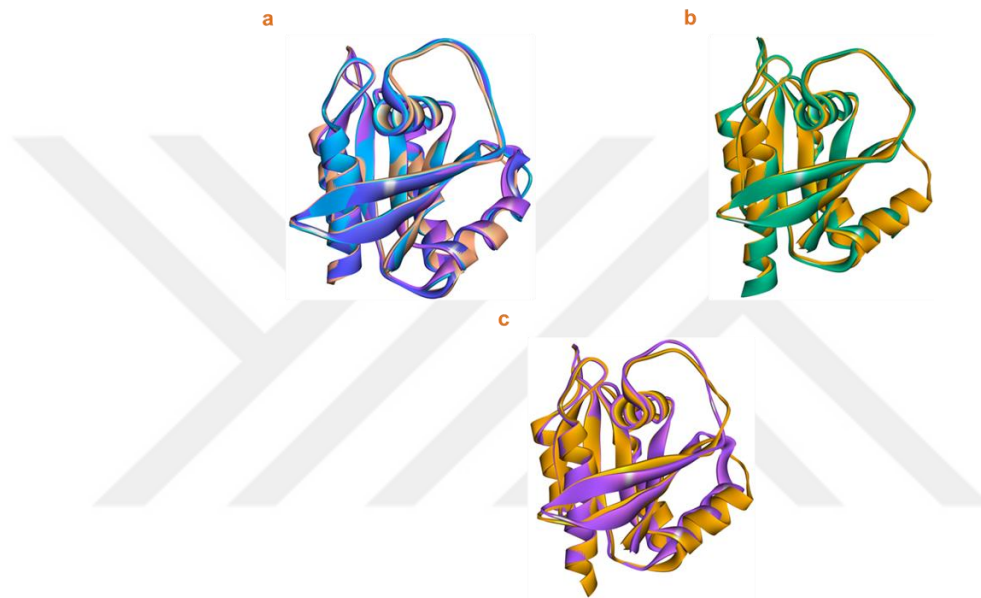
APPENDIX B

Figure B.1. Superposition of the wild type H-Ras structures. (a) Superposition of GTP>P analogs-bound H-Ras structures (PDB ID: 1QRA, magenta; PDB ID: 1CTQ, purple; PDB ID: 121P, blue; PDB ID: 1GNR, pink). (b) Superposition of GDP-bound H-Ras structures (PDB ID: 1IOZ, green; PDB ID: 4Q21, orange). (c) Superposition of GTP&GDP-bound H-Ras structures (PDB ID: 1QRA, magenta; PDB ID: 4Q21, orange).

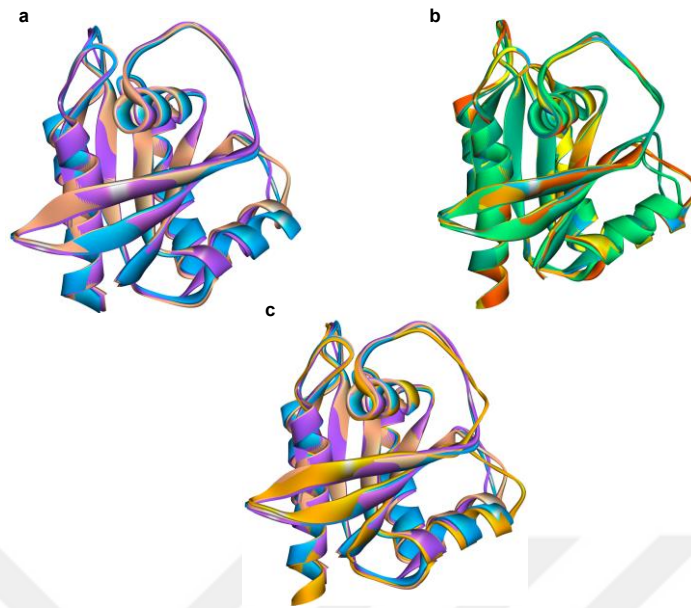


Figure B.2. Superposition of the K-Ras structures. (a) Superposition of GTP analogs-bound K-Ras structures (PDB ID: 4DSN, pink; PDB ID: 4DSO, magenta; PDB ID: 3GFT, blue). (b) Superposition of GDP-bound K-Ras structures (PDB ID: 4EPW, dark orange; PDB ID: 4EPR, light green; PDB ID: 4EPT, dark green; PDB ID: 4EPV, yellow; PDB ID: 4EPX, blue; PDB ID: 4EPY, orange). (c) Superposition of GTP analogs&GDP-bound K-Ras structures (PDB ID: 4DSN, pink; PDB ID: 4DSO, magenta; PDB ID: 3GFT, blue; PDB ID: 4EPY, orange).

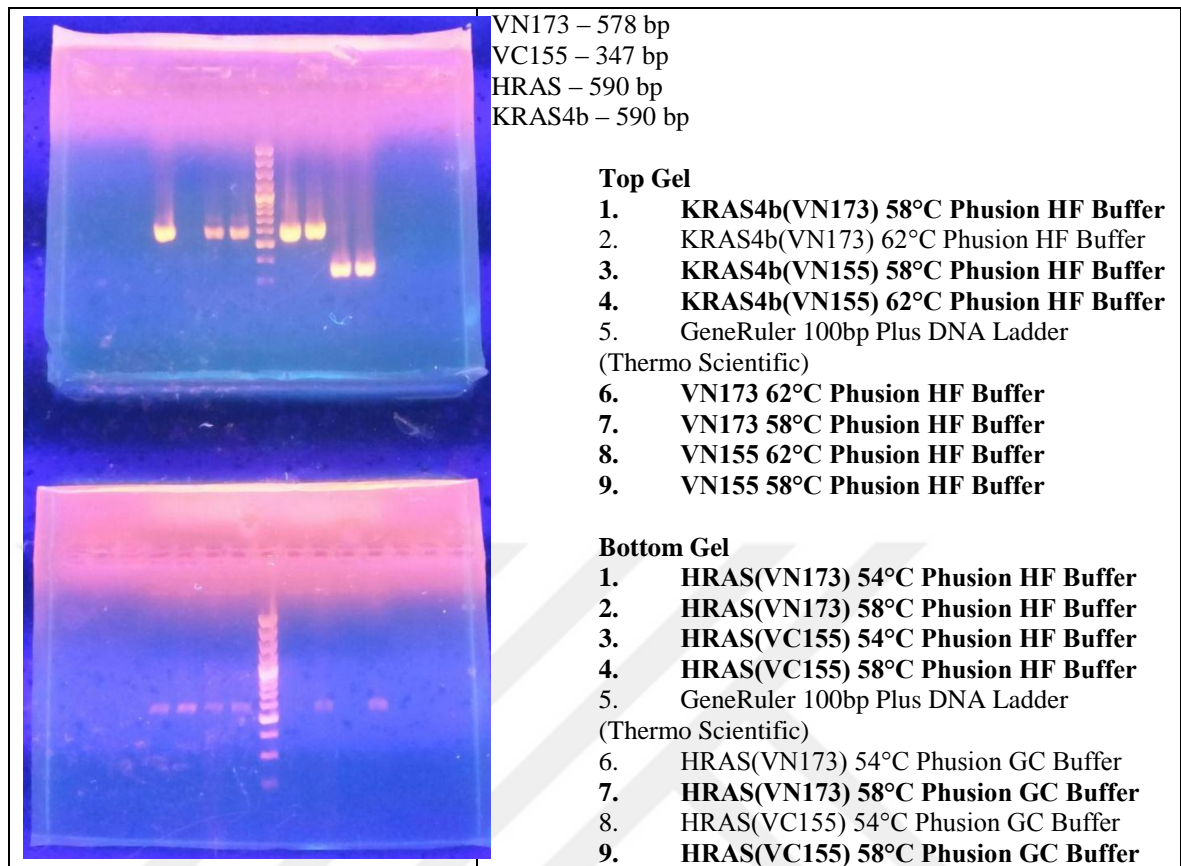


Figure B.3. Gel electrophoresis of PCR products (VN173, VC155, HRAS and KRAS4B). Bold ones represent the successfully amplified samples.

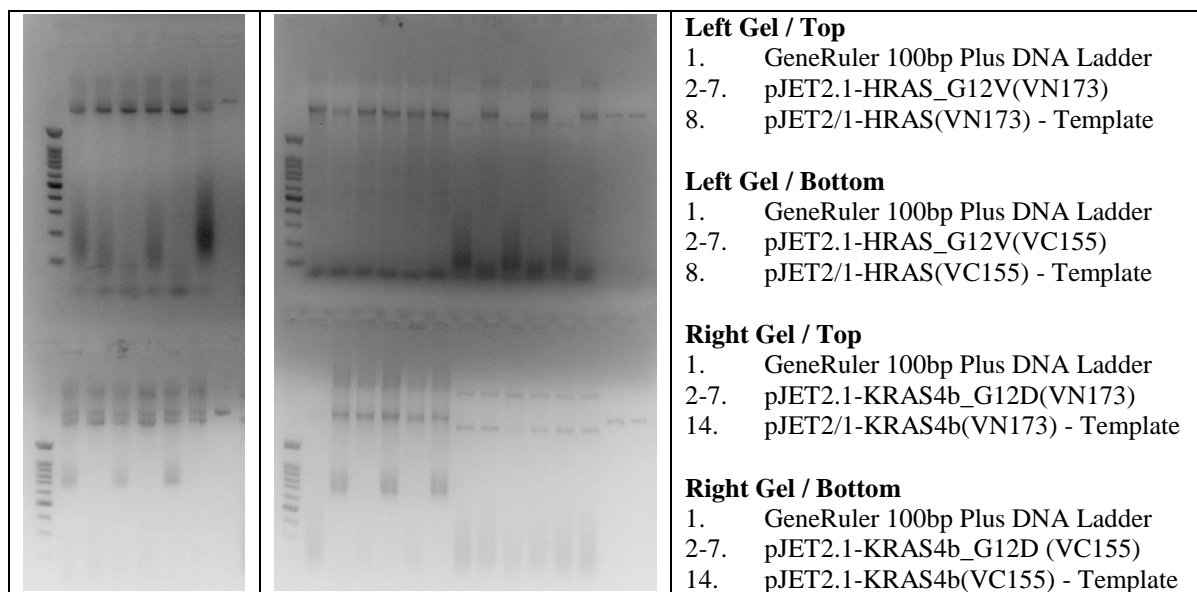


Figure B.4. Site-directed mutagenesis results. (The lanes between 8 and 13 and lane 15 on the right gel consist of different samples.)

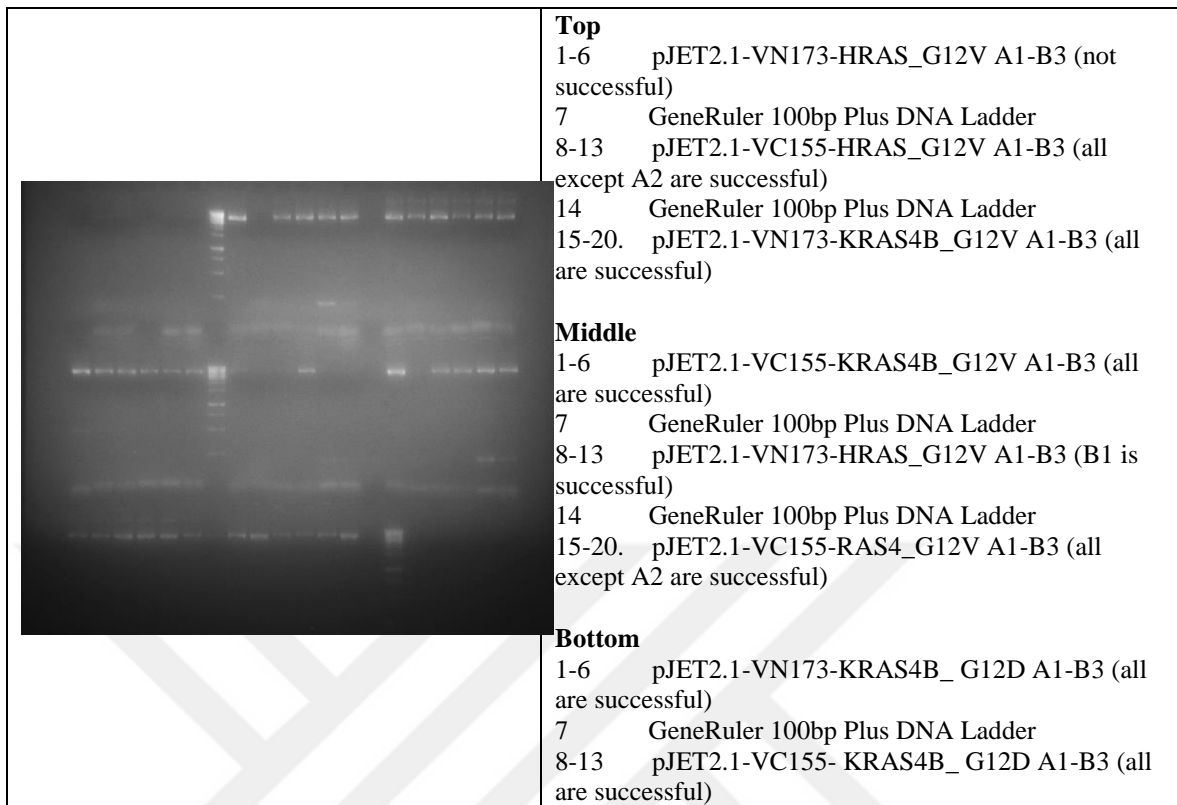


Figure B.5. PCR gels of SDM experiments done with pJET2.1-Venus-RAS constructs carrying the constitutively active forms of RAS.

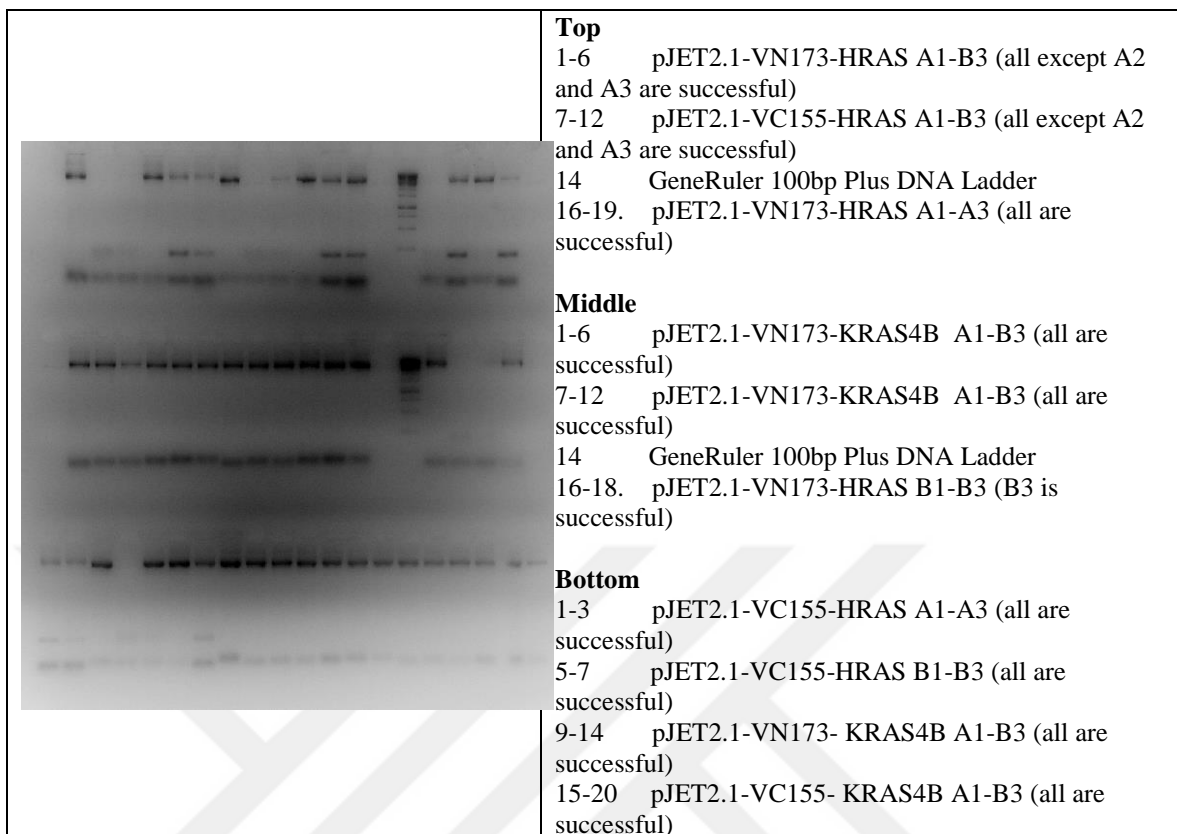


Figure B.6. PCR gels of SDM experiments done with pJET2.1-Venus-RAS constructs carrying the wild type RAS.

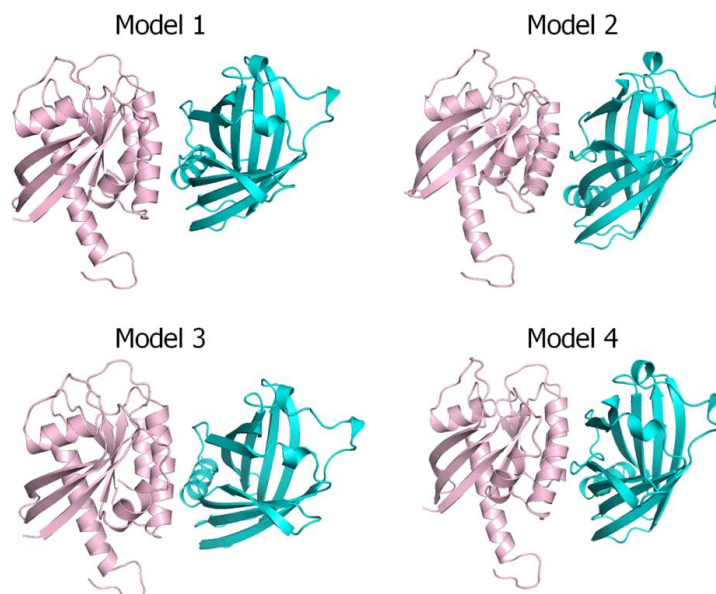


Figure B.7. Predicted models of the K-Ras4B catalytic domain interacting with PDE δ by using the standard Rosetta global docking method.

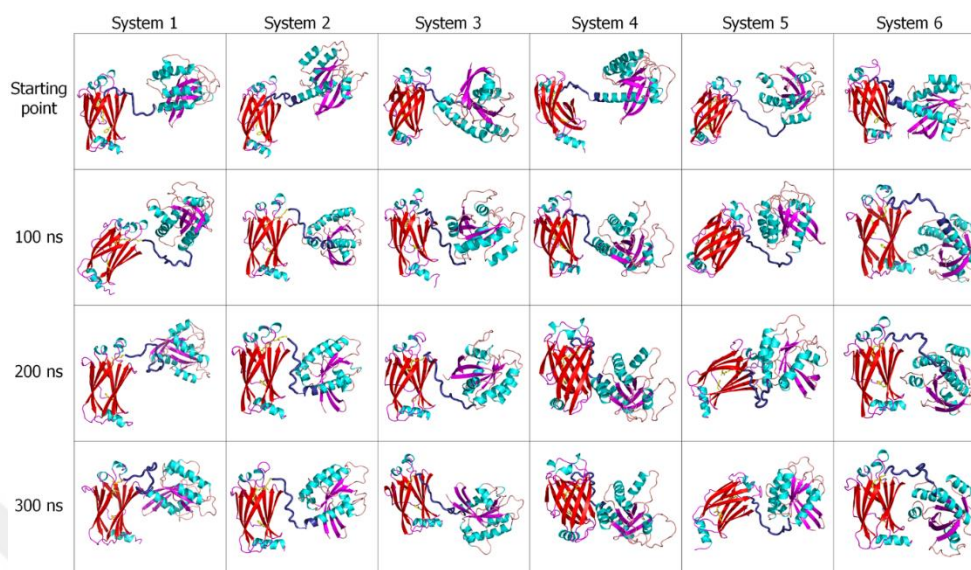


Figure B.8. The snapshots of K-Ras4B-GTP/PDE δ complex (System 1 – System 6) at the start point, 100 ns, 200 ns, and 300 ns run points.

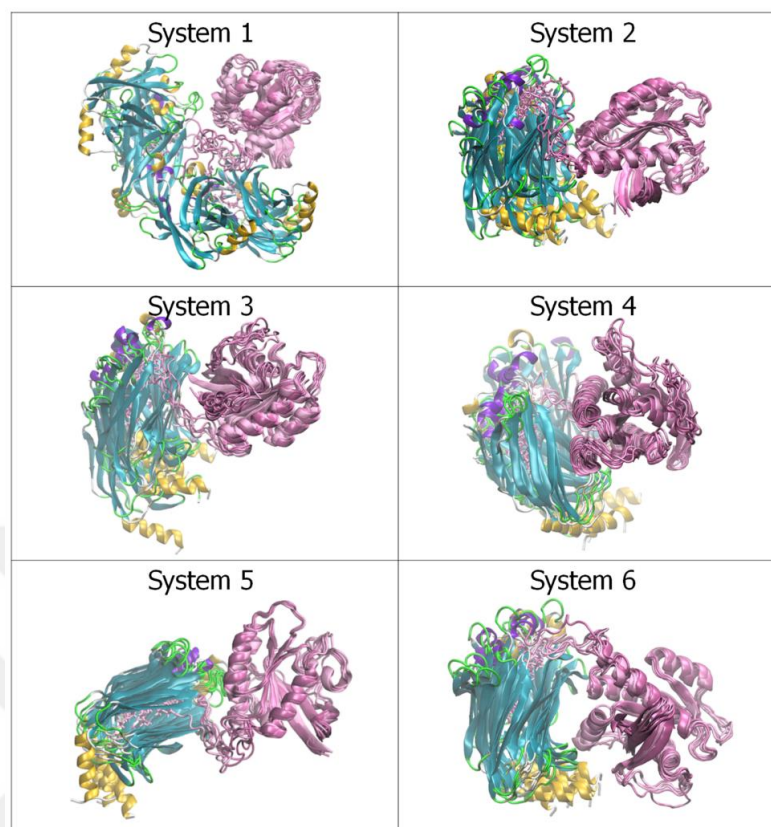


Figure B.9. The superimposed snapshots taken every 50 ns simulations of these six K-Ras4B-GTP/PDE δ systems.

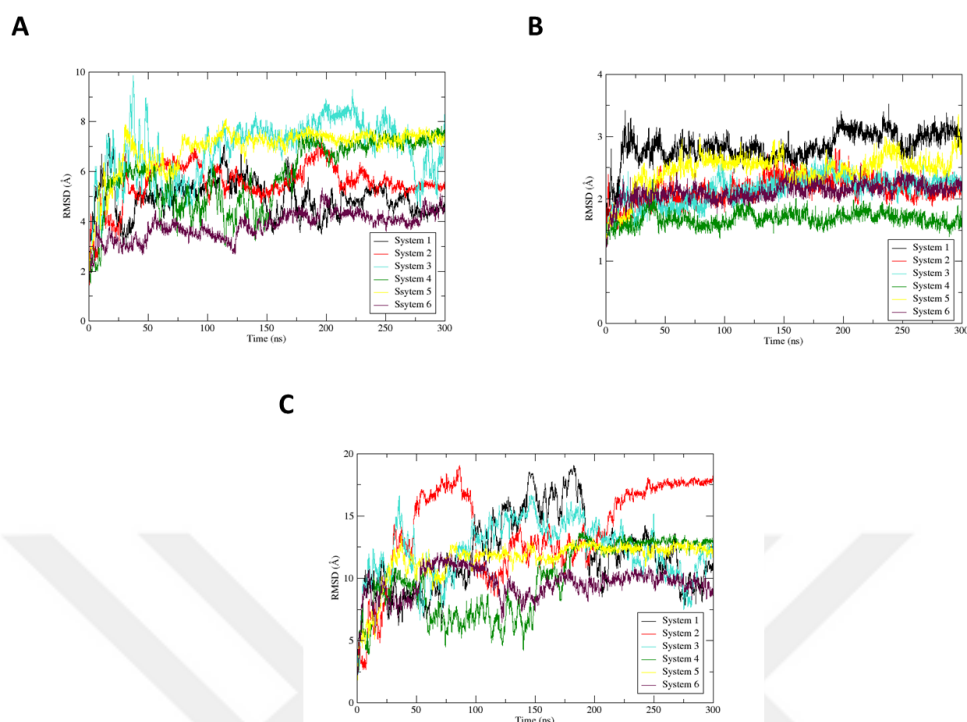


Figure B.10. Root-mean-squared deviations (RMSDs) of (A) K-Ras4B, (B) PDE δ , and (C) K-Ras4B/PDE δ complex in the six K-Ras4B/PDE δ systems.

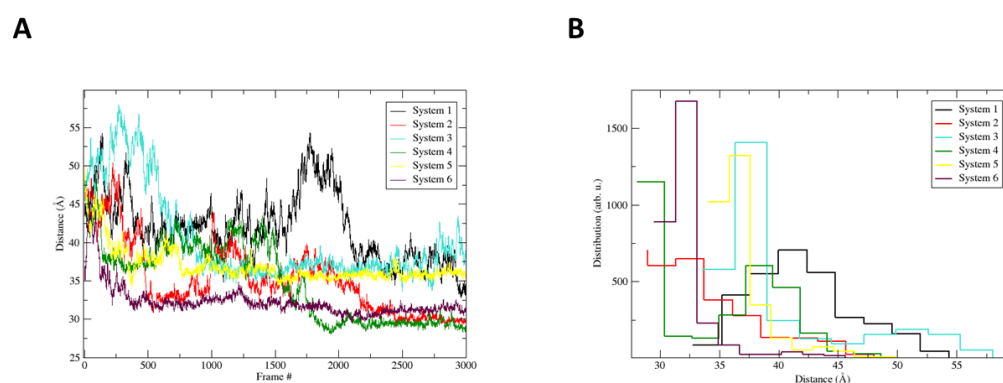


Figure B.11. Distance analysis of the six K-Ras4B/PDE δ systems. (A) The center of mass distance between K-Ras4B and PDE δ of the six K-Ras4B/PDE δ systems. (B) Distribution of the center of mass distance of the six simulated K-Ras4B/PDE δ systems.

APPENDIX C

A sample minimization configuration file

```

# FILE: kt1f1pde_water_namd_preequ_mini.cnfg
# Minimization of solvent with protein fix
# Constraint lipid molecules on x-y plane

# Set variable values
set temp      310
set dir       /data/muratcioglus/kt1f1pde_water
set type      kt1f1pde_water

# Parameters
paraTypeCharmm on
parameters    /data/muratcioglus/charmm_input/par_all36_ras_c39b2_hbj.inp

# Input files
structure     ${223}/psf/${226}_namd_salt_xplor.psf  ;# Name of structure file
coordinates   ${223}/coor/${226}_namd_salt_charmm.pdb ;# Name of input pdb file

# Restart files
# NOTE: Do not set the initial restart velocity if you have also specified a temperature!
if [163] {
velocities    ${dir}/vel/                ;# Initial velocities in pdb file
binVelocities ${223}/vel/                ;# Initial velocities in binary format
;# Remove the "temperature" entry if you use this!
binCoordinates ${223}/coor/              ;# Initial coor in binary format
extendedSystem ${223}/xsc/               ;# Input periodic cell para read from
}

# Simulation temperature
# NOTE: Do not set the initial velocity temperature if you have also specified a .vel restart file!
temperature   $temp

# Output files
outputName    ${223}/coor/${226}_namd_preequ_mini_pdb ;# Name of final output coor file
binaryoutput  no                                     ;# Save final coor in binary format
restartname   ${223}/coor/${226}_namd_preequ_mini    ;# Name of output(restart) coor & vel file
binaryrestart yes                                    ;# Save restart file in binary format
restartfreq   10000                                  ;# Freq saving coor & vel (1000 steps = every 1ps)
restartsave   yes                                    ;# Append time step at end of file name
dcdfile      ${223}/trj/${226}_namd_preequ_mini.dcd ;# Name of trajectory file
dcdfreq      100                                    ;# Freq saving trajectory
dcdUnitCell  yes                                    ;# Write unit cell data to dcd file
#velcdfile   ${223}/vel/${226}_namd_preequ_mini_vel.dcd ;# Name of vel trajectory file
#velcdfreq   500                                    ;# Freq saving vel trajectory

# Output configurations
outputEnergies 100 ;# Freq for printing Energies
outputTiming   100 ;# Freq for printing Timing info
outputPressure 100 ;# Freq for printing Pressure

```



```
reassignIncr    30.0                ;# Temperature increment or decrement
reassignHold    $temp                ;# Target temperature
}

# Constant pressure control
useGroupPressure yes                ;# Should use w/SHAKE, needed for 2fs steps
useFlexibleCell no                   ;# Allows dimensions of cell to fluctuate
                                        ;# no for water box, yes for membrane
useConstantArea no                   ;# x-y fixed and z dim can vary
                                        ;# no for water box, yes for membrane

if {1} {
LangevinPiston on                    ;# Use Nose-Hoover Langeving Piston Algorithm
LangevinPistonTarget 1.01325         ;# Target pressure to run simu at (bars)
LangevinPistonPeriod 200             ;# Oscillation period
LangevinPistonDecay 100              ;# Damping time scale
LangevinPistonTemp $temp             ;# Should be set equal to the target temperature
SurfaceTensionTarget 0.0             ;# Apply surface tension in xy plane (dyn/cm)
}

# Fix hydrogens
if {1} {
rigidBonds      all                  ;# Fix h-bonds to none, water, or all h-atoms
rigidTolerance  1.0e-8              ;# Allowable bond-length error for ShakeH
rigidIterations 100                  ;# Maximum ShakeH iterations
rigidDieOnError on                   ;# Exit and report an error
useSettle       off                  ;# Keep waters rigid
}

# Harmonic constraints : constraint protein backbone with k=5
if {1} {
constraints     off                  ;# Turn on the use of constraints
consexp         2                    ;# Exponent to be use in harmonic constraint energy
consref         ${dir}/cons/preequ_constr_atoms_ref_5.pdb ;# A pdb file to use for reference positions
conskfile       ${dir}/cons/preequ_constr_atoms_kfile_5.pdb ;# A pdb file to use for k values
conskcol        B                    ;# Column of pdb file to use for harmonic constraint
}

# Fixed atoms constraint : fix protein
if {1} {
fixedAtoms      on                   ;# Turn on the use of constraints
fixedAtomsForces on                  ;# Calculate forces between fixed atoms
fixedAtomsFile  ${dir}/cons/preequ_fix_protein.pdb      ;# A pdb file to use for reference positions
fixedAtomsCol   O                      ;# Set O to read occupancy column in pdb file
}

# Minimization parameters
if {1} {
minimization     on                   ;# Perform conjugate gradient energy minimization
minTinyStep      1.0e-8               ;# First initial step for line minimizer
minBabyStep      1.0e-2               ;# Max initial step for line minimizer
minLineGoal      1.0e-4               ;# Gradient reduction factor for line minimizer
}

# Extra parameters
# Put here any custom parameters that are specific to this job

# Execution script
```

```

#-----#
minimize      10000                ;# Minimization step
#-----#
#-----#
#run          10000                ;# Dynamics step
#-----#
# End of script
Scripts for MMGBSA calculations:

```

Sample job file

```

#!/bin/bash
#####
# SGE options:
#
#$ -S /bin/bash
#$ -cwd
#$ -j y
#$ -notify
#$ -q cosbi.q
#$ -o $JOB_ID.out
#$ -e $JOB_ID.err
#$ -M smuratcioglu@ku.edu.tr

#$ -pe smp 4
#$ -N Workshop_MMGBSA
# end of SGE stuff
#####

export AMBERHOME=/share/apps/amber/amber14

export PATH=$AMBERHOME:$PATH
export LD_LIBRARY_PATH=$AMBERHOME/lib:$AMBERHOME/lib64:$LD_LIBRARY_PATH
export LD_LIBRARY_PATH=$LD_LIBRARY_PATH:/share/apps/gcc/gcc-4.8.4/lib64

##psf to prmtop conversion
/share/apps/amber/amber14/AmberTools/bin/chamber -top top_all36_ras_c39b2_hbj.inp -param
par_all36_ras_c39b2_hbj.inp -xpsf nraf1pde_water_namd_salt_charmm.psf -crd
nraf1pde_water_namd_salt_charmm.pdb -p nraf1pde_solvated.prmtop -inpcrd nraf1pde_solvated.inpcrd -
cmap -verbose > verbose.log.v14

##creating complex, receptor and ligand topology files from solvated_complex.prmtop
/share/apps/amber/amber14/AmberTools/bin/ante-MMPBSA.py -p nraf1pde_solvated.prmtop -c
nraf1pde_complex.prmtop -r nraf1pde_pded.prmtop -l nraf1pde_hvr.prmtop -s ':SOD,;MG,;CLA,;WAT' -n
':1-20,;GTP'

##running MMGBSA
/share/apps/amber/amber14/AmberTools/bin/MMPBSA.py -O -i mmgbsa.in -o
FINAL_RESULTS_MMGBSA.dat -sp nraf1pde_solvated.prmtop -cp nraf1pde_complex.prmtop -rp
nraf1pde_pded.prmtop -lp nraf1pde_hvr.prmtop -y
nraf1pde_water_namd_prod_merged_200ns_total_mmgbsa.dcd

```

MMGBSA.in (input file)

&general #for both MMPB/GBSA

```
endframe=2000, verbose=100, strip_mask=":WAT:SOD:CLA:MG"  
/  
&gb #indicates that the calculations will be done using MMGBSA  
igb=2, saltcon=0.100  
/
```



APPENDIX D

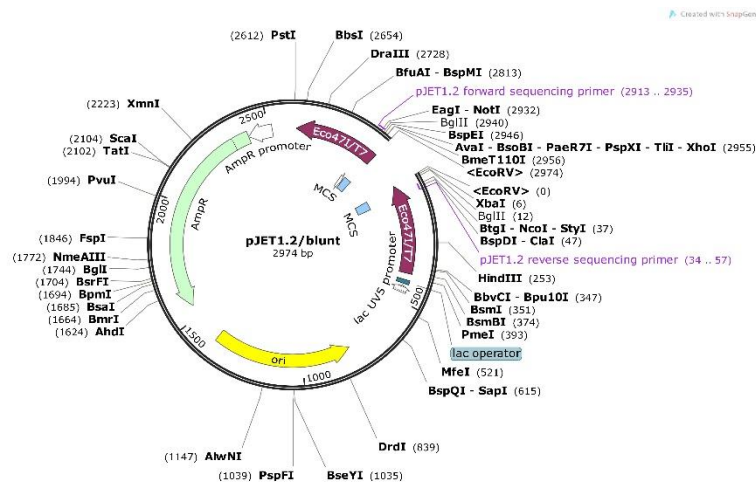


Figure D.1. pJET2.1blunt vector map

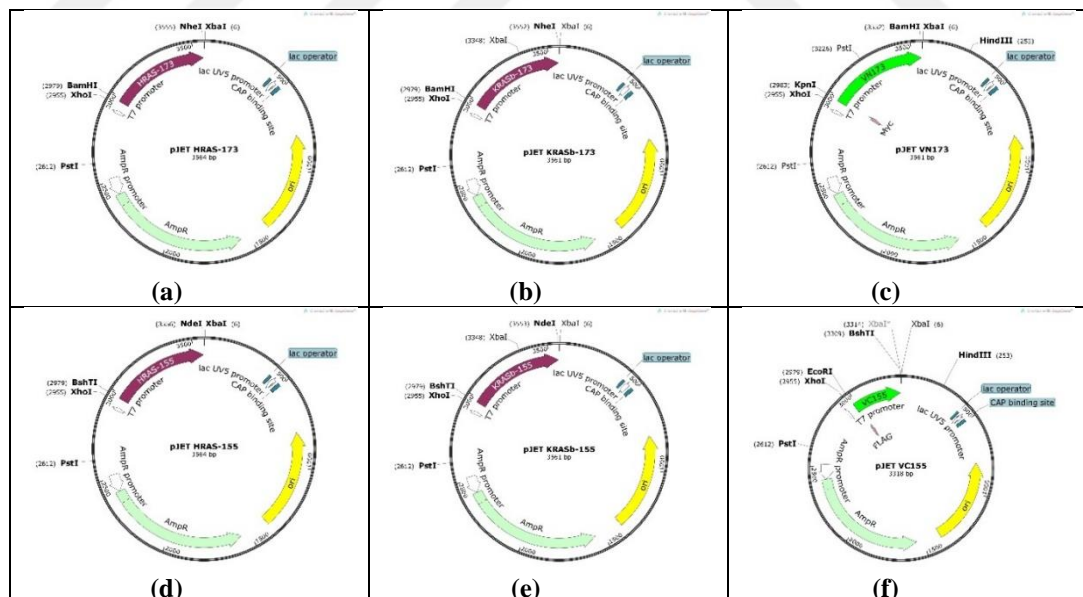


Figure D.2. (a, d) pJET2.1-HRAS, (b, e) pJET2.1-KRAS4b, (c) pJET2.1-VN173 and (f) pJET2.1-VC155 recombinant plasmids. Restriction cut sites for both pJET2.1 and pTRE-Tight-BI cloning are shown.

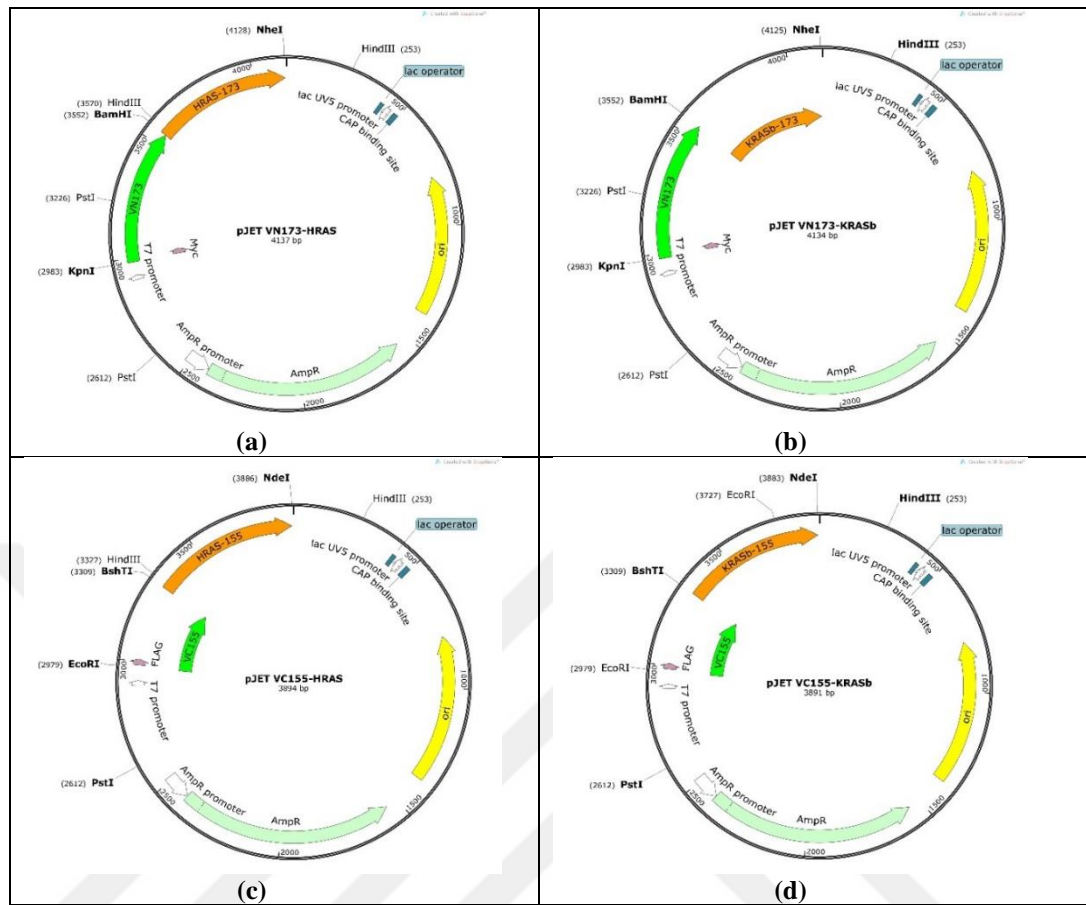


Figure D.3. (a, b) pJET2.1-Ras (VN173) ligated with the VN173. (c, d) pJET2.1-Ras (VC155) ligated with the VC155. Cloning and restriction sites are shown.

BIBLIOGRAPHY

1. Nan, X., et al., *Single-molecule superresolution imaging allows quantitative analysis of RAF multimer formation and signaling*. Proc Natl Acad Sci U S A, 2013. **110**(46): p. 18519-24.
2. Guldenhaupt, J., et al., *N-Ras forms dimers at POPC membranes*. Biophys J, 2012. **103**(7): p. 1585-93.
3. Lin, W.C., et al., *H-Ras forms dimers on membrane surfaces via a protein-protein interface*. Proc Natl Acad Sci U S A, 2014. **111**(8): p. 2996-3001.
4. Gysin, S., et al., *Therapeutic strategies for targeting ras proteins*. Genes Cancer, 2011. **2**(3): p. 359-72.
5. Cox, A.D., C.J. Der, and M.R. Philips, *Targeting RAS Membrane Association: Back to the Future for Anti-RAS Drug Discovery?* Clin Cancer Res, 2015. **21**(8): p. 1819-27.
6. Harvey, J.J., *An Unidentified Virus Which Causes the Rapid Production of Tumours in Mice*. Nature, 1964. **204**: p. 1104-5.
7. Kirsten, W.H. and L.A. Mayer, *Morphologic responses to a murine erythroblastosis virus*. J Natl Cancer Inst, 1967. **39**(2): p. 311-35.
8. Scolnick, E.M., et al., *Studies on the nucleic acid sequences of Kirsten sarcoma virus: a model for formation of a mammalian RNA-containing sarcoma virus*. J Virol, 1973. **12**(3): p. 458-63.
9. Shih, T.Y., et al., *Identification of a sarcoma virus-coded phosphoprotein in nonproducer cells transformed by Kirsten or Harvey murine sarcoma virus*. Virology, 1979. **96**(1): p. 64-79.
10. Scolnick, E.M. and W.P. Parks, *Harvey sarcoma virus: a second murine type C sarcoma virus with rat genetic information*. J Virol, 1974. **13**(6): p. 1211-9.
11. Scolnick, E.M., A.G. Papageorge, and T.Y. Shih, *Guanine nucleotide-binding activity as an assay for src protein of rat-derived murine sarcoma viruses*. Proc Natl Acad Sci U S A, 1979. **76**(10): p. 5355-9.
12. Willingham, M.C., et al., *Localization of the src gene product of the Harvey strain of MSV to plasma membrane of transformed cells by electron microscopic immunocytochemistry*. Cell, 1980. **19**(4): p. 1005-14.
13. Santos, E., et al., *T24 human bladder carcinoma oncogene is an activated form of the normal human homologue of BALB- and Harvey-MSV transforming genes*. Nature, 1982. **298**(5872): p. 343-7.
14. Der, C.J., T.G. Krontiris, and G.M. Cooper, *Transforming genes of human bladder and lung carcinoma cell lines are homologous to the ras genes of Harvey and Kirsten sarcoma viruses*. Proc Natl Acad Sci U S A, 1982. **79**(11): p. 3637-40.
15. Parada, L.F., et al., *Human EJ bladder carcinoma oncogene is homologue of Harvey sarcoma virus ras gene*. Nature, 1982. **297**(5866): p. 474-8.
16. O'Toole, C.M., et al., *Identity of some human bladder cancer cell lines*. Nature, 1983. **301**(5899): p. 429-30.
17. Capon, D.J., et al., *Activation of Ki-ras2 gene in human colon and lung carcinomas by two different point mutations*. Nature, 1983. **304**(5926): p. 507-13.
18. Shimizu, K., et al., *Three human transforming genes are related to the viral ras oncogenes*. Proc Natl Acad Sci U S A, 1983. **80**(8): p. 2112-6.

19. Hall, A., et al., *Identification of transforming gene in two human sarcoma cell lines as a new member of the ras gene family located on chromosome 1*. Nature, 1983. **303**(5916): p. 396-400.
20. Pulciani, S., et al., *Oncogenes in solid human tumours*. Nature, 1982. **300**(5892): p. 539-42.
21. Campbell, S.L., et al., *Increasing complexity of Ras signaling*. Oncogene, 1998. **17**(11 Reviews): p. 1395-413.
22. Reuther, G.W. and C.J. Der, *The Ras branch of small GTPases: Ras family members don't fall far from the tree*. Curr Opin Cell Biol, 2000. **12**(2): p. 157-65.
23. Downward, J., *The ras superfamily of small GTP-binding proteins*. Trends Biochem Sci, 1990. **15**(12): p. 469-72.
24. Grand, R.J. and D. Owen, *The biochemistry of ras p21*. Biochem J, 1991. **279** (Pt 3): p. 609-31.
25. Bourne, H.R., D.A. Sanders, and F. McCormick, *The GTPase superfamily: conserved structure and molecular mechanism*. Nature, 1991. **349**(6305): p. 117-27.
26. Wittinghofer, A. and E.F. Pai, *The structure of Ras protein: a model for a universal molecular switch*. Trends Biochem Sci, 1991. **16**(10): p. 382-7.
27. Wittinghofer, A. and I.R. Vetter, *Structure-function relationships of the G domain, a canonical switch motif*. Annu Rev Biochem, 2011. **80**: p. 943-71.
28. Lowy, D.R., et al., *Regulation of p21ras activity*. Trends Genet, 1991. **7**(11-12): p. 346-51.
29. Lamontanara, A.J., et al., *The SH2 domain of Abl kinases regulates kinase autophosphorylation by controlling activation loop accessibility*. Nat Commun, 2014. **5**: p. 5470.
30. Cherfils, J. and M. Zeghouf, *Regulation of small GTPases by GEFs, GAPs, and GDIs*. Physiol Rev, 2013. **93**(1): p. 269-309.
31. Geyer, M. and A. Wittinghofer, *GEFs, GAPs, GDIs and effectors: taking a closer (3D) look at the regulation of Ras-related GTP-binding proteins*. Curr Opin Struct Biol, 1997. **7**(6): p. 786-92.
32. Sprang, S.R., *G proteins, effectors and GAPs: structure and mechanism*. Curr Opin Struct Biol, 1997. **7**(6): p. 849-56.
33. Wittinghofer, A., K. Scheffzek, and M.R. Ahmadian, *The interaction of Ras with GTPase-activating proteins*. FEBS Lett, 1997. **410**(1): p. 63-7.
34. Adjei, A.A., *Blocking oncogenic Ras signaling for cancer therapy*. J Natl Cancer Inst, 2001. **93**(14): p. 1062-74.
35. Vigil, D., et al., *Ras superfamily GEFs and GAPs: validated and tractable targets for cancer therapy?* Nat Rev Cancer, 2010. **10**(12): p. 842-57.
36. Schubert, S., K. Shannon, and G. Bollag, *Hyperactive Ras in developmental disorders and cancer*. Nat Rev Cancer, 2007. **7**(4): p. 295-308.
37. Smith, M.J. and M. Ikura, *Integrated RAS signaling defined by parallel NMR detection of effectors and regulators*. Nat Chem Biol, 2014. **10**(3): p. 223-30.
38. Downward, J., *Ras signalling and apoptosis*. Curr Opin Genet Dev, 1998. **8**(1): p. 49-54.
39. Khosravi-Far, R., et al., *Increasing complexity of Ras signal transduction: involvement of Rho family proteins*. Adv Cancer Res, 1998. **72**: p. 57-107.
40. Rojas, A.M., et al., *The Ras protein superfamily: evolutionary tree and role of conserved amino acids*. J Cell Biol, 2012. **196**(2): p. 189-201.

41. Forbes, S.A., et al., *COSMIC: mining complete cancer genomes in the Catalogue of Somatic Mutations in Cancer*. Nucleic Acids Res, 2011. **39**(Database issue): p. D945-50.
42. Karnoub, A.E. and R.A. Weinberg, *Ras oncogenes: split personalities*. Nat Rev Mol Cell Biol, 2008. **9**(7): p. 517-31.
43. Cox, A.D. and C.J. Der, *Ras history: The saga continues*. Small GTPases, 2010. **1**(1): p. 2-27.
44. Takai, Y., T. Sasaki, and T. Matozaki, *Small GTP-binding proteins*. Physiol Rev, 2001. **81**(1): p. 153-208.
45. Bollag, G. and C. Zhang, *Drug discovery: Pocket of opportunity*. Nature, 2013. **503**(7477): p. 475-6.
46. Fanelli, F. and F. Raimondi, *Nucleotide binding affects intrinsic dynamics and structural communication in Ras GTPases*. Curr Pharm Des, 2013. **19**(23): p. 4214-25.
47. Seton-Rogers, S., *Oncogenes: direct hit on mutant RAS*. Nat Rev Cancer, 2014. **14**(1): p. 8-9.
48. Lu, S., et al., *Ras Conformational Ensembles, Allostery, and Signaling*. Chem Rev, 2016. **116**(11): p. 6607-65.
49. de Vos, A.M., et al., *Three-dimensional structure of an oncogene protein: catalytic domain of human c-H-ras p21*. Science, 1988. **239**(4842): p. 888-93.
50. Pai, E.F., et al., *Refined crystal structure of the triphosphate conformation of H-ras p21 at 1.35 Å resolution: implications for the mechanism of GTP hydrolysis*. EMBO J, 1990. **9**(8): p. 2351-9.
51. Milburn, M.V., et al., *Molecular switch for signal transduction: structural differences between active and inactive forms of protooncogenic ras proteins*. Science, 1990. **247**(4945): p. 939-45.
52. Muegge, I., et al., *Electrostatic control of GTP and GDP binding in the oncoprotein p21ras*. Structure, 1996. **4**(4): p. 475-89.
53. Gorfe, A.A., B.J. Grant, and J.A. McCammon, *Mapping the nucleotide and isoform-dependent structural and dynamical features of Ras proteins*. Structure, 2008. **16**(6): p. 885-96.
54. Buhrman, G., et al., *Analysis of binding site hot spots on the surface of Ras GTPase*. J Mol Biol, 2011. **413**(4): p. 773-89.
55. Buhrman, G., et al., *Allosteric modulation of Ras positions Q61 for a direct role in catalysis*. Proc Natl Acad Sci U S A, 2010. **107**(11): p. 4931-6.
56. Stouten, P.F., et al., *How does the switch II region of G-domains work?* FEBS Lett, 1993. **320**(1): p. 1-6.
57. Yan, J., et al., *Ras isoforms vary in their ability to activate Raf-1 and phosphoinositide 3-kinase*. J Biol Chem, 1998. **273**(37): p. 24052-6.
58. Nussinov, R., H. Jang, and C.J. Tsai, *Oligomerization and nanocluster organization render specificity*. Biol Rev Camb Philos Soc, 2015. **90**(2): p. 587-98.
59. Long, S.B., P.J. Casey, and L.S. Beese, *The basis for K-Ras4B binding specificity to protein farnesyltransferase revealed by 2 Å resolution ternary complex structures*. Structure, 2000. **8**(2): p. 209-22.
60. Reid, T.S., et al., *Crystallographic analysis of CaaX prenyltransferases complexed with substrates defines rules of protein substrate selectivity*. J Mol Biol, 2004. **343**(2): p. 417-33.
61. Newman, C.M. and A.I. Magee, *Posttranslational processing of the ras superfamily of small GTP-binding proteins*. Biochim Biophys Acta, 1993. **1155**(1): p. 79-96.

62. Downward, J., *Targeting RAS signalling pathways in cancer therapy*. Nat Rev Cancer, 2003. **3**(1): p. 11-22.
63. Buday, L. and J. Downward, *Many faces of Ras activation*. Biochim Biophys Acta, 2008. **1786**(2): p. 178-87.
64. Shields, J.M., et al., *Understanding Ras: 'it ain't over 'til it's over'*. Trends Cell Biol, 2000. **10**(4): p. 147-54.
65. Willumsen, B.M., et al., *The p21 ras C-terminus is required for transformation and membrane association*. Nature, 1984. **310**(5978): p. 583-6.
66. Wright, L.P. and M.R. Philips, *Thematic review series: lipid posttranslational modifications. CAAX modification and membrane targeting of Ras*. J Lipid Res, 2006. **47**(5): p. 883-91.
67. Chiu, V.K., et al., *Carboxyl methylation of Ras regulates membrane targeting and effector engagement*. J Biol Chem, 2004. **279**(8): p. 7346-52.
68. Laude, A.J. and I.A. Prior, *Palmitoylation and localisation of RAS isoforms are modulated by the hypervariable linker domain*. J Cell Sci, 2008. **121**(Pt 4): p. 421-7.
69. Roy, S., et al., *Individual palmitoyl residues serve distinct roles in H-ras trafficking, microlocalization, and signaling*. Mol Cell Biol, 2005. **25**(15): p. 6722-33.
70. Roy, S., et al., *Dominant-negative caveolin inhibits H-Ras function by disrupting cholesterol-rich plasma membrane domains*. Nat Cell Biol, 1999. **1**(2): p. 98-105.
71. Matallanas, D., et al., *Differences on the inhibitory specificities of H-Ras, K-Ras, and N-Ras (N17) dominant negative mutants are related to their membrane microlocalization*. J Biol Chem, 2003. **278**(7): p. 4572-81.
72. Prior, I.A., et al., *GTP-dependent segregation of H-ras from lipid rafts is required for biological activity*. Nat Cell Biol, 2001. **3**(4): p. 368-75.
73. Prior, I.A., et al., *Direct visualization of Ras proteins in spatially distinct cell surface microdomains*. J Cell Biol, 2003. **160**(2): p. 165-70.
74. McLaughlin, S., et al., *Reversible - through calmodulin - electrostatic interactions between basic residues on proteins and acidic lipids in the plasma membrane*. Biochem Soc Symp, 2005(72): p. 189-98.
75. Bivona, T.G., et al., *PKC regulates a farnesyl-electrostatic switch on K-Ras that promotes its association with Bcl-XL on mitochondria and induces apoptosis*. Mol Cell, 2006. **21**(4): p. 481-93.
76. Plowman, S.J. and J.F. Hancock, *Ras signaling from plasma membrane and endomembrane microdomains*. Biochim Biophys Acta, 2005. **1746**(3): p. 274-83.
77. van den Bogaart, G., et al., *Membrane protein sequestering by ionic protein-lipid interactions*. Nature, 2011. **479**(7374): p. 552-5.
78. Zhou, Y. and J.F. Hancock, *Ras nanoclusters: Versatile lipid-based signaling platforms*. Biochim Biophys Acta, 2015. **1853**(4): p. 841-9.
79. Zhou, Y., et al., *Signal integration by lipid-mediated spatial cross talk between Ras nanoclusters*. Mol Cell Biol, 2014. **34**(5): p. 862-76.
80. Ghosh, S. and R.M. Bell, *Regulation of Raf-1 kinase by interaction with the lipid second messenger, phosphatidic acid*. Biochem Soc Trans, 1997. **25**(2): p. 561-5.
81. Ehrhardt, A., et al., *Distinct mechanisms determine the patterns of differential activation of H-Ras, N-Ras, K-Ras 4B, and M-Ras by receptors for growth factors or antigen*. Mol Cell Biol, 2004. **24**(14): p. 6311-23.
82. Willumsen, B.M., et al., *Harvey murine sarcoma virus p21 ras protein: biological and biochemical significance of the cysteine nearest the carboxy terminus*. EMBO J, 1984. **3**(11): p. 2581-5.

83. Trahey, M. and F. McCormick, *A cytoplasmic protein stimulates normal N-ras p21 GTPase, but does not affect oncogenic mutants*. *Science*, 1987. **238**(4826): p. 542-5.
84. Seabra, M.C., *Membrane association and targeting of prenylated Ras-like GTPases*. *Cell Signal*, 1998. **10**(3): p. 167-72.
85. Lowy, D.R. and B.M. Willumsen, *Function and regulation of ras*. *Annu Rev Biochem*, 1993. **62**: p. 851-91.
86. Sprang, S.R., *How Ras works: structure of a Rap-Raf complex*. *Structure*, 1995. **3**(7): p. 641-3.
87. Vetter, I.R. and A. Wittinghofer, *The guanine nucleotide-binding switch in three dimensions*. *Science*, 2001. **294**(5545): p. 1299-304.
88. Ray, A., N. Jatana, and L. Thukral, *Lipidated proteins: Spotlight on protein-membrane binding interfaces*. *Prog Biophys Mol Biol*, 2017: p. DOI: 10.1016/j.pbiomolbio.2017.01.002.
89. Schmick, M., et al., *KRas localizes to the plasma membrane by spatial cycles of solubilization, trapping and vesicular transport*. *Cell*, 2014. **157**(2): p. 459-71.
90. Lynch, S.J., et al., *The differential palmitoylation states of N-Ras and H-Ras determine their distinct Golgi subcompartment localizations*. *J Cell Physiol*, 2015. **230**(3): p. 610-9.
91. Apolloni, A., et al., *H-ras but not K-ras traffics to the plasma membrane through the exocytic pathway*. *Mol Cell Biol*, 2000. **20**(7): p. 2475-87.
92. Tsai, F.D., et al., *K-Ras4A splice variant is widely expressed in cancer and uses a hybrid membrane-targeting motif*. *Proc Natl Acad Sci U S A*, 2015. **112**(3): p. 779-84.
93. Zhang, H., et al., *Photoreceptor cGMP phosphodiesterase delta subunit (PDEdelta) functions as a prenyl-binding protein*. *J Biol Chem*, 2004. **279**(1): p. 407-13.
94. Hanzal-Bayer, M., et al., *The complex of Arl2-GTP and PDE delta: from structure to function*. *EMBO J*, 2002. **21**(9): p. 2095-106.
95. Nancy, V., et al., *The delta subunit of retinal rod cGMP phosphodiesterase regulates the membrane association of Ras and Rap GTPases*. *J Biol Chem*, 2002. **277**(17): p. 15076-84.
96. Chen, Y.X., et al., *Synthesis of the Rheb and K-Ras4B GTPases*. *Angew Chem Int Ed Engl*, 2010. **49**(35): p. 6090-5.
97. Dharmaiah, S., et al., *Structural basis of recognition of farnesylated and methylated KRAS4b by PDEdelta*. *Proc Natl Acad Sci U S A*, 2016. **113**(44): p. E6766-E6775.
98. Chandra, A., et al., *The GDI-like solubilizing factor PDEdelta sustains the spatial organization and signalling of Ras family proteins*. *Nat Cell Biol*, 2011. **14**(2): p. 148-58.
99. Weise, K., et al., *Dissociation of the K-Ras4B/PDEdelta complex upon contact with lipid membranes: membrane delivery instead of extraction*. *J Am Chem Soc*, 2012. **134**(28): p. 11503-10.
100. Wu, S.K., et al., *Structural insights into the function of the Rab GDI superfamily*. *Trends Biochem Sci*, 1996. **21**(12): p. 472-6.
101. Hoffman, G.R., N. Nassar, and R.A. Cerione, *Structure of the Rho family GTP-binding protein Cdc42 in complex with the multifunctional regulator RhoGDI*. *Cell*, 2000. **100**(3): p. 345-56.
102. Linari, M., M. Hanzal-Bayer, and J. Becker, *The delta subunit of rod specific cyclic GMP phosphodiesterase, PDE delta, interacts with the Arf-like protein Arl3 in a GTP specific manner*. *FEBS Lett*, 1999. **458**(1): p. 55-9.

103. Veltel, S., et al., *Specificity of Arl2/Arl3 signaling is mediated by a ternary Arl3-effector-GAP complex*. FEBS Lett, 2008. **582**(17): p. 2501-7.
104. Gosser, Y.Q., et al., *C-terminal binding domain of Rho GDP-dissociation inhibitor directs N-terminal inhibitory peptide to GTPases*. Nature, 1997. **387**(6635): p. 814-9.
105. Scheffzek, K., et al., *The Rac-RhoGDI complex and the structural basis for the regulation of Rho proteins by RhoGDI*. Nat Struct Biol, 2000. **7**(2): p. 122-6.
106. Ismail, S.A., et al., *Arl2-GTP and Arl3-GTP regulate a GDI-like transport system for farnesylated cargo*. Nat Chem Biol, 2011. **7**(12): p. 942-9.
107. Wittinghofer, A. and C. Herrmann, *Ras-effector interactions, the problem of specificity*. FEBS Lett, 1995. **369**(1): p. 52-6.
108. Marshall, C.J., *Ras effectors*. Curr Opin Cell Biol, 1996. **8**(2): p. 197-204.
109. McCormick, F. and A. Wittinghofer, *Interactions between Ras proteins and their effectors*. Curr Opin Biotechnol, 1996. **7**(4): p. 449-56.
110. Koide, H., et al., *GTP-dependent association of Raf-1 with Ha-Ras: identification of Raf as a target downstream of Ras in mammalian cells*. Proc Natl Acad Sci U S A, 1993. **90**(18): p. 8683-6.
111. Spoerner, M., et al., *Dynamic properties of the Ras switch I region and its importance for binding to effectors*. Proc Natl Acad Sci U S A, 2001. **98**(9): p. 4944-9.
112. Herrmann, C., G.A. Martin, and A. Wittinghofer, *Quantitative analysis of the complex between p21ras and the Ras-binding domain of the human Raf-1 protein kinase*. J Biol Chem, 1995. **270**(7): p. 2901-5.
113. Mott, H.R. and D. Owen, *Structures of Ras superfamily effector complexes: What have we learnt in two decades?* Crit Rev Biochem Mol Biol, 2015. **50**(2): p. 85-133.
114. Kolch, W., *Meaningful relationships: the regulation of the Ras/Raf/MEK/ERK pathway by protein interactions*. Biochem J, 2000. **351 Pt 2**: p. 289-305.
115. Roskoski, R., Jr., *RAF protein-serine/threonine kinases: structure and regulation*. Biochem Biophys Res Commun, 2010. **399**(3): p. 313-7.
116. Vojtek, A.B., S.M. Hollenberg, and J.A. Cooper, *Mammalian Ras interacts directly with the serine/threonine kinase Raf*. Cell, 1993. **74**(1): p. 205-14.
117. Chuang, E., et al., *Critical binding and regulatory interactions between Ras and Raf occur through a small, stable N-terminal domain of Raf and specific Ras effector residues*. Mol Cell Biol, 1994. **14**(8): p. 5318-25.
118. Ghosh, S. and R.M. Bell, *Identification of discrete segments of human Raf-1 kinase critical for high affinity binding to Ha-Ras*. J Biol Chem, 1994. **269**(49): p. 30785-8.
119. Gohlke, H., C. Kiel, and D.A. Case, *Insights into protein-protein binding by binding free energy calculation and free energy decomposition for the Ras-Raf and Ras-RalGDS complexes*. J Mol Biol, 2003. **330**(4): p. 891-913.
120. Fetics, S.K., et al., *Allosteric effects of the oncogenic RasQ61L mutant on Raf-RBD*. Structure, 2015. **23**(3): p. 505-16.
121. Castellano, E. and J. Downward, *RAS Interaction with PI3K: More Than Just Another Effector Pathway*. Genes Cancer, 2011. **2**(3): p. 261-74.
122. Zhao, Y., et al., *Crystal Structures of PI3Kalpha Complexed with P1103 and Its Derivatives: New Directions for Inhibitors Design*. ACS Med Chem Lett, 2014. **5**(2): p. 138-42.
123. Huang, C.H., et al., *The structure of a human p110alpha/p85alpha complex elucidates the effects of oncogenic PI3Kalpha mutations*. Science, 2007. **318**(5857): p. 1744-8.
124. Fritsch, R., et al., *RAS and RHO families of GTPases directly regulate distinct phosphoinositide 3-kinase isoforms*. Cell, 2013. **153**(5): p. 1050-63.

125. Rubio, I., et al., *Interaction of Ras with phosphoinositide 3-kinase gamma*. *Biochem J*, 1997. **326** (Pt 3): p. 891-5.
126. Vanhaesebroeck, B., et al., *P110delta, a novel phosphoinositide 3-kinase in leukocytes*. *Proc Natl Acad Sci U S A*, 1997. **94**(9): p. 4330-5.
127. Zhao, L. and P.K. Vogt, *Helical domain and kinase domain mutations in p110alpha of phosphatidylinositol 3-kinase induce gain of function by different mechanisms*. *Proc Natl Acad Sci U S A*, 2008. **105**(7): p. 2652-7.
128. Pacold, M.E., et al., *Crystal structure and functional analysis of Ras binding to its effector phosphoinositide 3-kinase gamma*. *Cell*, 2000. **103**(6): p. 931-43.
129. Lukman, S., et al., *The distinct conformational dynamics of K-Ras and H-Ras A59G*. *PLoS Comput Biol*, 2010. **6**(9).
130. Villalonga, P., et al., *Calmodulin binds to K-Ras, but not to H- or N-Ras, and modulates its downstream signaling*. *Mol Cell Biol*, 2001. **21**(21): p. 7345-54.
131. Abraham, S.J., et al., *The hypervariable region of K-Ras4B is responsible for its specific interactions with calmodulin*. *Biochemistry*, 2009. **48**(32): p. 7575-83.
132. Chavan, T.S., S. Abraham, and V. Gaponenko, *Application of reductive (1)(3)C-methylation of lysines to enhance the sensitivity of conventional NMR methods*. *Molecules*, 2013. **18**(6): p. 7103-19.
133. Joyal, J.L., et al., *Calmodulin activates phosphatidylinositol 3-kinase*. *J Biol Chem*, 1997. **272**(45): p. 28183-6.
134. Liao, J., et al., *Growth factor-dependent AKT activation and cell migration requires the function of c-K(B)-Ras versus other cellular ras isoforms*. *J Biol Chem*, 2006. **281**(40): p. 29730-8.
135. Liao, J., J.C. Wolfman, and A. Wolfman, *K-ras regulates the steady-state expression of matrix metalloproteinase 2 in fibroblasts*. *J Biol Chem*, 2003. **278**(34): p. 31871-8.
136. Bosch, M., et al., *Calmodulin inhibitor W13 induces sustained activation of ERK2 and expression of p21(cip1)*. *J Biol Chem*, 1998. **273**(34): p. 22145-50.
137. Lopez-Alcala, C., et al., *Identification of essential interacting elements in K-Ras/calmodulin binding and its role in K-Ras localization*. *J Biol Chem*, 2008. **283**(16): p. 10621-31.
138. Fivaz, M. and T. Meyer, *Reversible intracellular translocation of KRas but not HRas in hippocampal neurons regulated by Ca²⁺/calmodulin*. *J Cell Biol*, 2005. **170**(3): p. 429-41.
139. Nussinov, R., et al., *The Key Role of Calmodulin in KRAS-Driven Adenocarcinomas*. *Mol Cancer Res*, 2015. **13**(9): p. 1265-73.
140. Xu, Y., et al., *Emerging roles of the p38 MAPK and PI3K/AKT/mTOR pathways in oncogene-induced senescence*. *Trends Biochem Sci*, 2014. **39**(6): p. 268-76.
141. Nandan, M.O. and V.W. Yang, *An Update on the Biology of RAS/RAF Mutations in Colorectal Cancer*. *Curr Colorectal Cancer Rep*, 2011. **7**(2): p. 113-120.
142. Courtney, K.D., R.B. Corcoran, and J.A. Engelman, *The PI3K pathway as drug target in human cancer*. *J Clin Oncol*, 2010. **28**(6): p. 1075-83.
143. Vivanco, I. and C.L. Sawyers, *The phosphatidylinositol 3-Kinase AKT pathway in human cancer*. *Nat Rev Cancer*, 2002. **2**(7): p. 489-501.
144. Castellano, E. and J. Downward, *Role of RAS in the regulation of PI 3-kinase*. *Curr Top Microbiol Immunol*, 2010. **346**: p. 143-69.
145. Rajakulendran, T., et al., *A dimerization-dependent mechanism drives RAF catalytic activation*. *Nature*, 2009. **461**(7263): p. 542-5.

146. Freeman, A.K., D.A. Ritt, and D.K. Morrison, *The importance of Raf dimerization in cell signaling*. Small GTPases, 2013. **4**(3): p. 180-5.
147. Lavoie, H., et al., *Inhibitors that stabilize a closed RAF kinase domain conformation induce dimerization*. Nat Chem Biol, 2013. **9**(7): p. 428-36.
148. Marais, R., et al., *Ras recruits Raf-1 to the plasma membrane for activation by tyrosine phosphorylation*. EMBO J, 1995. **14**(13): p. 3136-45.
149. Avruch, J., et al., *Ras activation of the Raf kinase: tyrosine kinase recruitment of the MAP kinase cascade*. Recent Prog Horm Res, 2001. **56**: p. 127-55.
150. Domchek, S.M., et al., *Inhibition of SH2 domain/phosphoprotein association by a nonhydrolyzable phosphonopeptide*. Biochemistry, 1992. **31**(41): p. 9865-70.
151. Pawson, T., *Specificity in signal transduction: from phosphotyrosine-SH2 domain interactions to complex cellular systems*. Cell, 2004. **116**(2): p. 191-203.
152. Ong, S.H., et al., *Stimulation of phosphatidylinositol 3-kinase by fibroblast growth factor receptors is mediated by coordinated recruitment of multiple docking proteins*. Proc Natl Acad Sci U S A, 2001. **98**(11): p. 6074-9.
153. Cantley, L.C., *The phosphoinositide 3-kinase pathway*. Science, 2002. **296**(5573): p. 1655-7.
154. Alessi, D.R., et al., *Characterization of a 3-phosphoinositide-dependent protein kinase which phosphorylates and activates protein kinase Balpha*. Curr Biol, 1997. **7**(4): p. 261-9.
155. Jambrina, P.G., et al., *Molecular mechanisms of asymmetric RAF dimer activation*. Biochem Soc Trans, 2014. **42**(4): p. 784-90.
156. Inouye, K., et al., *Formation of the Ras dimer is essential for Raf-1 activation*. J Biol Chem, 2000. **275**(6): p. 3737-40.
157. Nussinov, R., et al., *Principles of K-Ras effector organization and the role of oncogenic K-Ras in cancer initiation through G1 cell cycle deregulation*. Expert Rev Proteomics, 2015. **12**(6): p. 669-82.
158. Nan, X., et al., *Ras-GTP dimers activate the Mitogen-Activated Protein Kinase (MAPK) pathway*. Proc Natl Acad Sci U S A, 2015. **112**(26): p. 7996-8001.
159. Philips, M.R. and C.J. Der, *Seeing is believing: Ras dimers observed in live cells*. Proc Natl Acad Sci U S A, 2015. **112**(32): p. 9793-4.
160. Prakash, P., et al., *Computational and biochemical characterization of two partially overlapping interfaces and multiple weak-affinity K-Ras dimers*. Sci Rep, 2017. **7**: p. 40109.
161. Spencer-Smith, R., et al., *Inhibition of RAS function through targeting an allosteric regulatory site*. Nat Chem Biol, 2017. **13**(1): p. 62-68.
162. Woolf, P.J. and J.J. Linderman, *Self organization of membrane proteins via dimerization*. Biophys Chem, 2003. **104**(1): p. 217-27.
163. Abankwa, D., et al., *Ras membrane orientation and nanodomain localization generate isoform diversity*. Proc Natl Acad Sci U S A, 2010. **107**(3): p. 1130-5.
164. Murakoshi, H., et al., *Single-molecule imaging analysis of Ras activation in living cells*. Proc Natl Acad Sci U S A, 2004. **101**(19): p. 7317-22.
165. Plowman, S.J., et al., *H-ras, K-ras, and inner plasma membrane raft proteins operate in nanoclusters with differential dependence on the actin cytoskeleton*. Proc Natl Acad Sci U S A, 2005. **102**(43): p. 15500-5.
166. Hibino, K., et al., *Single- and multiple-molecule dynamics of the signaling from H-Ras to cRaf-1 visualized on the plasma membrane of living cells*. Chemphyschem, 2003. **4**(7): p. 748-53.

167. Janosi, L., et al., *Organization, dynamics, and segregation of Ras nanoclusters in membrane domains*. Proc Natl Acad Sci U S A, 2012. **109**(21): p. 8097-102.
168. Bader, A.N., et al., *Homo-FRET imaging as a tool to quantify protein and lipid clustering*. Chemphyschem, 2011. **12**(3): p. 475-83.
169. Kearney, B.M., et al., *DRoP: a water analysis program identifies Ras-GTP-specific pathway of communication between membrane-interacting regions and the active site*. J Mol Biol, 2014. **426**(3): p. 611-29.
170. Shalom-Feuerstein, R., et al., *K-ras nanoclustering is subverted by overexpression of the scaffold protein galectin-3*. Cancer Res, 2008. **68**(16): p. 6608-16.
171. Harding, A., et al., *Identification of residues and domains of Raf important for function in vivo and in vitro*. J Biol Chem, 2003. **278**(46): p. 45519-27.
172. Zhu, J., et al., *Identification of Raf-1 S471 as a novel phosphorylation site critical for Raf-1 and B-Raf kinase activities and for MEK binding*. Mol Biol Cell, 2005. **16**(10): p. 4733-44.
173. Terai, K. and M. Matsuda, *Ras binding opens c-Raf to expose the docking site for mitogen-activated protein kinase kinase*. EMBO Rep, 2005. **6**(3): p. 251-5.
174. Rotblat, B., et al., *H-Ras nanocluster stability regulates the magnitude of MAPK signal output*. PLoS One, 2010. **5**(8): p. e11991.
175. Tian, T., et al., *Mathematical modeling of K-Ras nanocluster formation on the plasma membrane*. Biophys J, 2010. **99**(2): p. 534-43.
176. Cho, K.J. and J.F. Hancock, *Ras nanoclusters: a new drug target?* Small GTPases, 2013. **4**(1): p. 57-60.
177. Tian, T., et al., *Plasma membrane nanoswitches generate high-fidelity Ras signal transduction*. Nat Cell Biol, 2007. **9**(8): p. 905-14.
178. Zhou, Y., et al., *SIGNAL TRANSDUCTION. Membrane potential modulates plasma membrane phospholipid dynamics and K-Ras signaling*. Science, 2015. **349**(6250): p. 873-6.
179. Harding, A. and J.F. Hancock, *Ras nanoclusters: combining digital and analog signaling*. Cell Cycle, 2008. **7**(2): p. 127-34.
180. Cho, K.J., et al., *Raf inhibitors target ras spatiotemporal dynamics*. Curr Biol, 2012. **22**(11): p. 945-55.
181. Barbacid, M., *ras genes*. Annu Rev Biochem, 1987. **56**: p. 779-827.
182. Bos, J.L., *ras oncogenes in human cancer: a review*. Cancer Res, 1989. **49**(17): p. 4682-9.
183. Aytuna, A.S., A. Gursoy, and O. Keskin, *Prediction of protein-protein interactions by combining structure and sequence conservation in protein interfaces*. Bioinformatics, 2005. **21**(12): p. 2850-5.
184. Ogmen, U., et al., *PRISM: protein interactions by structural matching*. Nucleic Acids Res, 2005. **33**(Web Server issue): p. W331-6.
185. Tuncbag, N., et al., *Predicting protein-protein interactions on a proteome scale by matching evolutionary and structural similarities at interfaces using PRISM*. Nat Protoc, 2011. **6**(9): p. 1341-54.
186. Mashlach, E., R. Nussinov, and H.J. Wolfson, *FiberDock: Flexible induced-fit backbone refinement in molecular docking*. Proteins, 2010. **78**(6): p. 1503-19.
187. Tuncbag, N., et al., *Fast and accurate modeling of protein-protein interactions by combining template-interface-based docking with flexible refinement*. Proteins, 2012. **80**(4): p. 1239-49.

188. Cukuroglu, E., A. GURSOY, and O. Keskin, *HotRegion: a database of predicted hot spot clusters*. Nucleic Acids Res, 2012. **40**(Database issue): p. D829-33.
189. Duarte, J.M., et al., *Protein interface classification by evolutionary analysis*. BMC Bioinformatics, 2012. **13**: p. 334.
190. Van Durme, J., et al., *A graphical interface for the FoldX forcefield*. Bioinformatics, 2011. **27**(12): p. 1711-2.
191. Zhang, Y., *I-TASSER server for protein 3D structure prediction*. BMC Bioinformatics, 2008. **9**: p. 40.
192. Brooks, B.R., et al., *CHARMM: the biomolecular simulation program*. J Comput Chem, 2009. **30**(10): p. 1545-614.
193. Klauda, J.B., et al., *Update of the CHARMM all-atom additive force field for lipids: validation on six lipid types*. J Phys Chem B, 2010. **114**(23): p. 7830-43.
194. Chavan, T.S., et al., *High-affinity interaction of the K-Ras4B hypervariable region with the Ras active site*. Biophys J, 2015. **109**: p. 2602-13.
195. Jang, H., et al., *Mechanisms of membrane binding of small GTPase K-Ras4B farnesylated hypervariable region*. J Biol Chem, 2015. **290**(15): p. 9465-77.
196. Nussinov, R., et al., *A New View of Ras Isoforms in Cancers*. Cancer Res, 2016. **76**(1): p. 18-23.
197. Jang, H., et al., *Membrane-associated Ras dimers are isoform-specific: K-Ras dimers differ from H-Ras dimers*. Biochem J, 2016. **473**(12): p. 1719-32.
198. Lu, S., et al., *GTP Binding and Oncogenic Mutations May Attenuate Hypervariable Region (HVR)-Catalytic Domain Interactions in Small GTPase K-Ras4B, Exposing the Effector Binding Site*. J Biol Chem, 2015. **290**(48): p. 28887-900.
199. Durell, S.R., B.R. Brooks, and A. Bennaïm, *Solvent-induced forces between two hydrophilic groups*. J. Phys. Chem., 1994. **98**: p. 2198-2202.
200. Phillips, J.C., et al., *Scalable molecular dynamics with NAMD*. J Comput Chem, 2005. **26**(16): p. 1781-802.
201. Onufriev, A., D. Bashford, and D.A. Case, *Exploring protein native states and large-scale conformational changes with a modified generalized born model*. Proteins, 2004. **55**(2): p. 383-94.
202. Hornak, V., et al., *Comparison of multiple Amber force fields and development of improved protein backbone parameters*. Proteins, 2006. **65**(3): p. 712-25.
203. Kar, G., et al., *Human proteome-scale structural modeling of E2-E3 interactions exploiting interface motifs*. J Proteome Res, 2012. **11**(2): p. 1196-207.
204. Acuner Ozbabacan, S.E., et al., *Enriching the human apoptosis pathway by predicting the structures of protein-protein complexes*. J Struct Biol, 2012. **179**(3): p. 338-46.
205. Kuzu, G., et al., *Exploiting conformational ensembles in modeling protein-protein interactions on the proteome scale*. J Proteome Res, 2013. **12**(6): p. 2641-53.
206. Muratcioglu, S., et al., *GTP-Dependent K-Ras Dimerization*. Structure, 2015. **23**(7): p. 1325-35.
207. Frank, A.O., et al., *Discovery of a potent inhibitor of replication protein a protein-protein interactions using a fragment-linking approach*. Journal of medicinal chemistry, 2013. **56**(22): p. 9242-50.
208. Harner, M.J., A.O. Frank, and S.W. Fesik, *Fragment-based drug discovery using NMR spectroscopy*. Journal of biomolecular NMR, 2013. **56**(2): p. 65-75.
209. Davis, M.J. and J. Schlessinger, *The genesis of Zelboraf: targeting mutant B-Raf in melanoma*. The Journal of cell biology, 2012. **199**(1): p. 15-9.

210. Ostrem, J.M., et al., *K-Ras(G12C) inhibitors allosterically control GTP affinity and effector interactions*. Nature, 2013. **503**(7477): p. 548-51.
211. Jang, H., et al., *The higher level of complexity of K-Ras4B activation at the membrane*. FASEB J, 2016. **30**(4): p. 1643-55.
212. Gabdoulline, R.R. and R.C. Wade, *On the protein-protein diffusional encounter complex*. J Mol Recognit, 1999. **12**(4): p. 226-34.
213. Sheinerman, F.B., R. Norel, and B. Honig, *Electrostatic aspects of protein-protein interactions*. Curr Opin Struct Biol, 2000. **10**(2): p. 153-9.
214. Dhillon, A.S., et al., *MAP kinase signalling pathways in cancer*. Oncogene, 2007. **26**(22): p. 3279-90.
215. Fambrough, D., et al., *Diverse signaling pathways activated by growth factor receptors induce broadly overlapping, rather than independent, sets of genes*. Cell, 1999. **97**(6): p. 727-41.
216. Whitmarsh, A.J., et al., *Integration of MAP kinase signal transduction pathways at the serum response element*. Science, 1995. **269**(5222): p. 403-7.
217. Greenberg, M.E., L.A. Greene, and E.B. Ziff, *Nerve growth factor and epidermal growth factor induce rapid transient changes in proto-oncogene transcription in PC12 cells*. J Biol Chem, 1985. **260**(26): p. 14101-10.
218. Cruzalegui, F.H., E. Cano, and R. Treisman, *ERK activation induces phosphorylation of Elk-1 at multiple S/T-P motifs to high stoichiometry*. Oncogene, 1999. **18**(56): p. 7948-57.
219. Morton, S., et al., *A reinvestigation of the multisite phosphorylation of the transcription factor c-Jun*. EMBO J, 2003. **22**(15): p. 3876-86.
220. Pulverer, B.J., et al., *Phosphorylation of c-jun mediated by MAP kinases*. Nature, 1991. **353**(6345): p. 670-4.
221. Morton, S., R.J. Davis, and P. Cohen, *Signalling pathways involved in multisite phosphorylation of the transcription factor ATF-2*. FEBS Lett, 2004. **572**(1-3): p. 177-83.
222. Han, T.H., W.W. Lamph, and R. Prywes, *Mapping of epidermal growth factor-, serum-, and phorbol ester-responsive sequence elements in the c-jun promoter*. Mol Cell Biol, 1992. **12**(10): p. 4472-7.
223. Angel, P., et al., *The jun proto-oncogene is positively autoregulated by its product, Jun/AP-1*. Cell, 1988. **55**(5): p. 875-85.
224. Essafi, A., et al., *Direct transcriptional regulation of Bim by FoxO3a mediates STI571-induced apoptosis in Bcr-Abl-expressing cells*. Oncogene, 2005. **24**(14): p. 2317-29.
225. Yang, J.Y., et al., *ERK promotes tumorigenesis by inhibiting FOXO3a via MDM2-mediated degradation*. Nat Cell Biol, 2008. **10**(2): p. 138-48.
226. Akiyama, T., C.R. Dass, and P.F. Choong, *Bim-targeted cancer therapy: a link between drug action and underlying molecular changes*. Mol Cancer Ther, 2009. **8**(12): p. 3173-80.
227. Rodriguez-Viciano, P., C. Sabatier, and F. McCormick, *Signaling specificity by Ras family GTPases is determined by the full spectrum of effectors they regulate*. Mol Cell Biol, 2004. **24**(11): p. 4943-54.
228. Bauvois, B., *New facets of matrix metalloproteinases MMP-2 and MMP-9 as cell surface transducers: outside-in signaling and relationship to tumor progression*. Biochim Biophys Acta, 2012. **1825**(1): p. 29-36.

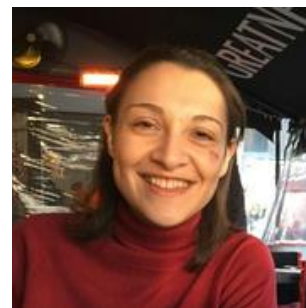
229. Vadas, O., et al., *Structural basis for activation and inhibition of class I phosphoinositide 3-kinases*. *Sci Signal*, 2011. **4**(195): p. re2.
230. Sydor, J.R., et al., *Transient kinetic studies on the interaction of Ras and the Ras-binding domain of c-Raf-1 reveal rapid equilibration of the complex*. *Biochemistry*, 1998. **37**(40): p. 14292-9.
231. Herrmann, C., et al., *Differential interaction of the ras family GTP-binding proteins H-Ras, Rap1A, and R-Ras with the putative effector molecules Raf kinase and Ral-guanine nucleotide exchange factor*. *J Biol Chem*, 1996. **271**(12): p. 6794-800.
232. Kilambi, K.P., et al., *Extending RosettaDock with water, sugar, and pH for prediction of complex structures and affinities for CAPRI rounds 20-27*. *Proteins*, 2013. **81**(12): p. 2201-9.
233. Adams, P.D., et al., *Advances, interactions, and future developments in the CNS, Phenix, and Rosetta structural biology software systems*. *Annu Rev Biophys*, 2013. **42**: p. 265-87.
234. Muratcioglu, S., et al., *PDEdelta Binding to Ras Isoforms Provides a Route to Proper Membrane Localization*. *J Phys Chem B*, 2017.
235. Chen, M., et al., *Ras Dimer Formation as a New Signaling Mechanism and Potential Cancer Therapeutic Target*. *Mini Rev Med Chem*, 2016. **16**(5): p. 391-403.
236. Prakash, P., et al., *Oncogenic K-Ras Binds to an Anionic Membrane in Two Distinct Orientations: A Molecular Dynamics Analysis*. *Biophys J*, 2016. **110**(5): p. 1125-38.
237. Banerjee, A., et al., *The disordered hypervariable region and the folded catalytic domain of oncogenic K-Ras4B partner in phospholipid binding*. *Curr Opin Struct Biol*, 2016. **36**: p. 10-7.
238. Li, Z.L. and M. Buck, *Computational Modeling Reveals that Signaling Lipids Modulate the Orientation of K-Ras4A at the Membrane Reflecting Protein Topology*. *Structure*, 2017. **25**(4): p. 679-689 e2.
239. Erwin, N., et al., *Influence of isoform-specific Ras lipidation motifs on protein partitioning and dynamics in model membrane systems of various complexity*. *Biol Chem*, 2017. **398**(5-6): p. 547-563.
240. Liao, T.J., et al., *RASSF5: An MST activator and tumor suppressor in vivo but opposite in vitro*. *Curr Opin Struct Biol*, 2016. **41**: p. 217-224.
241. Donninger, H., et al., *Ras signaling through RASSF proteins*. *Semin Cell Dev Biol*, 2016. **58**: p. 86-95.
242. Spiegel, J., et al., *Small-molecule modulation of Ras signaling*. *Nat Chem Biol*, 2014. **10**(8): p. 613-22.
243. Chakrabarti, M., H. Jang, and R. Nussinov, *Comparison of the Conformations of KRAS Isoforms, K-Ras4A and K-Ras4B, Points to Similarities and Significant Differences*. *J Phys Chem B*, 2016. **120**(4): p. 667-79.
244. Nussinov, R., et al., *Calmodulin and PI3K Signaling in KRAS Cancers*. *Trends Cancer*, 2017. **3**(3): p. 214-224.
245. Nussinov, R. and P.G. Wolynes, *A second molecular biology revolution? The energy landscapes of biomolecular function*. *Phys Chem Chem Phys*, 2014. **16**(14): p. 6321-2.

VITA

Serena Muratcioğlu was born in Istanbul, Turkey, on November 16, 1987. She received her dual bachelor's degrees in Chemistry and Molecular Biology and Genetics in 2011 and 2012, respectively, at Istanbul Technical University. She received her Ph.D. Degree from Koç University in Chemical and Biological Engineering in 2017. From September 2012 to August 2017 she worked as a teaching and research assistant at Koç University. She studied as a guest researcher in National Cancer Institute (NCI), NIH.

Her research interests lie in the area of computational and experimental biology, particularly on protein-protein interactions and signaling. She has been studying a protein called Ras. She has published articles in prestigious journals such as Structure, Biophysical Journal, Molecular Cancer Research, Current Opinion in Structural Biology and Journal of Physical Chemistry.

CURRICULUM VITAE



SERENA MURATCIOĞLU

Koc University
Department of Chemical and Biological Engineering
Rumelifeneri Yolu, Sariyer 34450
Istanbul, TURKEY

Mobile Phone: +90 537 718 9925
E-mail: smuratcioglu@ku.edu.tr

EDUCATION

Koç University Istanbul, Turkey
PhD, Chemical and Biological Engineering January 2018
Dissertation: Computational and Experimental Investigation of Ras Homodimer Formation,
Ras-effector Interactions and Ras Shuttling

Istanbul Technical University Istanbul, Turkey
BS, Molecular Biology and Genetics January 2012
BS, Chemistry June 2011

GRANTS AND AWARDS

The Scientific and Technological Research Council of Turkey (TUBITAK) 1001 (Scientific and Technological Research Projects Funding Program), 2014-Present

Koç University Graduate Student Travel Award for oral presentation at The International Symposium on Health Informatics and Bioinformatics, (HIBIT), METU Northern Cyprus Campus, Northern Cyprus, 2017.

Koç University Graduate Student Travel Award for Workshop on Integrative Modeling and Simulations, University of California San Francisco, San Francisco, CA, December, 2016.

TUBITAK BİDEB 2224-B (Scientific Meetings Grant Programs)-for presenting at the 9th International Symposium on Health Informatics and Bioinformatics HIBIT 2015, Muğla, October, 2015.

Koç University Graduate Student Travel Award for presenting at ISMB/ECCB 2015, Dublin, July, 2015.

COST Action: CM1306 Travel Award for presenting at the International Symposium - Integrating spectroscopic and theoretical methods to analyse molecular machines, Germany, December, 2014.

TUBITAK BİDEB 2224-B (Scientific Meetings Grant Programs)-for presenting at the Modeling of Biomolecular Systems Interactions, Dynamics, and Allostery: Bridging Experiments and Computations held in Istanbul, Turkey, 2014.

Koç University Graduate Student Travel Award for presenting at the Intelligent Systems for Molecular Biology (ISMB) conference held in Boston, MA, 2014.

RESEARCH EXPERIENCE

Koç University

Istanbul, Turkey

Research Assistant; Advisors: Özlem Keskin & Attila Gürsoy 2012-Present

Molecular Dynamics (MD) simulations of Ras/PDE δ complexes

- Performed MD simulations to gain insight into how Ras proteins (N-Ras, K-Ras4A and K-Ras4B) interact with PDE δ , a chaperone participating in intracellular trafficking of Ras.
- Analyzed the interfaces in detail to identify the similarities/differences among the isoforms.
- Calculated the binding free energies using the MM-GBSA method.

Computational studies on H- and K-Ras dimerization and Ras-effector interactions.

- Predicted the dimeric structures of H-Ras and K-Ras4B proteins using a template-based prediction algorithm, PRISM, developed by our group.
- Mutated the residues important for binding *in silico* and selected the ones with highest positive energy difference ($\Delta\Delta G > 0$) for further experimental validation.
- Predicted the complex structures of H-Ras and K-Ras4B proteins with their downstream effectors.

Construction of GR/C-EBP/SWI-SNF chromatin remodeling complexes

- Predicted the binary interactions between GR, C-EBP and SWI/SNF chromatin remodeling complex subunits using PRISM and constructed a multimeric structure by superimposing the predicted binary complexes.

Construction of the structural network of Interleukin-10 (IL-10)

- Identified the binding partners of IL-10 and predicted the complex structures of these interactions using PRISM.
- Constructed the structural network of IL-10.
- Exploited mutations identified in cancer patients, mapped them onto key proteins of IL-10 network.
- Analyzed the effect of these mutations on the interactions, and demonstrated a relation between these and inflammation and cancer.

Koç University

Istanbul, Turkey

Research Assistant; Advisor: Halil Kavaklı

2015-Present

Experimental investigation of H- and K-Ras dimerization

- Applied the BiFC method to visualize the interactions of wild type and constitutively active (HRASG12V, KRAS4BG12D) H-Ras and K-Ras4B homodimers.
- Performed site-directed mutagenesis to mutate the predicted interface residues.
- Applied the BiFC method to observe the effects of mutations on binding.
- Analyzed the effect of mutations on downstream signaling pathways (MAPK and Akt pathways) using SDS-PAGE with western blotting (compared the levels of phosphorylated ERK and Akt proteins).

National Cancer Institute

Frederick, MD, USA

Guest Researcher; Advisor: Ruth Nussinov

Summer 2013, 2014, 2016

Computational studies on H- and K-Ras dimerization and Ras-effector interactions MD simulations of Ras/PDE δ complexes**TEACHING EXPERIENCE****Koç University**

Istanbul, Turkey

Teaching Assistant, Reaction Engineering

Spring 2014, 2015, 2016, 2017

Teaching Assistant, Bioinformatics

Fall 2013, 2014, 2016

Teaching Assistant, Biomolecular Structure, Function and Dynamics

Fall 2015

Teaching Assistant, Organic Chemistry II Lab

Spring 2013

Teaching Assistant, Organic Chemistry I Lab

Fall 2012

CONFERENCE PRESENTATIONS

Muratcioglu, S., Chavan, T.S., Freed, B.C., Jang, H., Khavrutskii, L., Freed, R.N., Dyba, M.A., Stefanisko, K., Tarasov, S.G., GURSOY, A., Keskin, O., Tarasova, N.I., Gaponenko, V., Nussinov, R. GTP-Dependent K-Ras Dimerization. Poster presentation delivered at the 9th International Symposium on Health Informatics and Bioinformatics HIBIT 2015, Muğla, October, 2015.

Muratcioglu, S., Chavan, T.S., Freed, B.C., Jang, H., Khavrutskii, L., Freed, R.N., Dyba, M.A., Stefanisko, K., Tarasov, S.G., GURSOY, A., Keskin, O., Tarasova, N.I., Gaponenko, V., Nussinov, R. GTP-Dependent K-Ras Dimerization. Poster presentation delivered at the ISMB/ECCB 2015, Dublin, July, 2015.

Muratcioglu S., Nussinov R., GURSOY A., Keskin O. Identification of effector binding sites on H-Ras explains signal propagation. Poster presentation delivered at the Modeling of Biomolecular Systems Interactions, Dynamics, and Allostery: Bridging Experiments and Computations, Istanbul, September, 2014.

Muratcioglu S., Nussinov R., Gursoy A., Keskin O. Identification of effector binding sites on H-Ras explains signal propagation. Poster presentation delivered at the Intelligent Systems for Molecular Biology (ISMB) conference, Boston, MA, July, 2014.

WORKSHOPS

Computational Biophysics Workshop. Workshop on Integrative Modeling and Simulations, University of California San Francisco, San Francisco, CA, December, 2016.

Muratcioglu S., Nussinov R., Gursoy A., Keskin O. Template-based structure modeling of ras interactions. Poster presentation delivered at the International Symposium - Integrating spectroscopic and theoretical methods to analyse molecular machines, Germany, December, 2014.

PUBLICATIONS

Muratcioglu, S., Jang, H., Gursoy, A., Keskin, O., Nussinov, R. PDE δ binding to farnesylated Ras family proteins provides a route to proper membrane localization. *J. Phys. Chem. B.*, **2017** (accepted). (Impact factor: 3.187)

Jang, H., **Muratcioglu, S.**, Gursoy, A., Keskin, O., Nussinov, R. Membrane-associated Ras dimers are isoform-specific: K-Ras dimers differ from H-Ras dimers. *Biochem J.*, **2016**, 473(12):1719-32. (Impact factor: 3.562)

Chavan, T.S., **Muratcioglu, S.**, Marszalek, R., Keskin, O., Gursoy, A., Nussinov, R., Gaponenko, V. Plasma membrane regulates Ras signaling networks. *Cell Logist.*, **2016**, 5(4):e1136374.

Nussinov, R., **Muratcioglu, S.**, Tasi, C.J., Jang, H., Gursoy, A., Keskin, O. K-Ras4B/calmodulin/PI3K α : A promising new adenocarcinoma-specific drug target? *Expert Opin Ther Targets.*, 2016, 20(7):831-42 (Impact factor: 4.798)

Lu, S., Jang, H., **Muratcioglu, S.**, Gursoy, A., Keskin, O., Nussinov, R., Zhang, J. Ras Conformational Ensembles, Allostery, and Signaling. *Chem Rev.*, 2016, 116(11):6607-65 (Impact factor: 37.369)

Muratcioglu, S., Guven-Maiorov, E., Keskin, O. Gursoy, A. Advances in template-based protein docking by utilizing interfaces towards completing structural interactome. *Curr Opin Struct Biol.*, 2015, 35:87-92 (Impact factor: 6.713)

Nussinov, R., Tsai, C.J., **Muratcioglu, S.**, Jang, H., Gursoy, A., Keskin, O. Principles of K-Ras effector organization and the role of oncogenic K-Ras in cancer initiation through G1 cell cycle deregulation. *Expert Rev Proteomics.*, 2015, 12(6):669-82 (Impact factor: 3.465)

Muratcioglu, S., Presman, D.M., Pooley, J.R., Grøntved, L., Hager, G.L., Nussinov, R., Keskin, O., Gursoy, A. Structural Modeling of GR Interactions with the SWI/SNF

Chromatin Remodeling Complex and C/EBP. *Biophys J.*, 2015, 109(6):1227-39 (Impact factor: 3.632)

Nussinov, R., **Muratcioglu, S.**, Tsai, C.J., Jang, H., Gursoy, A., Keskin, O. The Key Role of Calmodulin in KRAS-Driven Adenocarcinomas. *Mol Cancer Res.*, 2015, 13(9):1265-73 (Impact factor: 4.510)

Muratcioglu, S., Chavan, T.S., Freed, B.C., Jang, H., Khavrutskii, L., Freed, R.N., Dyba, M.A., Stefanisko, K., Tarasov, S.G., Gursoy, A., Keskin, O., Tarasova, N.I., Gaponenko, V., Nussinov, R. GTP-Dependent K-Ras Dimerization. *Structure.*, 2015, 23(7):1325-35 (Impact factor: 5.237)

Acuner-Ozbabacan, E.S., Engin, B.H., Guven-Maiorov, E., Kuzu, G., **Muratcioglu, S.**, Baspinar, A., Chen, Z., Van Waes, C., Gursoy, A., Keskin, O., Nussinov, R. The structural network of Interleukin-10 and its implications in inflammation and cancer. *BMC Genomics.*, 2014, 15 Suppl 4:S2 (Impact factor: 3.986)

REFERENCES

Özlem Keskin, Ph.D.
Professor
Department of Chemical and Biological Engineering
Koç University
Rumelifeneri Yolu Sarıyer, 34450, Istanbul, Turkey
Office: Eng 224
Ph: +90-212-338-1538
okeskin@ku.edu.tr

Ruth Nussinov, Ph.D.
Professor
Center for Cancer Research
National Cancer Institute
Building 542, Rm 603
Frederick, MD 21702-1201
Ph: 301-846-5579
nussinov@helix.nih.gov

Attila Gürsoy, Ph.D.
Professor, Assoc. Dean of Engineering
Department of Computer Engineering
Koç University
Rumelifeneri Yolu Sarıyer, 34450
Istanbul, Turkey
Office: Eng 224
Ph: +90 212 338 1720
agursoy@ku.edu.tr

İ.Halil Kavakli, Ph.D.
Professor
Departments of Chemical and
Biological Engineering and Molecular
Biology and Genetics
Koç University
Rumeli Feneri Yolu Sarıyer, 34450
Istanbul, Turkey
Ph: +90 (212) 338-1708
hkavakli@ku.edu.tr